University of Cincinnati

Date: 7/13/2015

I, Arvindh R Sharma , hereby submit this original work as part of the requirements for the degree of Master of Science in Aerospace Engineering.

It is entitled:

Liquid Jet in Oscillating Crossflow: Characterization of Near-Field and Far-Field Spray Behavior

Student's name: **Arvindh R Sharma**

This work and its defense approved by:

Committee chair: Jongguen Lee, Ph.D.

Committee member: Milind Jog, Ph.D.

Committee member: Mark Turner, Sc.D.

17361

Liquid Jet in Oscillating Crossflow: Characterization of Near-Field and Far-Field Spray Behavior

A thesis submitted to

The Graduate School of the University of Cincinnati

in partial fulfillment of the requirements for the degree of

Master of Science

in the Department of Aerospace Engineering and Engineering Mechanics of

the College of Engineering and Applied Science

July 2015

by

Arvindh R. Sharma

B.E. Aeronautical Engineering, Anna University, 2012

Committee Chair: Dr. Jongguen Lee

Abstract

An experimental investigation of response characteristics of a liquid jet in oscillating crossflow is undertaken to understand the behavior of a liquid fuel spray in the presence of combustion instabilities. The effect of crossflow oscillations on the liquid jet is studied in the near-field (within $x/d \approx 8$) and the far-field ($x/d \approx 50$) spray region. Experiments are conducted in bag breakup, multimode and shear breakup regimes by varying crossflow Weber number from 18 to 250, while momentum flux ratio is varied between 10 and 30. The crossflow is modulated in the frequency range of 90 Hz to 450 Hz, with modulation level varying between 5% and 20%, using a mechanical modulating device. High speed shadowgraph is employed to study the near-field and far-field spray movement while intensified high-speed camera images of laser Mie-scattering intensity are utilized in studying the spray cross-section in the far-field. A technique to extract time-varying momentum flux ratio from the windward trajectory of liquid jet in the near-field is developed. The response of near-field spray is quantified in terms of a ratio of the observed momentum flux ratio extracted from a correlation of upper penetration to the expected momentum flux ratio corresponding to the instantaneous crossflow velocity. The liquid jet penetration is found to respond to oscillations in the crossflow at all oscillation frequencies in the near-field. The strength of the response is found to be mainly dependent on the crossflow oscillation frequency, with the strength of response decreasing with increase in frequency. The momentum flux ratio and the modulation level are found to have relatively negligible effects on the level of normalized spray response. The spray response in the far-field is studied by observing the high-speed shadowgraphs and Mie-scattering intensity images at an axial distance of $x/d=50$. The spray field in the axial location is divided into ten bins and the intensity change in each bin is analyzed to quantify spray response. The spray is found to respond to crossflow

oscillations by exhibiting a “flapping” behavior in the far-field. The binning method and Mie-scattering intensity image analysis suggest that the spray oscillation decreases with increasing crossflow frequency. The spray width and height fluctuate in the spray cross-section in the presence of crossflow oscillation. The amplitude of spray height fluctuation is higher in low frequency crossflow, and decreases with an increase in frequency. The total Mie-scattering intensity in the cross-section also exhibits a periodic response to crossflow oscillation, suggesting that the droplet characteristics are affected by crossflow fluctuation. The liquid spray near-field and far-field study indicates that the crossflow oscillation frequency plays a large role in determining spray response.

Acknowledgements

I owe a debt of gratitude to a multitude of people for making my graduate study at the University of Cincinnati a true learning experience. I would like to thank Dr. Jongguen Lee, my advisor, for inspiring me to realize the object and method of research. I am greatly indebted to Dr. Jinkwan Song for being an insightful mentor and a guide in my research. I also thank all the students and staff at Center Hill Research Facility for helping me in every turn. I thank Curtis Fox and Doug from the Machine Shop for helping me set up my test rig. I am grateful to Dr. Milind Jog and Dr. Mark Turner for graciously accepting to serve on my thesis committee. I express my heartfelt thanks to my friends at Cincinnati for enriching my graduate life experience.

I cannot express my thanks to my family and friends at home, as that would be a disservice, for this is as much their journey as it is mine.

Contents

Nomenclature

A	Nozzle orifice exit area
AMD, D_{10}	Arithmetic Mean Diameter
C_d	Coefficient of discharge
d	Nozzle orifice diameter (also referred to as "jet diameter")
f	Frequency of crossflow modulation
FFT	Fast Fourier Transform
H	Spray height or vertical extent
MFR, $\dot{m}$	Mass flow rate
MDL	Modulation Level, (Ratio of RMS of crossflow velocity fluctuation to mean crossflow velocity)
NAR	Normalized Amplitude Ratio
P	Crossflow static pressure
q	Momentum flux ratio, ($q=\rho_j v_j^2/\rho_a v_a^2$)
RMS	Root Mean Square
SMD, D_{32}	Sauter Mean Diameter
T	Temperature

v_a	Crossflow velocity
v_j	Liquid jet velocity
W	Spray width or lateral extent
We	Weber number, ($We=\rho_a v_a^2 d/\sigma$)
x	Distance along crossflow direction from the nozzle orifice
y	Distance along the transverse direction (direction of liquid jet injection) from the nozzle orifice
z	Distance along the direction orthogonal to crossflow and liquid injection, measured from the left edge of test-section when looking upstream in the crossflow direction
ρ	Density of the medium
μ	Viscosity of the medium
ϕ	Equivalence ratio
σ	Surface tension

Subscripts

a	Air crossflow property
Br	Breakup point

CI	Center of Intensities
j	Liquid jet property
l	Liquid property
Inj	Injection property

List of Figures

List of Videos

List of Tables

1 Introduction

Jet in crossflow (JIC) is a paradigm in fluid mechanics which is ubiquitous in the natural world and in the field of engineering. A jet in crossflow can be described as a stream of matter interacting with another crossflowing stream at a right angle. The phenomenon can be readily observed in volcanic plumes interacting with the wind, water sprinklers, agricultural sprays, fuel injection systems, smoke stacks, aerosol sprays, and so on. It is a concept easier in its physical conceptualization but more complex in its formulation due to the interplay between various facets of classical mechanics.

In the field of aerospace engineering, liquid jet in crossflow (LJIC) is well suited for fuel-injection applications. From gas turbine combustors, afterburners, ramjets, scramjets to rocket engines, liquid fuel placement is a critical component in the design of engines. The liquid fuel has to be fed reliably to the combustor, atomized into small droplets, distributed spatially and burn within a specific time in order for the engine to perform optimally. With its relative simplicity in design and efficiency in fuel placement, LJIC is widely used in aerospace fuel injection systems.

Modern standards in emission control and considerations of fuel combustion efficiency have driven gas turbine technology towards lean-premixed-prevaporized (LPP) combustion. The combustion process, in general, encounters fluctuations in heat release due to perturbations in the fuel flow, air mass flow, or their mixing characteristics. Particularly in lean operation, the heat release process is very sensitive to perturbations [1].

Consider the case where a perturbation in heat release rate due to combustion instability produces an acoustic disturbance, illustrated in Figure 1. The acoustic pressure fluctuations travel upstream and downstream from the combustor, and interact with the incoming air and fuel in the combustor. The interaction causes perturbations in the air and fuel flow. Since the equivalence ratio depends upon the mixing of the air and the fuel, fluctuations arising from either the air or the fuel flow cause perturbations in the equivalence ratio as well. These fluctuations then feed back into the fluctuations in the heat release. The damping or the amplification of the combustion instability is thus dependent on the interaction and phase difference between the pressure and heat release fluctuations. The Rayleigh criterion, which is widely used in acoustics-heat interactions, specifies that for an acoustic oscillation to persist, the phase of the oscillation should closely match the phase of the heat release oscillation [2].

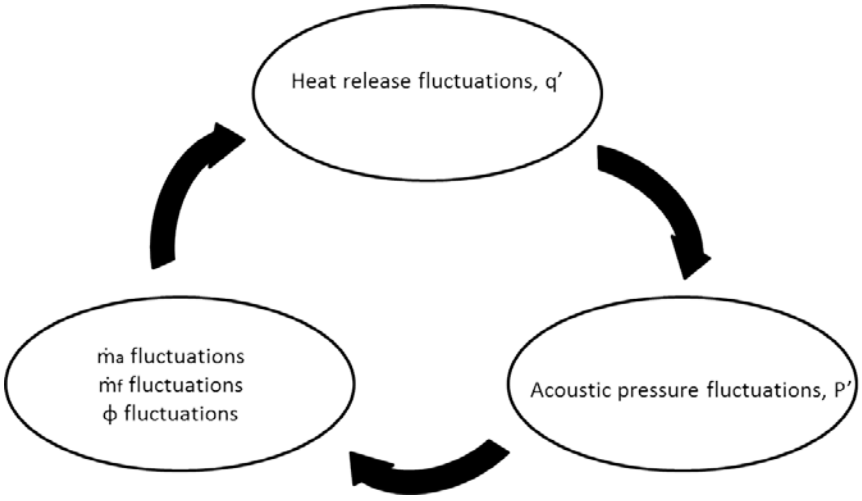

Figure 1. Combustion instability model

The phase difference between the heat release and acoustic pressure fluctuations would then depend upon the time scale of liquid atomization and combustion. The knowledge of response characteristics of the liquid fuel jet to the fluctuations in the crossflow pressure and velocity is

therefore of paramount importance in the study of combustion instabilities. Since the combustion instabilities can lead to mechanical degradation of the combustor and adversely affect combustion performance, the relationship between acoustic oscillations and liquid jet spray formation is of critical interest.

1.1 Literature Review

The study of response of a liquid jet to oscillating crossflow requires an understanding of the various physical phenomena that govern liquid jet breakup in general. The physics behind liquid jet breakup has been the focus of numerous studies for many decades and the aspects relevant to the current study are summarized in this section.

1.1.1 Liquid Jet Structure

The liquid jet and the associated flow structures that develop after the impingement of a crossflow have been extensively studied by various researchers [3-7]. Upon injection from the nozzle exit, the liquid jet in a crossflow develops surface wave patterns due to aerodynamic acceleration along the liquid column. The liquid column is bent in the crossflow direction and gets flattened to a "kidney-shaped jet". This flattening is the result of the establishment of a high pressure windward region and a low pressure leeward region, with the difference proportional to the crossflow dynamic pressure. The flattening further increases aerodynamic drag on the column and the column is bent further. Coherent masses of liquid, called "ligaments", break away from the jet column and are generated from the troughs of some of the surface waves. The amplitude of the surface waves grows until fracture of the liquid column.

The ligaments get broken down further into smaller droplets due to the action of shear forces from the crossflow. Droplets are also stripped off the sides of the jet column when the column

itself is intact. This occurs when the air flow strips off droplets from the crests of waves at the periphery of the jet. Thus, the breakup produces three stages/phases of liquid: 1. column, 2. ligament, and 3. droplets. These structures are characteristic of column breakup, as illustrated in Figure 2.

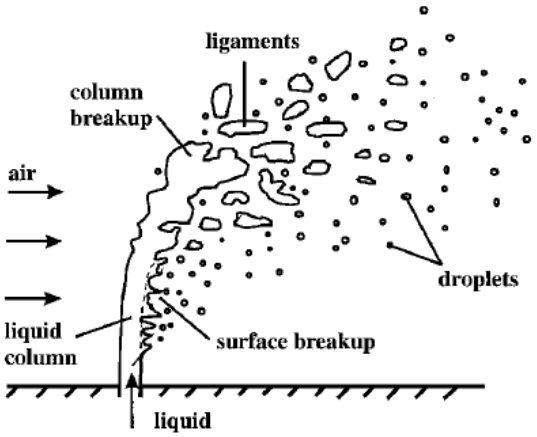

Figure 2. Typical liquid jet breakup process [3]

The crossflow induces the formation of a leading vortex near the jet injection point and a trailing vortex in the jet wake. The liquid jet and vortex interactions cause the jet to flutter, which causes the vortices to change in position, strength and orientation.

The non-dimensional parameters Weber number, *We,* and the momentum flux ratio, q, are key concepts in studying jet breakup and are given in Eqs. (1) and (2). The gas Weber number, which is the ratio of the gaseous crossflow's inertial force to the surface tension force of the liquid, is a measure of the interaction between the aerodynamic force exerted by the crossflow and the cohesive surface tension force on the liquid jet surface. The momentum flux ratio is a measure of the liquid jet's momentum flux compared to that of the crossflow and thus an important factor in determining the jet penetration.

$$We = \frac{\rho_a v_a^2 d}{\sigma_l} \quad (1)$$

$$q = \frac{\rho_j v_j^2}{\rho_a v_a^2} \quad (2)$$

1.1.2 Breakup Mechanisms and Regime Map

Two major breakup mechanisms are observed in liquid jet breakup: 1. Column breakup, and 2. Shear breakup. In column breakup, surface waves on the windward side grow in amplitude until the column fractures in one of the wave troughs. The surface breakup mechanism, on the other hand, involves the shearing off of ligaments and droplets from the sides of the jet. While both mechanisms are active, either one dominates at any point in time. Since the surface breakup generates droplets from shear forces, the droplets are of smaller sizes and result in better atomization of the jet [3,4,8,9].

Sallam et al. [6] describe four breakup mechanisms based on the crossflow Weber number - column, bag, multimode (bag/shear) and shear breakup regimes - in non-turbulent jets.

Table 1. Breakup modes [6]

Column breakup	Bag breakup	Multimode breakup	Shear breakup
We < 4	We = 4 – 30	We = 30 – 110	We > 110

In bag breakup (We = 4 – 30), the jet breaks up into bag-like structures which grow in size and are further deformed downstream in the crossflow. Between We = 30 – 110, both bags and ligaments are capable of forming, and this mode is called multimode breakup (Figure 3).

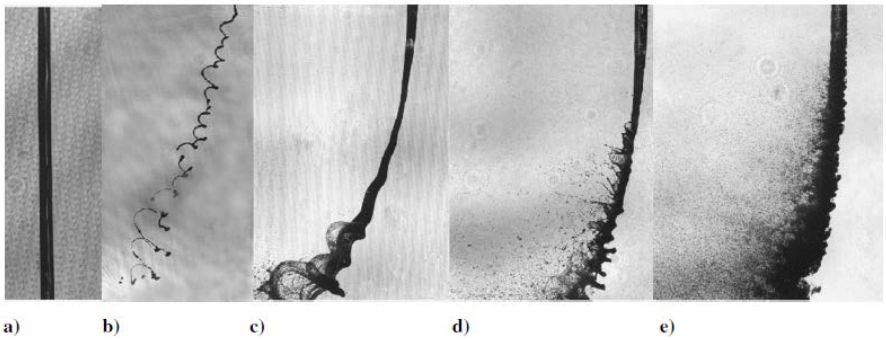

Figure 3. Breakup modes : a)Jet in still crossflow, b)Column Breakup, c)Bag breakup, d)Multimode breakup, and e)Shear breakup [6]

Breakup regime maps have been proposed by a number of researchers to identify the flow conditions that govern the different breakup mechanisms [3,4,10]. The summary of their findings is that the shear and column breakup regimes depend upon the Weber number and momentum flux ratio, with flows associated with higher values of both these parameters tending to have shear breakup. The transition between predominantly column breakup to predominantly shear breakup has been observed and demarcated in the literature, with one such breakup regime map shown in Figure 4.

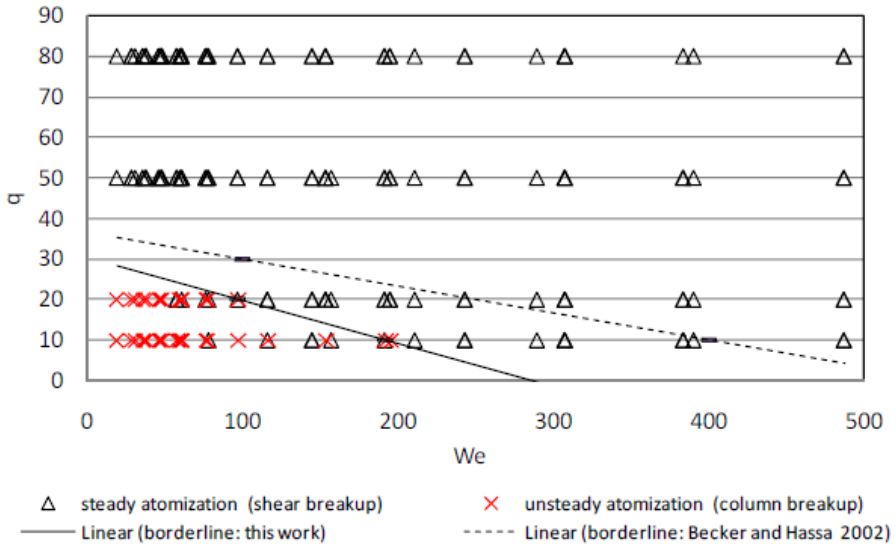

Figure 4. Breakup Regime Map from Amighi et al. [10]

1.1.3 Column Breakup Location

The column breakup point (CBP) is an important flow feature in the near-field determining the location up to which the injected liquid column preserves its coherent structure. The location of the column fracture point in the crossflow direction for atmospheric pressure crossflows has been found to be independent of momentum flux ratio and postulated to be around $x/d \approx 8$ [3-6]. Ragucci et al. [11] observed that the breakup location is dependent on air dynamic-to-capillary pressure ratio (and thus on Weber number) but only weakly dependent on momentum flux ratio. Lubarsky et al. [12] noted that the constant stream wise breakup location of $x/d \approx 8$ is an over prediction of the actual breakup point. As the momentum flux ratio is increased, two opposing effects are found to govern the CBP: 1. liquid velocity increases with momentum flux ratio, possibly increasing breakup point distance, and 2. the increased liquid velocity enhances the turbulence level, which enhances the size of the liquid surface structures, hastening jet breakup. On increasing the Weber number, similar effects were observed if the momentum flux ratio was kept a constant.

1.1.4 Droplet Characteristics

The droplet sizes and speeds determine the spatial and temporal distribution of the liquid in the crossflow.

At higher crossflow velocities, with the generation of small droplets in the spray periphery, the larger droplets cluster near the spray core whereas at lower crossflow velocities, the droplets generated tend to be larger, penetrate more in to the crossflow and cause the drop sizes to peak near the spray upper periphery [4,13]. The droplet velocities are dependent on the droplet sizes. Smaller droplets usually attain higher velocities on interaction with the crossflow while the larger ones have comparatively lower velocities [8].

1.1.5 Liquid Jet Penetration

The liquid jet penetration can be defined as the "maximum transverse distance attained by the droplets" [14], noting that other analogous definitions are used by different researchers. The spray penetration is an important parameter that dictates liquid placement in the crossflow.

The penetration of the liquid is the result of two successive processes: 1. the liquid coherent jet penetration, and 2. the penetration by the atomized spray. The momentum flux ratio determines the transverse distance up to which the liquid retains its momentum before getting entrained in the crossflow due to momentum exchange. Especially in the near-field, therefore, the liquid jet penetration is mainly a function of the momentum flux ratio, while only weakly dependent on the crossflow Weber number [3,12,13]. Amighi et al. [10] experimentally determined the penetration trajectory to depend more on the liquid jet velocity than the crossflow air speed. A few other studies note that the spray penetration is dependent upon the size of the droplets generated [4,14]. While the liquid column penetration has been found to be a function of momentum flux

ratio, the spray penetration has been found to be influenced by both the liquid column trajectory and the convection of droplets.

Numerous correlations exist in the literature for predicting the upper surface penetration [3,4,7,10,12-15]. From a sampling of the various correlations and mechanisms describing liquid jet penetration, it becomes clear that no single correlation can accurately predict the penetration. This is due to the fact that different experimental conditions and different post-processing techniques (for example, threshold value, location of maximum intensity) lend themselves to varying results. However, there is a degree of commonality between the correlations, as discussed below.

Wu et al. [3] use a force balance between the liquid jet's acceleration in the crossflow direction and the aerodynamic drag force to predict a simple correlation. Since they consider a liquid column with a constant diameter equal to the nozzle orifice and neglect the effects of mass stripping, the correlation they propose can be expected to be more suitable for near-field penetration. They propose the correlation given in Eq. (3):

$$\left(\frac{y}{d}\right) = 1.37\sqrt{q\left(\frac{x}{d}\right)} \qquad (3)$$

Unsurprisingly, many of the correlations from literature provide correlations for y/d as parabolic functions (or close to parabolic functions, with powers between 0.3 and 0.6) of q and downstream distance, *x/d*, with the inclusion of correction terms for various parameters like liquid viscosity and crossflow air density. For example, Stenzler et al. [14] provide a correlation with corrections for the crossflow Weber number and liquid viscosity for unheated crossflow conditions, given in Eq. (4).

$$\left(\frac{y}{d}\right) = 3.688q^{0.430}\left(\frac{x}{d}\right)^{0.384} We^{-0.110}\left(\frac{\mu_l}{\mu_{H_2O}}\right)^{-0.108} \quad (4)$$

1.1.6 Effect of crossflow modulation

Bunce et al. [16] studied the effects of crossflow modulation on a vaporizing liquid spray at an air temperature of 650 °C using Jet-A as the liquid. They studied the spray response at a modulation frequency of around 416 Hz. On comparing averaged Mie-scattering images, they found that the crossflow modulation did not cause a large change in upper penetration of the spray compared to non-modulated conditions. However, instantaneous images showed a distinctive change in the spray visible area at different phases of oscillation. They observed from Laser Line Mie scattering signals that the spray responded at twice the modulation frequency and found that the amplitude of response varies depending on distance from the injector. The imperceptible change in penetration with input air modulation was attributed to the location of the injector near a pressure anti-node, causing the velocity fluctuations to be minimal. The study's results, therefore, could have been influenced by the presence of velocity node.

McQuay and Dubey [17] experimentally investigated droplet behavior in the case of an evaporating ethanol spray in an oscillating air crossflow at three modes, 54, 106 and 162 Hz, all maintained at a constant sound pressure level in a long tube. They observed that the droplet velocities responded to the forcing frequency by analyzing frequency spectra. They were mainly focusing on the droplet behavior in oscillating flows.

Anderson et al. [18] studied the coherence (measure of linearity of response) between modulated crossflow and fuel mass flow at various axial locations. They found variations in the coherence values over a range of frequencies and different injector designs. The coherence was expected to

change with axial distance since the droplets are atomized to different levels at different axial locations. Since smaller droplets could follow the crossflow more readily and thus respond easily to fluctuations, the atomization process was expected to affect the spray response to modulation. The study throws light on the effect of frequency on the response, but is focused on seeing the response of planar mass flow to modulation of crossflow.

Song et al. [19] studied the response of liquid spray penetration and the atomization process to air modulation. In a crossflow with We=326.19 (shear breakup regime), modulation frequency of 150 Hz and a crossflow velocity fluctuation amplitude of 18% of mean velocity, they observed from Mie-scattering images that the maximum intensity trajectory of the spray did not deviate substantially from the non-oscillating crossflow cases. However, they found that the trajectory was slightly lower than the steady crossflow case, attributing the reduction in penetration to the generation of a higher number of smaller droplets in the presence of oscillating crossflow, independently confirmed by Phase Doppler Particle Analyzer data. It was also observed that the different local regions within the spray responded differently to modulation, by studying Mie-scattered intensity. The upper and central portions of the spray were observed to respond to the fundamental frequency and higher harmonics of modulation while the lower portion responded primarily to only the fundamental frequency. The upper and lower regions of the spray intensities were also found to be out-of-phase with each other and this was attributed to different droplet velocities in the two regions.

In another study focusing on spray response to crossflow modulation at 800 Hz, Song et al. [20] confirmed the previous observation that the spray penetration does not fluctuate substantially. An interesting finding was that the spray responded to modulation in the form of convective oscillations along the crossflow direction. PDPA measurements indicated that the number of

both larger and smaller droplets increase in number in the presence of oscillating crossflows, and the effect of droplet sizes and velocities were noted to be important in quantifying spray response. Thus research work in [19] and [20] showed that the penetration is not affected much by modulation but the experiments were primarily conducted in the shear flow regime.

Anderson et al. [21], on the other hand, observed that the spray penetration showed significant response to crossflow modulation at 200 Hz. However, their experiments were conducted at modulation levels close to 50% and were limited to crossflow frequency of 200 Hz. They also observed that there was finite phase lag between the spray density and the crossflow at an arbitrary measurement plane downstream of injector. The phase lag was found to be uniform in the direction of the jet injection but varied significantly at the top of the spray, indicating that different sized droplets respond differently to the crossflow modulation.

While the available literature offers good starting points and offer physical explanations piecemeal, a comprehensive picture of the response of liquid spray penetration and distribution to crossflow modulation does not emerge.

1.2 Motivation and Objectives

Liquid jet in crossflow is extensively used to inject fuel in gas-turbine and other aero-engine combustors. The liquid fuel jet, upon injection, penetrates into the crossflow and begins to break down into droplets. While the penetration is a major factor governing the spatial distribution of the liquid spray in the combustor, the breakup mechanism, which influences the droplet sizes and velocities, is an equally important factor affecting the spatio-temporal distribution.

When encountering combustion instabilities, which results in crossflow oscillation, the response of the fuel jet becomes crucial. The near-field of fuel injection determines to a large extent the

spray penetration in the far-field. The response of fuel penetration in the near-field could also lead to changes in the droplet sizes, and thus velocities, causing variations in the fuel distribution downstream.

The character of response in the far-field region is also critical in the combustion process. For instance, the far-field fuel spray could respond to crossflow oscillation by fluctuating up and down in the direction of fuel injection. There might also be oscillations in the mass flow due to the crossflow oscillation producing different sized droplets in the near-field. Moreover, the spray cross-section could also be influenced by the combustion instability induced pressure oscillations. These factors ultimately decide the spatial and temporal fluctuations in heat release. Therefore, the study of the response of a fuel jet to crossflow fluctuations is a precursor to the study of combustion dynamics in the presence of instabilities.

The knowledge of fuel jet response characteristics could provide useful information for the design of combustors and fuel injection systems to either avoid or control combustion instabilities. From the review of literature, it is apparent that the research in this topic has been scarce and has tended to focus on few flow conditions, frequencies or specific aspects such as droplet convection and spray penetration. Especially in the near-field where the momentum flux ratio plays a large role in determining jet penetration, there is a need for quantitative evaluation of jet response to crossflow oscillations. Since the jet in crossflow involves complex interactions between fluid properties such as air density, liquid surface tension, viscosity, the velocities of both phases, and so on, any comprehensive study of liquid jet in oscillating crossflow should encompass the different breakup regimes and flow conditions.

Combustion instabilities evidently are influenced by the spatial and temporal distribution of the fuel and the frequency of acoustic oscillations in the crossflow [1]. A study of liquid jet response to oscillating crossflow in different breakup regimes, a range of oscillation frequencies at which combustion instabilities occur and different oscillation strengths will therefore throw light on the thermo-acoustic interactions in combustors.

The objectives of the current study, therefore, stem from the need to identify and quantify the response of liquid jet to oscillating crossflow. The initial step would be to observe a liquid jet in a modulated crossflow to detect the manner in which near-field penetration responds. Then, a method to quantify the response in the near-field would have to be devised. Since the far-field spray penetration is influenced by the near-field penetration, the near-field study leads to far-field spray fluctuation studies. The far-field spray region is to be investigated to ascertain the effect of crossflow oscillations on the spray spread, location and composition.

2 Experimental Setup, Procedures and Calibrations

2.1 Experimental Setup

The experimental setup consists of a horizontal test rig which includes the following major subcomponents: compressed air supply, an air modulating device (nicknamed “siren”), test-section with a liquid injection port, a back-pressure regulator and a liquid injection system.

The siren is a device that consists of an enclosed rotor and stator assembly through which air is passed to obtain a flow with oscillations. The cross-sectional view of the siren is shown in Figure 5. The rotor has four equally spaced holes that can each align with the single hole in the stator during one rotation of the rotor. Inlet air enters through a port and when one of the holes in the rotor aligns with the stator, the air passes through the siren to the outlet port. In this way, a periodicity is induced in the air mass-flow through the siren. The siren rotor shaft is driven by a DC motor with speed control.

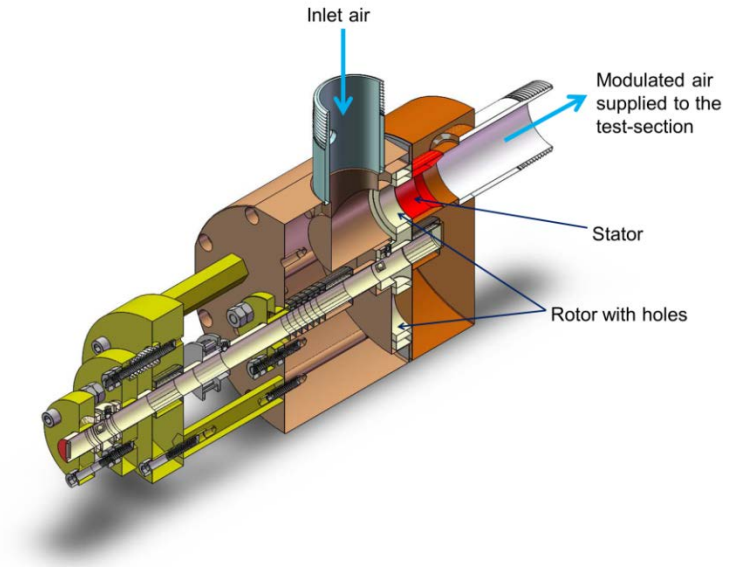

Figure 5. Siren: Cross-section view

The air from the compressor is metered through a Micro Motion mass flow sensor (F200 series) and then supplied to the siren and a bypass line. To obtain crossflows with variable modulation levels, the modulated air is mixed with the bypass air, and the mass flow rates of modulated air and the bypassed air are adjusted to produce crossflows with desired modulation levels.

A schematic of the test rig showing the test-section is given in Figure 6. The test-section made of stainless steel has a rectangular cross-section with a height of 31.8 mm and a width of 25.4 mm. In order to provide optical access, windows made of fused silica are used on the sides and top sections. The windows allow for optical access up to a downstream distance of 200 jet diameters (200 d) from the injector. The static pressure is measured at a point 47.6 mm upstream of the liquid injection plane using a digital pressure gauge (SSI Technologies Inc.). The experiments are conducted at room temperature (293 K). The dynamic pressure is measured using piezo-electric pressure transducers (PCB Piezotronics Model 112A22) at the ports indicated in the schematic as A, B, C, and D. The static pressure in the test-section can be adjusted by controlling the back-pressure regulator downstream of the test-section. The dynamic pressure signals are acquired using an NI-DAQ system as explained in Section 2.2.1.

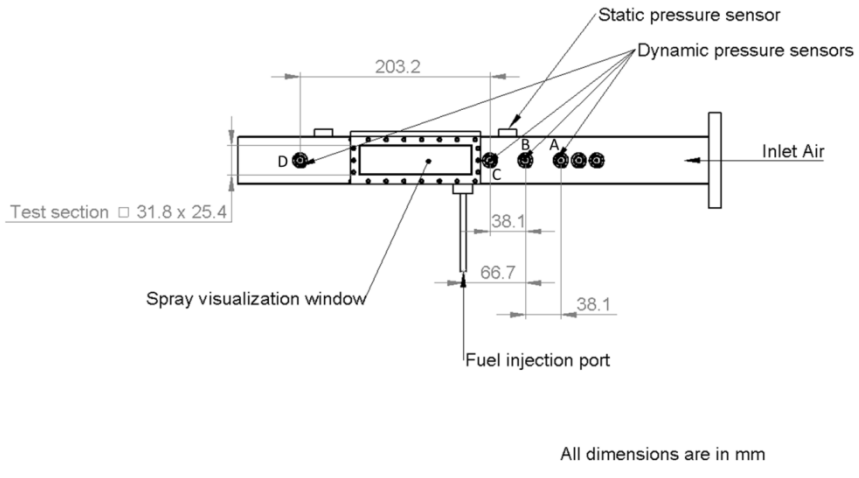

Figure 6. Schematic of test rig containing test-section

The liquid injection system consists of a stainless steel storage tank, a mass-flow meter (Brooks MT 3809) for measuring the liquid mass flow rate, and an injection nozzle. The storage tank can be pressurized with air to drive the liquid with injection pressure. A simple orifice injector with an orifice diameter of 0.5 mm (0.02 inch) and a length to diameter ratio of 5.5 is used for liquid injection. The injector uses a chamfer with angle 45° for transitioning from the larger tube diameter to the nozzle orifice diameter, as shown in Figure 7. The nozzle is flush mounted with the test-section lower surface for liquid injection. Water is the test liquid used throughout this study.

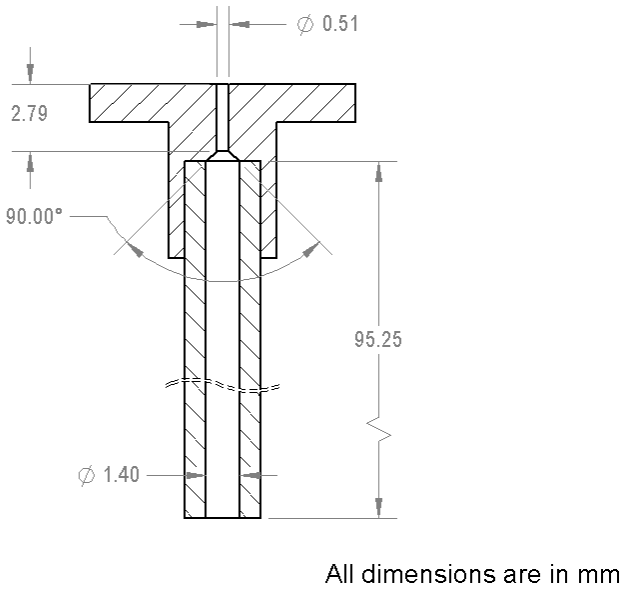

Figure 7. Cross-sectional view of injector [19]

2.2 Data Acquisition Systems

The experiments required the acquisition of pressure and image signals as detailed in the succeeding sections.

2.2.1 Two-Microphone Method to measure Crossflow Velocity Fluctuation

To measure instantaneous velocity in the crossflow, the dynamic pressure signal data is analyzed using the two-microphone method. The two microphone method has been used for many years in finding the instantaneous velocity using two pressure signals acquired within a small distance of each other [22,23]. The siren introduces oscillations in the crossflow air's mass flow and thus small pressure fluctuations are created. The two microphones measure the pressure fluctuations and convert them into velocity information. The two microphone method can be understood by considering Euler's momentum equation in Eq. (5) with acoustic pressure P and velocity V:

$$-\nabla P = \rho\left(\frac{\partial V}{\partial t} + \left(V.\nabla V\right)\right) \qquad (5)$$

Along one dimension (say x), with the assumption of small perturbations ($P=\bar{P}+P'$ and $V=\bar{V}+u'$) and zero mean velocity, the equation can be simplified to Eq. (6):

$$-\frac{\partial P'}{\partial x} = \rho\left(\frac{\partial u'}{\partial t}\right) \qquad (6)$$

Discretizing Eq. (6) for very small time and spatial steps, the equation transforms to Eq. (7):

$$-\left(\frac{P_2' - P_1'}{\Delta x}\right) = \rho\left(\frac{u'\left(t+\Delta t\right) - u'\left(t\right)}{\Delta t}\right) \qquad (7)$$

where the pressure perturbations refer to the pressure at points 1 and 2 separated by a small distance of Δx, and the velocity perturbations are the changes in velocity in a small time step of Δt. Rearranging the terms, an expression for velocity fluctuation, u', after the time step is obtained in Eq. (8):

$$u'(t+\Delta t) = -\frac{1}{\rho}\left(\frac{P_2' - P_1'}{\Delta x}\right)\Delta t + u'(t) \qquad (8)$$

Thus by acquiring pressure signals at two locations at a small spatial distance of Δx and by time stepping with a guess for the initial velocity perturbation *u'(0)*, the instantaneous velocity perturbation at the mid-point between the two pressure ports can be calculated by this method. One of the main sources of error, as detailed in the literature, is the finite difference approximation used to calculate the spatial derivative of pressure perturbation. Therefore, it is desirable to have a microphone separation distance orders of magnitude lower than the wavelength of the velocity oscillation.

Each acquisition of the pressure signals recorded 16384 samples acquired at a sampling rate of 8000 Hz.

2.2.2 High-speed Camera Imaging for Near-Field and Far-Field Visualization

Phantom Vision Research MIRO LC310 camera is used to acquire images for visualization of the flow in both near-field and far-field region. The images are acquired at a rate of 10000 Hz for a total of 1722 images per acquisition. The exposure time is set at 1 μs in order to observe the transitory liquid structures. A solid state light source (Thorlabs High Power Light Source) is used for illuminating the spray with visible light from one side of the test-section. The shadow formed by the spray in the test-section is captured by the camera on the other-side of the test-section as shown in Figure 8. An Infinity Long-Distance Microscope (Model K2-SC) is used to focus the near-field of the liquid jet while a Micro-Nikkor 105 mm lens is used to focus the far-field of the spray.

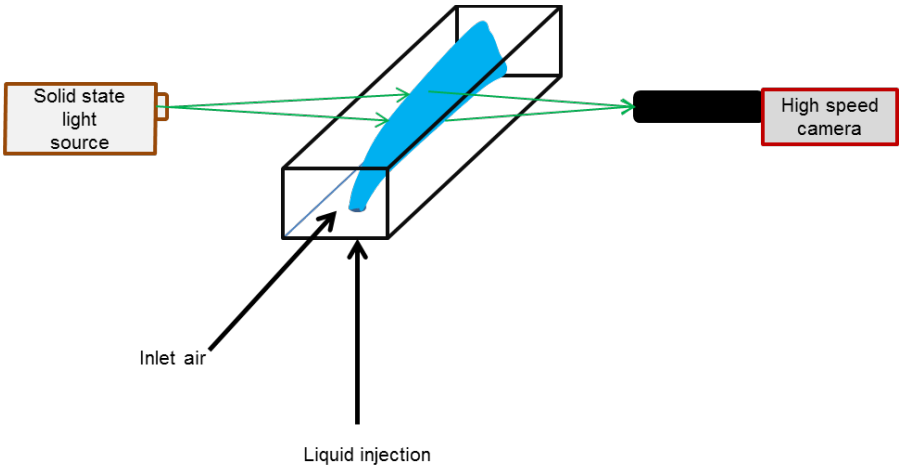

Figure 8. Image acquisition using high-speed camera

2.2.3 Intensified Camera Imaging for Spray Cross-Section Visualization using Laser Mie-Scattering

The spray cross-section is imaged by inducing laser Mie-scattering and capturing the scattered light using a Phantom v411 high speed camera with a Lambert Instruments' High-speed Intensified Camera Attachment (HiCATT). The schematic of the imaging setup is shown in Figure 9. A Helium-Neon laser of wavelength 632.8 nm is used for optical illumination. The beam from the He-Ne laser is transformed into a thin laser sheet using cylindrical lenses and provided into the test-section through one of the side windows. The intensifier-camera assembly is positioned at an angle of 45 degrees to the plane of laser illumination. The Mie-scattering signal pertaining to the image cross-section is then filtered using a bandpass filter with a center wavelength of 632.8 nm to filter out the optical noise. The intensifier is digitally gated with an open time of 1 μs and its trigger is synchronized with the high-speed camera's image acquisition (sampling rate 10000 Hz).

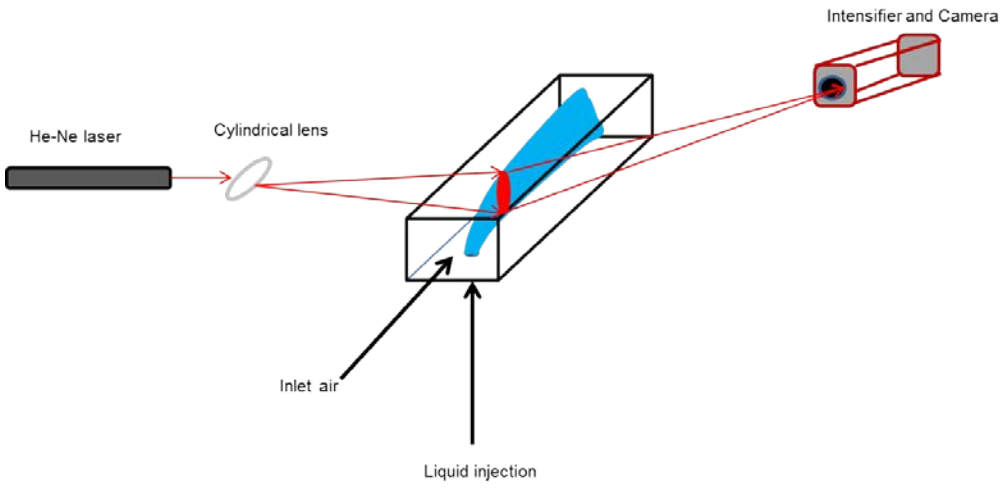

Figure 9. Image acquisition using intensifier-camera assembly

2.3 Calibrations

2.3.1 Nozzle flow calibrations

The orifice diameter of the liquid injection nozzle is checked to see if the diameter is within tolerance. The first method employed to check the diameter is to use plug gauges. Since the gauges used are in inches, this section utilizes the same unit and gives the equivalent length in millimeters within brackets. The nozzle orifice could accommodate the pin gauge of size 0.02 inch (0.508 mm) but would not allow the pin of size 0.021 inch (0.533 mm), indicating that the orifice diameter is indeed 0.02 inch (0.508 mm) within the pin guage tolerance (+0.0000/-0.0002 inch). The next method to verify the orifice diameter is to obtain a magnified image of the injector orifice plane, measure the outer diameter of the injector, then compare the pixel distances in the image to obtain the orifice diameter. This method is shown in Figure 10 and the diameter obtained using this method, 0.0195 inch (0.495 mm) suggests that the orifice diameter is closer to the negative limit of 0.02 inch (0.508 mm).

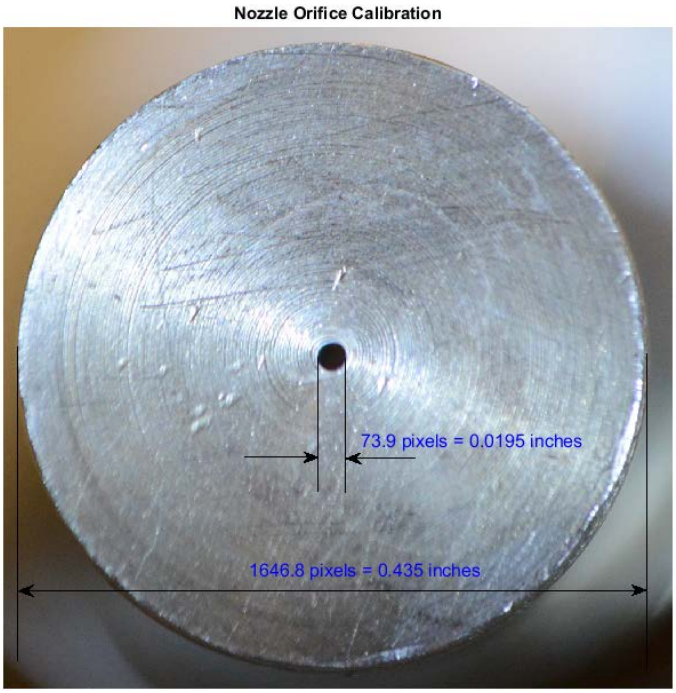

Figure 10. Nozzle orifice diameter calibration

The nozzle discharge coefficient (C_d) is the ratio of actual mass flow rate ($\dot{m}_l$) to the theoretical mass flow rate. It is calculated for different injection pressures by measuring the mass flow rate of the nozzle discharge using a weighing scale and a stop watch. The mass flow rate is calculated by measuring the mass of the liquid acquired over a given time. The weighing scale is calibrated with a known calibration mass. C_d is then calculated using Eq. (9):

$$C_d = \frac{\dot{m}_l}{A\sqrt{2\rho_l \Delta P_{Inj}}} \qquad (9)$$

It is observed from Figure 11 that the coefficient of discharge is close to 0.9 for a range of injection pressures up to around 4.08 atm (60 psi). After that point, the discharge coefficient starts to drop to values around 0.75. The instantaneous nozzle discharge images (1µs exposure) pertaining to three different injection pressures are shown in Figure 12. In order to avoid the

sudden drop in discharge coefficient which could be attributed to cavitation effects, the injection pressure range is maintained within 4.08 atm (60 psi) in the subsequent experiments.

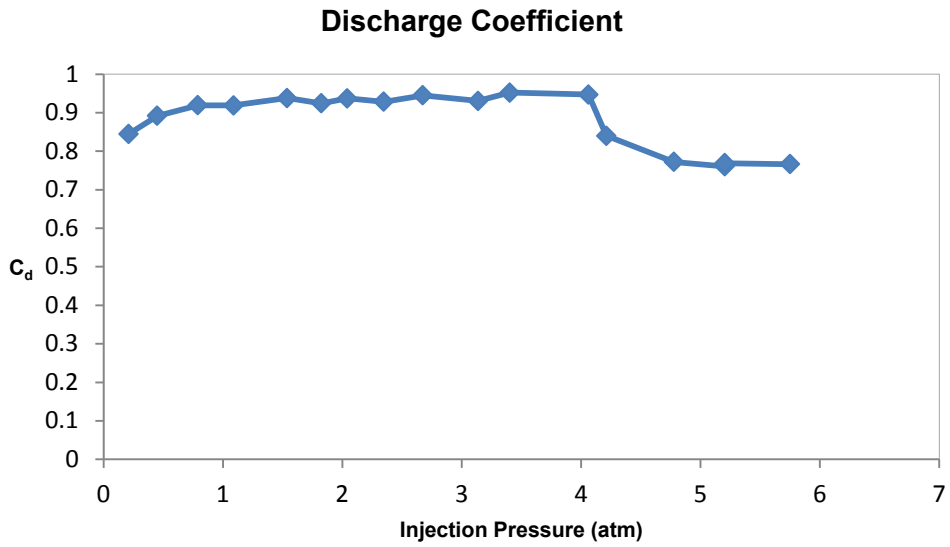

Figure 11. Nozzle discharge coefficient

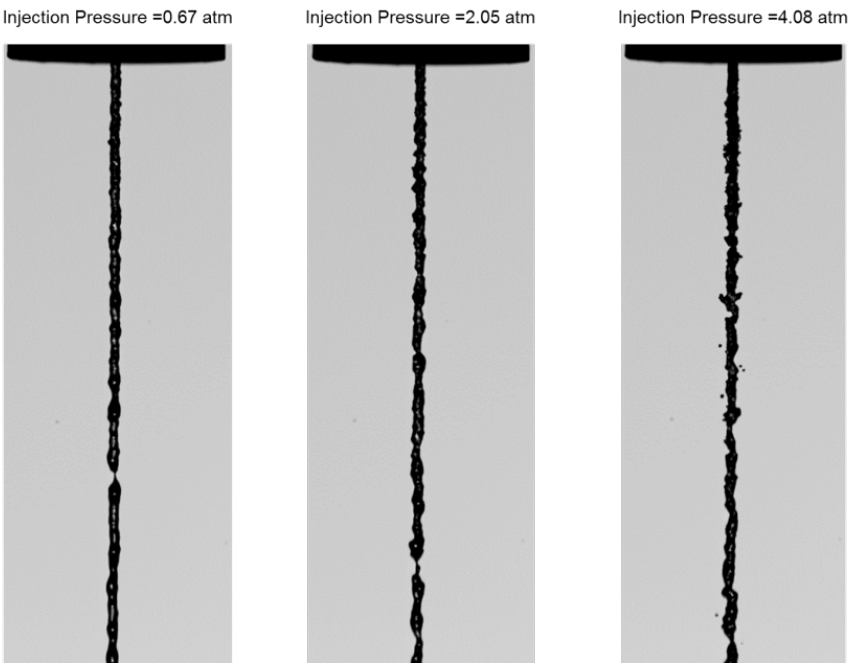

Figure 12. Comparison of nozzle discharge at different injection pressures

The measured liquid mass flow rate is then calibrated against the injection pressure as plotted in Figure 13.

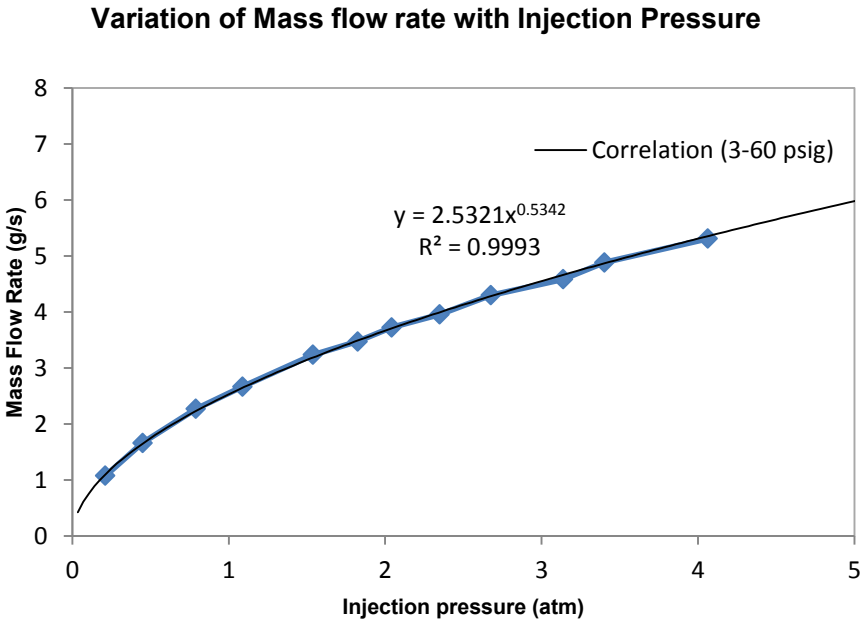

Figure 13. Liquid mass flow rate calibrated against injection pressure

2.3.2 Liquid Mass flow meter calibration

The liquid mass flow rate, which is calculated for measuring the discharge coefficient, is simultaneously used to calibrate the mass flow meter. The relationship between the digital read-out and the actual mass flow rate is found to be linear in the mass flow rate range of interest, as shown in Figure 14.

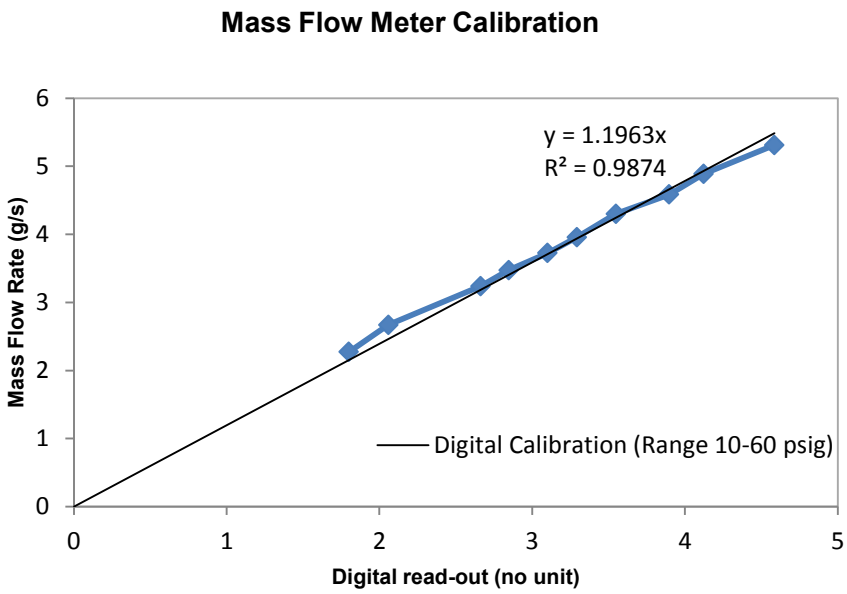

Figure 14. Liquid mass flow meter calibration

2.3.3 Calibration of crossflow air modulation level

The crossflow modulation level (MDL), defined as the ratio of Root Mean Square (RMS) of the crossflow velocity fluctuation to the mean crossflow velocity, is measured during the experiments at the dynamic pressure sensor locations immediately upstream of the nozzle. It was found during calibration that the modulation level in the test-section can vary from the upstream location due to the presence of standing waves. The presence of nodes and antinodes of pressure (and velocity) could affect the response of the liquid spray to the crossflow. For example, consider Figure 15 and Figure 16 which show the velocity fluctuation from mean and its Fast Fourier Transform (FFT) spectrum for a typical case (We=175) with crossflow modulation at 90 Hz at two different locations in the test rig. The difference in the velocity levels is apparent and the actual level at the injector location needs to be calculated. The method to obtain velocity fluctuation level measurements at various locations in the test-section is detailed next.

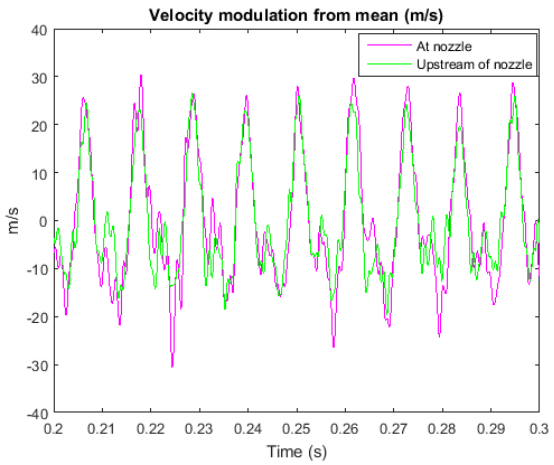

Figure 15. Velocity fluctuations at nozzle and upstream location

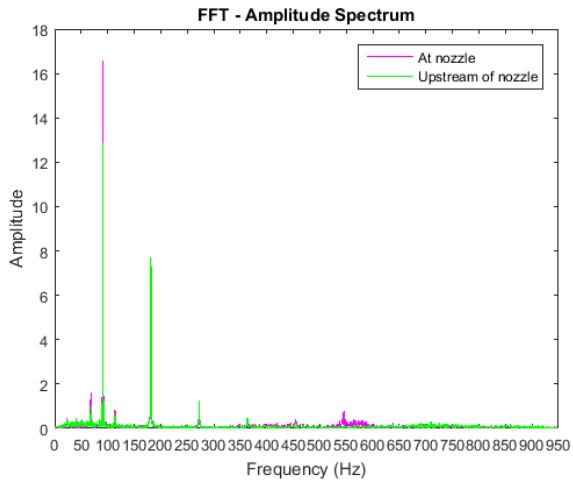

Figure 16. FFT of velocity fluctuation at nozzle and upstream location

A stainless steel window with a dynamic pressure port 'E' was designed such that the port would be at a distance of 57.15 mm (2.25 inches) from the closest upstream dynamic pressure sensor 'C', and the midpoint of the two pressure sensors would be at the nozzle plane. This window was used in place of one of the fused silica side windows during the calibration tests. The schematic of the modified setup for calibrating the modulation level is shown in Figure 17. Thus a total of five pressure sensors (A-E) were used to find the modulation level at various points in the test-section. With this setup, the modulation level desired at the nozzle plane can be set and the corresponding modulation level at the various other pressure sensing locations are calculated. These conditions are then used during the experiments when the modulation level would be set by monitoring the upstream pressure signals.

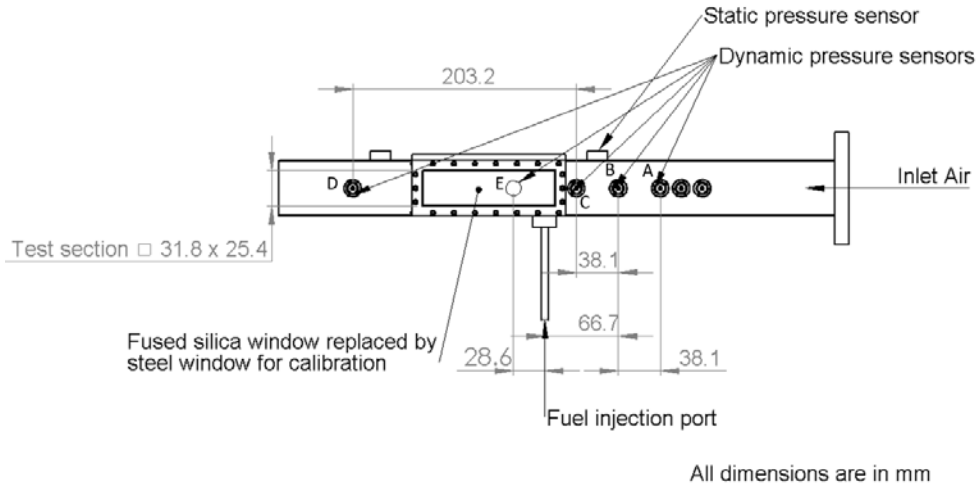

Figure 17. Schematic of the test rig showing the pressure sensor ports used in calibration

2.4 Experimental procedure

The experimental conditions are set by controlling a number of parameters. To set a desired crossflow Weber number at a particular static pressure, the air from the compressor is regulated to more than twice the desired static pressure in the test-section. Then the mass flow rate is set by monitoring the mass flow sensor reading. The pressure in the test-section is controlled by operating the back-pressure valve.

The momentum flux ratio is then controlled by setting a suitable value of the liquid mass flow rate and injection pressure, arrived at from the calibration. The desired modulation frequency is achieved by varying the rotations per minute of the DC motor which drives the siren. The modulation level is controlled by adjusting the amount of air flow through the siren and its bypass. Both the modulation frequency and modulation level are monitored in real-time using LabVIEW interface.

3 Liquid Jet Near-Field Analysis

The spray field of a liquid jet in crossflow consists of the liquid jet column penetrating into the crossflow, which is broken down and atomized by various processes. The liquid in the jet column preserves its momentum upon injection until it is bent by the crossflow, and momentum exchange commences. The penetration of both the liquid column and the resulting spray are thus dependent upon the initial liquid column trajectory. The analysis of the response of the liquid column to the oscillations in the crossflow would thus be the logical first step in characterizing the liquid jet penetration in oscillating crossflows.

From the literature, it can be deduced that the momentum flux ratio (q) is the major parameter in defining the column trajectory. Especially in the immediate vicinity of jet injection, the momentum flux ratio can be used to satisfactorily define the column trajectory before the surface phenomena on the column, due to the interaction with the crossflow, become dominant. Therefore, a method is developed to study the response of the jet using momentum flux ratio extracted from the high speed camera images in the near-field, which is defined to be within 8 jet diameters downstream of the injection location (x/d<8).

3.1 Liquid Column Trajectory Correlation

The jet column breakup location in the crossflow direction, x_{Br}/d, has been calculated in a number of previous studies by various researchers, as discussed in Section 1.1.3. While the exact breakup location might be dependent on the flow conditions, the liquid column remains largely intact within x/d=6 as was observed from instantaneous images at low Weber numbers. To study this near-field region of the liquid column, correlations similar to the form shown in Eq. (10),

where c_1, c_2 and c_3 are unknown coefficients, were fitted to the windward column trajectories extracted from high-speed camera images.

$$\frac{y}{d} = c_1 * q^{c_2} * \left(\frac{x}{d}\right)^{c_3} \quad (10)$$

It was observed that the correlations from the literature over-predict the actual column trajectory in a majority of the cases. Therefore, shadowgraph images were acquired over a wide range of flow conditions listed in Table 2, in order to develop a correlation that fits the observed data rigorously.

Table 2. Test Conditions to obtain near-field trajectory correlation

Air crossflow pressure, P_a (atm)	2.04, 3.06
Air crossflow density, ρ_a (kg/m^3)	2.46, 3.67
Weber number, We	8 – 175
Air crossflow velocity, v_a (m/s)	21.77 – 101.81
Air crossflow temperature, T (K)	293
Liquid	Water
Liquid density, ρ_j (kg/m^3)	998
Liquid surface tension, σ (N/m)	7.28 x 10^{-2}
Liquid jet velocity, v_j (m/s)	3.62 – 21.44
Momentum flux ratio, q	5 - 37

The column trajectory points were extracted from averaged images obtained from a series of instantaneous high-speed images using an algorithm described in Appendix B. The points within *x/d* of 6 were used for developing the correlation in the near-field. A non-linear regression analysis was performed on the data to obtain the correlation given in Eq. (11).

$$\frac{y}{d} = 1.3265 * q^{0.4131} * \left(\frac{x}{d}\right)^{0.5464} \qquad (11)$$

A comparison of the correlation developed in this study with two other correlations from the literature is presented for two different cases in Figure 18 and Figure 19. It is evident from the figures that the proposed correlation fits the liquid column very closely within *x/d*=6 while the correlations proposed by Wu et al. [3] and Stenzler et al. [14] over-predict the penetration. The non-linear regression model had an associated R-Squared value of 0.941.

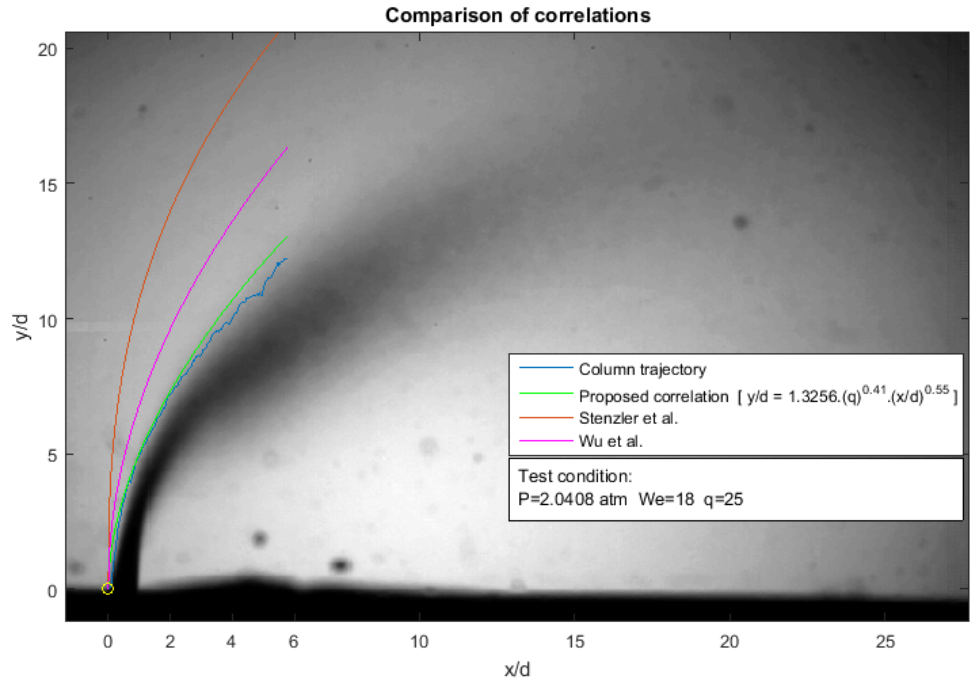

Figure 18. Comparison of correlations: Case1

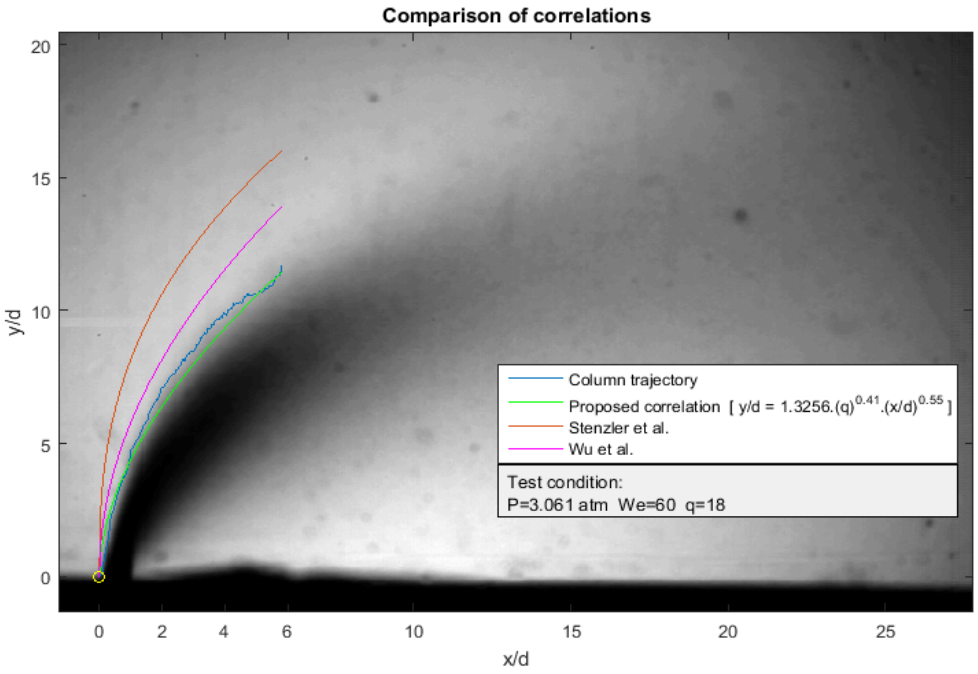

Figure 19. Comparison of correlations: Case 2

Since Wu et al.'s correlation is closer to the proposed correlation, a comparison of the two models is presented in Figure 20 where the observed y/d of points extracted from the images covering a wide range of test conditions is plotted against the expected y/d from the two correlations. The linear trend line fits the data well for both the models but the model proposed in this study has a better fit and a slope very close to unity, signifying the goodness of fit.

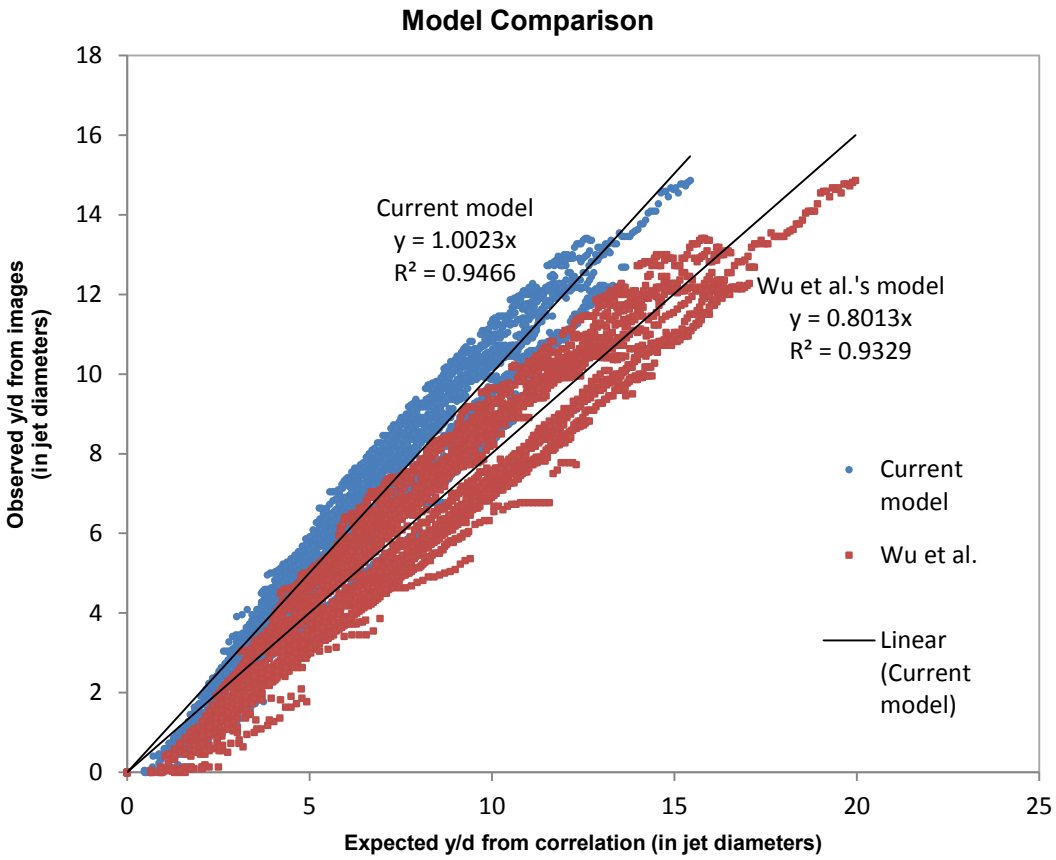

Figure 20. Comparison between fit of proposed correlation and Wu et al.'s correlation

3.2 Analysis of Liquid Jet Column Response to Crossflow Modulation

The next logical step is to use the correlation to study the variation in jet penetration in the presence of crossflow oscillations. Table 3 lists the test-conditions under which high-speed camera images and pressure signals were obtained for studying the jet column response. The Weber numbers are chosen in order to represent the different breakup regimes (bag, multimode and shear) and the modulation frequencies are selected to study the effect of timescale of crossflow oscillation.

Table 3. Test Conditions for Near-field Analysis

Parameters	**Range**
Air crossflow static pressure, P_a (atm)	2.04, 3.06
Air crossflow density, ρ_a (kg/m^3)	2.46, 3.67
Weber number, *We*	18 – 250
Air mean crossflow velocity, v_a (m/s)	26.66 – 121.69
Air crossflow temperature, T (K)	293
Liquid (water) density, ρ_j (kg/m^3)	998
Jet nozzle diameter, d (m)	0.5 x 10^{-3}
Liquid surface tension, σ (N/m)	7.28 x 10^{-2}
Liquid jet velocity, v_j (m/s)	5.12 – 25.62
Momentum flux ratio, q	10 – 30
Air crossflow modulation level, (MDL=RMS(v_a')/v_a)	5 – 20
Crossflow modulation frequency, f	90 - 450

For each test case, 1722 images are recorded at a frame rate of 10,000/second with an exposure time of 1 μs. The main consideration in choosing the frame rate is to make sure that the images contain data from an adequate number of phases of the modulating frequency. The exposure time has to be short enough to record transient details about the flow field in each image.

Figures 21-23 illustrate the liquid column movement in response to oscillating crossflow for three different cases. All three cases pertain to momentum flux ratio of 18 and a modulation level

of 10%. Figure 21 shows the jet response in a crossflow with a Weber number of 18 and modulation frequency of 90 Hz. Figure 22 and Figure 23 both show the behavior of a jet in a crossflow of Weber number 175, with the former in a crossflow modulated at 90 Hz and the latter in a modulated crossflow at 450 Hz.

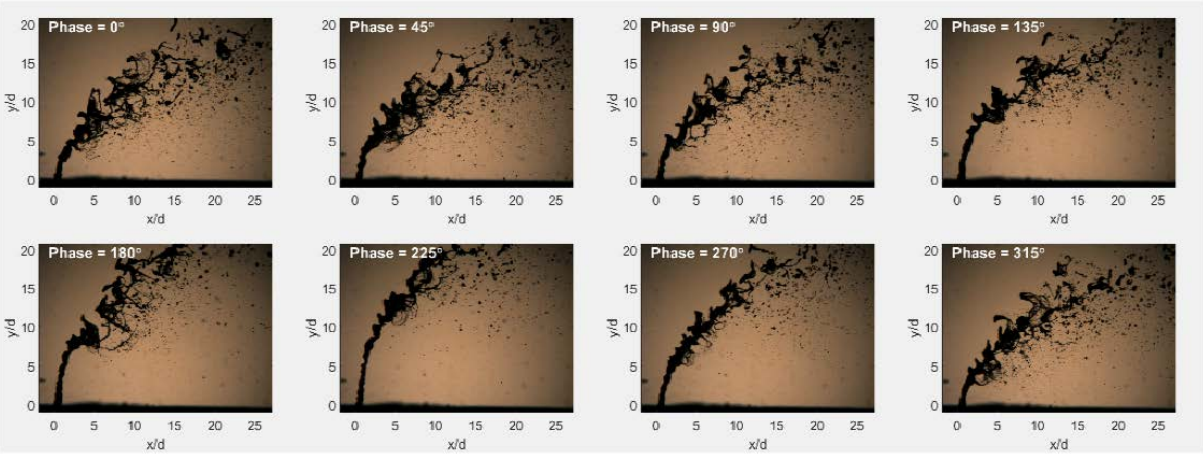

Figure 21. Montage of instantaneous images at different phases – Case 1: P=2.04 atm We=18 q=18 f=90 Hz MDL=10%

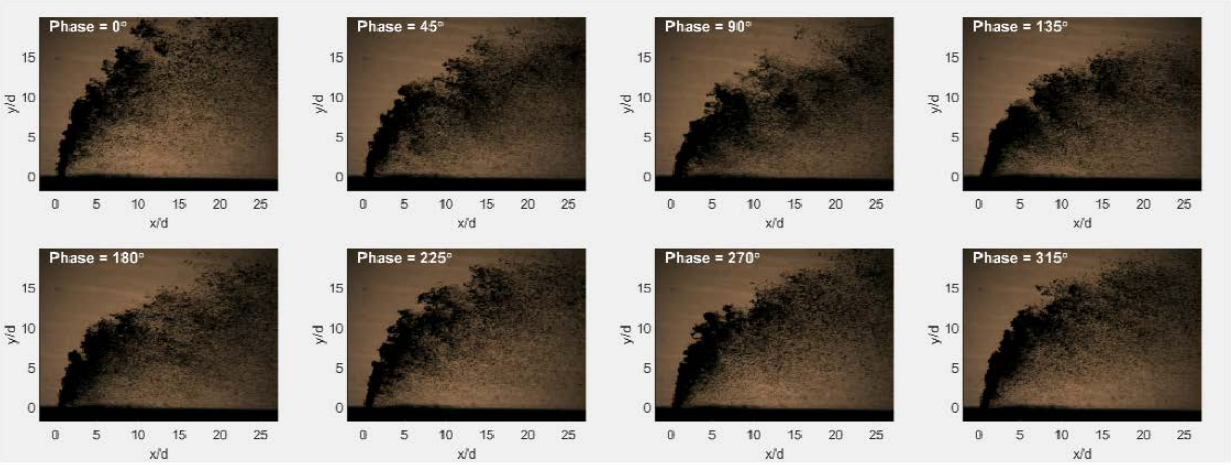

Figure 22. Montage of instantaneous images at different phases – Case 2: P=2.04 atm We=175 q=18 f=90 Hz MDL=10%

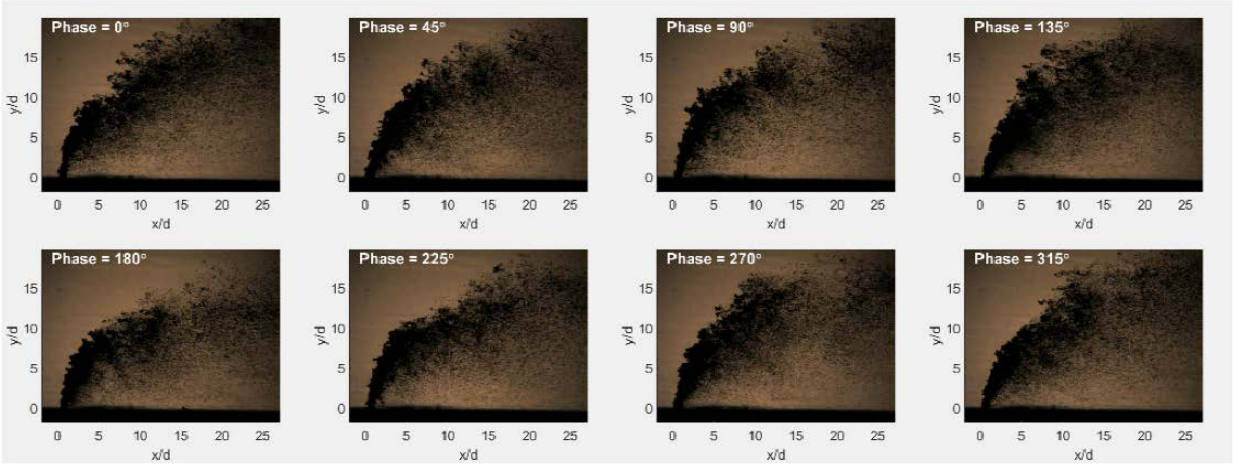

Figure 23. Montage of instantaneous images at different phases – Case 3: P=2.04 atm We=175 q=18 f=450 Hz MDL=10%

Qualitatively, it can be observed that the response of the jet to the crossflow modulation exists in all the above cases to different degrees. There are changes in the spray structures too, such as the location of column breakup point, during the course of one period of oscillation. Restricting the focus to the windward column trajectory, it becomes apparent that a suitable method to compare the different responses needs to be developed. It is also worth noting that in the lower Weber number case (Figure 21), the liquid column appears to break between *x/d* of 5 and 10 with the formation of bag-like structures. In the higher Weber number cases (Figure 22 and Figure 23), the dominant mode is clearly shear breakup.

To quantitatively analyze the liquid column behavior in the various flow conditions, the following procedure was conceived.

3.2.1 Analysis Procedure

The procedure is explained by illustrating the three cases corresponding to Figure 21, Figure 22 and Figure 23. The image processing is performed using MATLAB.

- The high speed camera images are first converted from RGB to grayscale images. Then, a threshold of 10% is used to convert the individual images to binary images with the pixels having grayscale intensities less than the threshold being assigned a value 0 and the rest of the pixels being assigned a value 1. The boundaries are then extracted from the thresholded images and the windward column trajectory points are isolated.
- Using the correlation developed in Eq. (11), a least squares fit is used to find the value of momentum flux ratio (q) corresponding to the curve that had the best fit to the column trajectory in each image. Figure 24 and Figure 25 show sample frames from two different test cases with the boundary of the thresholded images in blue, the boundary within *x/d*=2 in green and the curve fit using the correlation in white. Video 1 shows the process of curve fitting and extraction of corresponding momentum flux ratio data from each frame for the first case.

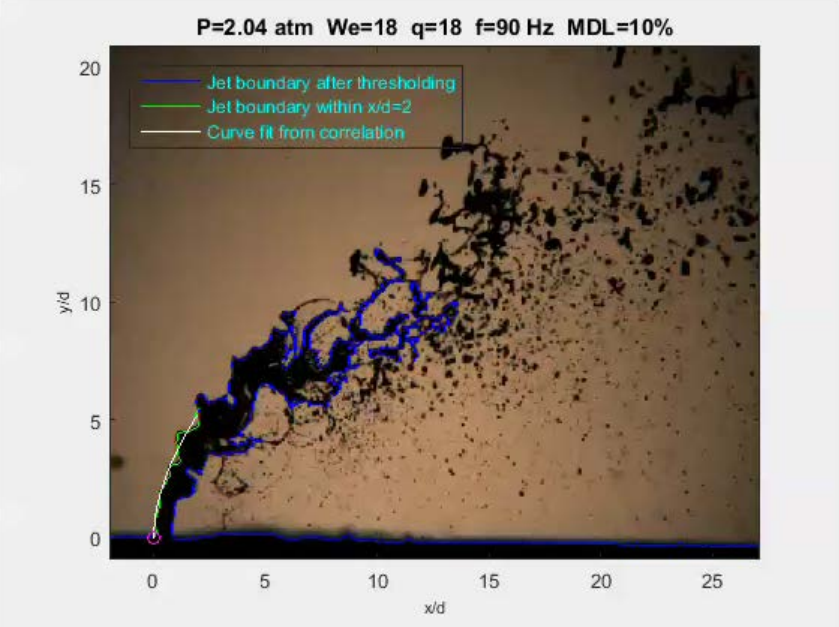

Figure 24. Illustration of curve fitting to the windward trajectory: Case - P=2.04 atm We=18 q=18 f=90 Hz MDL=10%

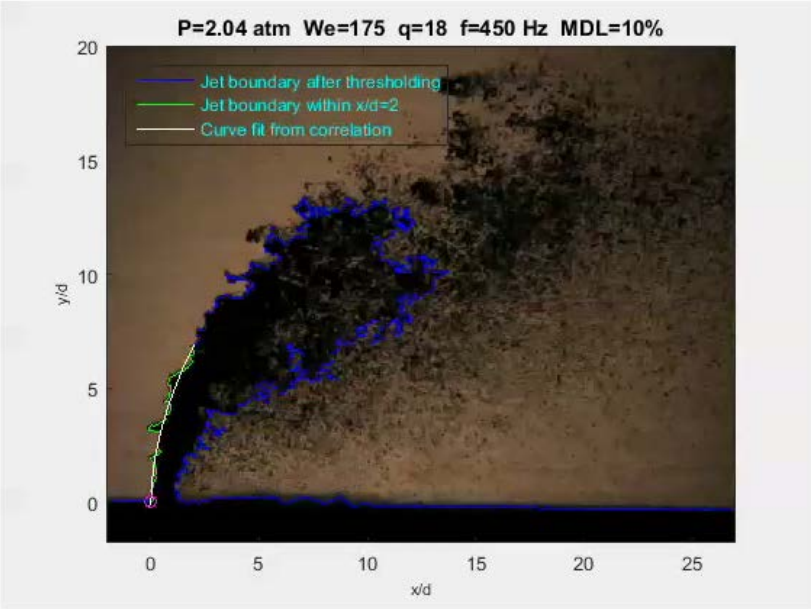

Figure 25. Illustration of curve fitting to the windward trajectory: Case - P=2.04 atm We=175 q=18 f=450 Hz MDL=10%

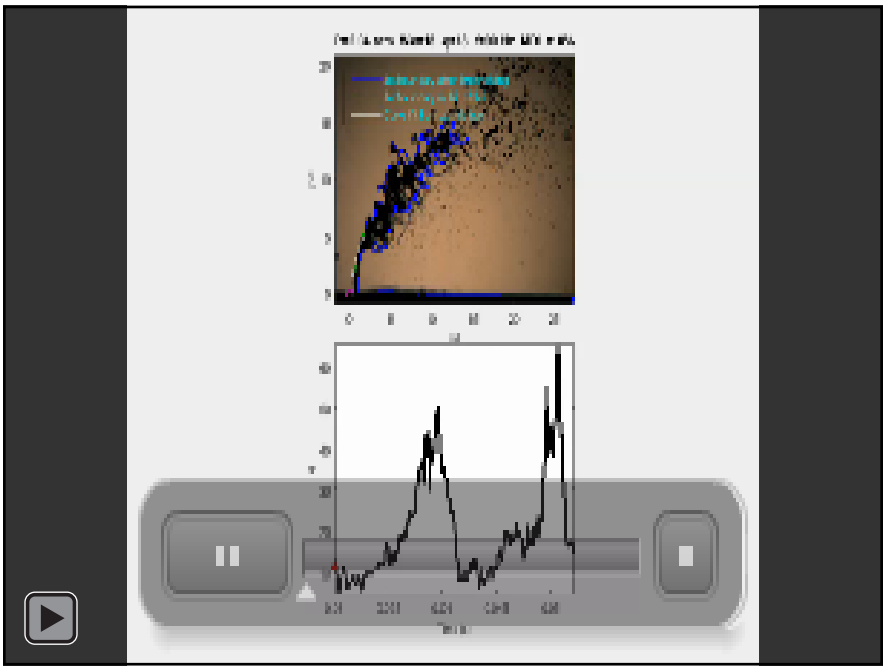

Video 1. Illustration of curve fitting and momentum flux ratio trace: Case 1 - P=2.04 atm We=18 q=18 f=90 Hz MDL=10% [Legend: Blue – Boundary from thresholded imaged; Green – Boundary within x/d=2; White – Curve fit]

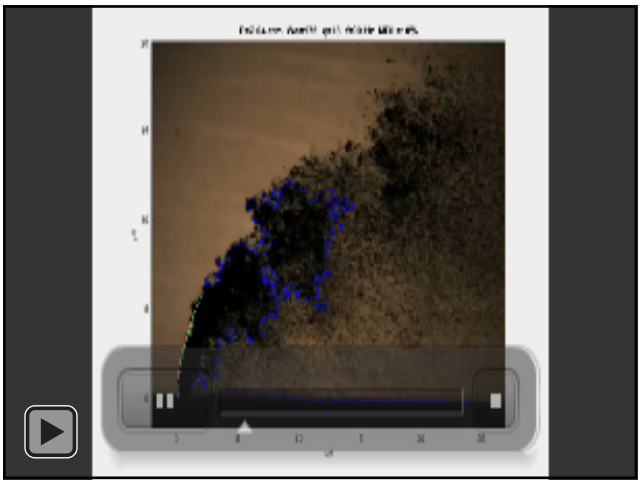

Video 2. Illustration of curve fitting: Case 2 - P=2.04 atm We=175 q=18 f=90 Hz MDL=10% [Legend: Blue – Boundary from thresholded imaged; Green – Boundary within x/d=2; White – Curve fit]

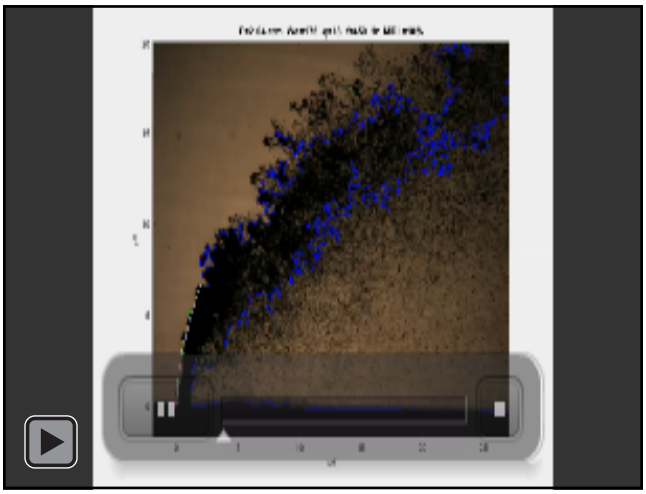

Video 3. Illustration of curve fitting: Case 3 - P=2.04 atm We=175 q=18 f=450 Hz MDL=10% [Legend: Blue – Boundary from thresholded imaged; Green – Boundary within x/d=2; White – Curve fit]

- The time trace of momentum flux ratio is then extracted from the images. FFT is performed on the data to identify the fundamental frequency. Figure 26 and Figure 27 show the time trace of momentum flux ratio and the amplitude spectrum respectively. It can be observed from the spectrum that there is clearly a peak at the modulating frequency of 90 Hz and its higher harmonics, giving an indication of the response of the liquid jet column.

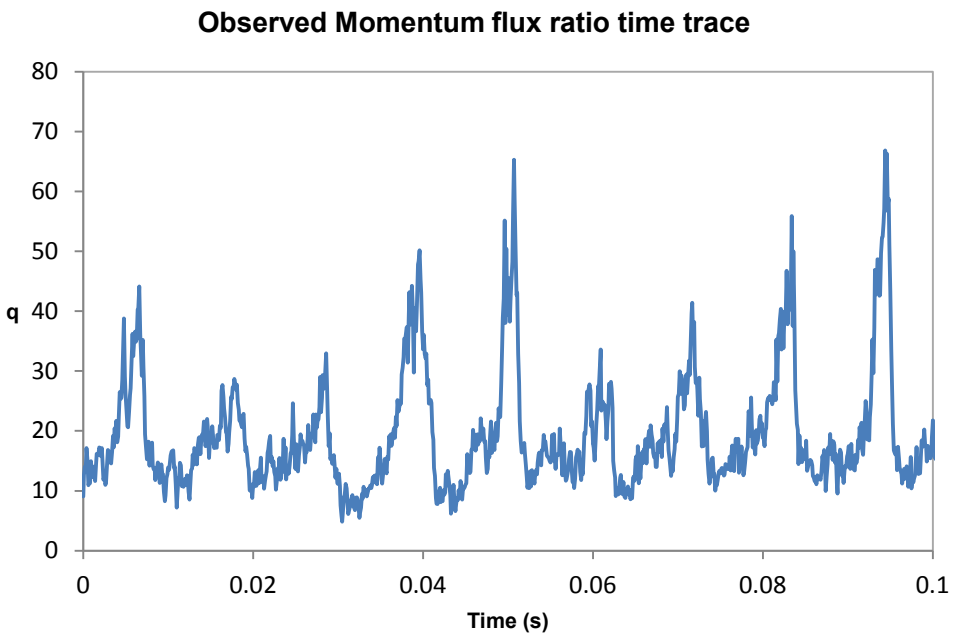

Figure 26. Momentum flux ratio time trace: Case 1 - P=2.04 atm We=18 q=18 f=90 Hz MDL=10%

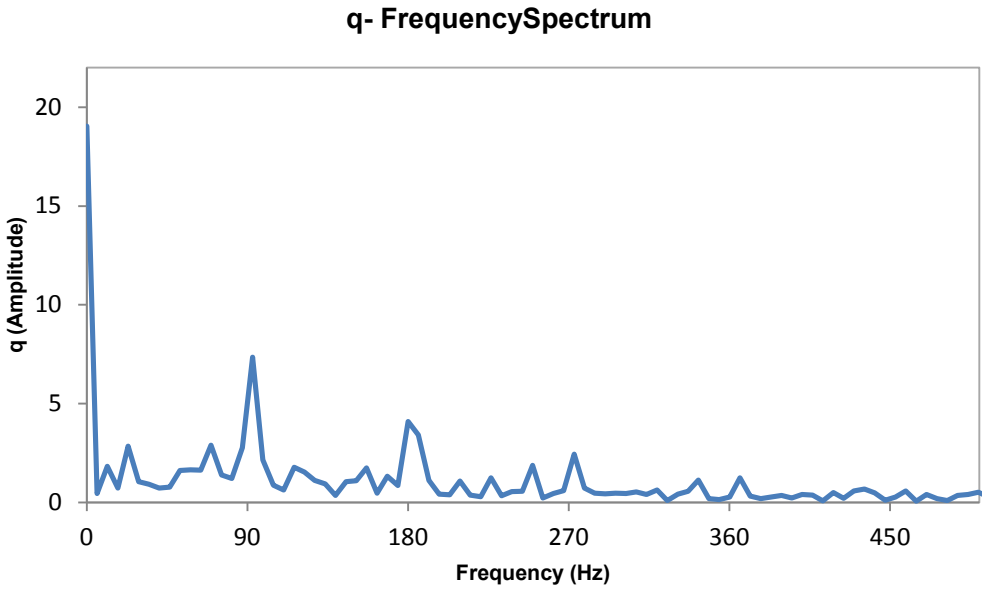

Figure 27. Amplitude spectrum of momentum flux ratio: Case 1 - P=2.04 atm We=18 q=18 f=90 Hz MDL=10%

- The 2-microphone method is simultaneously used to acquire the instantaneous pressure signals, and thus calculate instantaneous velocity fluctuation. Adding the instantaneous velocity fluctuation to the mean crossflow velocity, the expected instantaneous momentum flux ratio is calculated. Figure 28 shows the instantaneous velocity fluctuation from the mean crossflow velocity measured by the 2-microphone method. Figure 29 shows the corresponding momentum flux ratio that would be expected based upon the instantaneous net crossflow velocity.

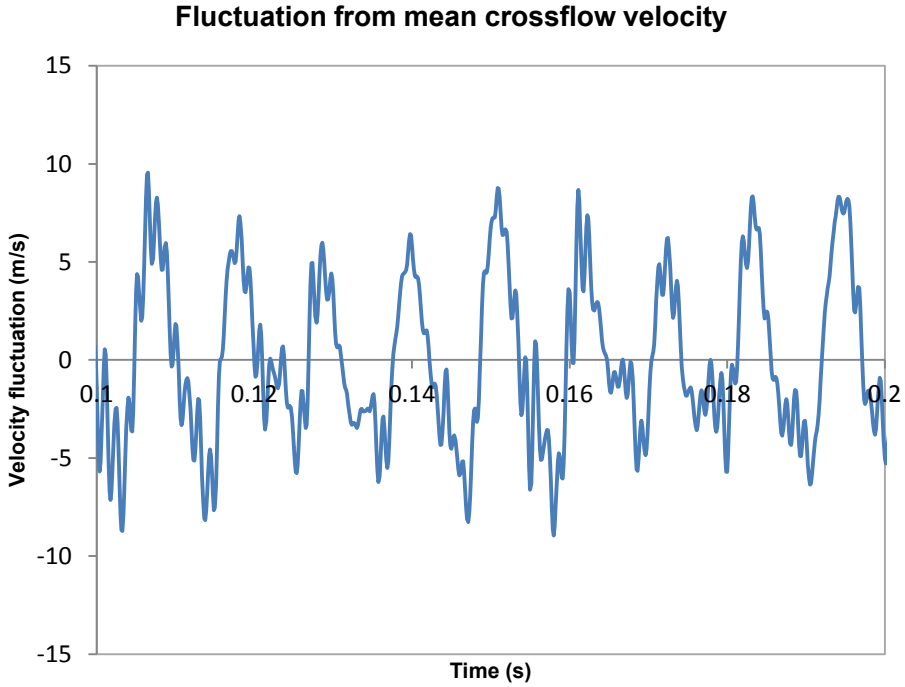

Figure 28. Fluctuation from mean crossflow velocity: Case 1 - P=2.04 atm We=18 q=18 f=90 Hz MDL=10%

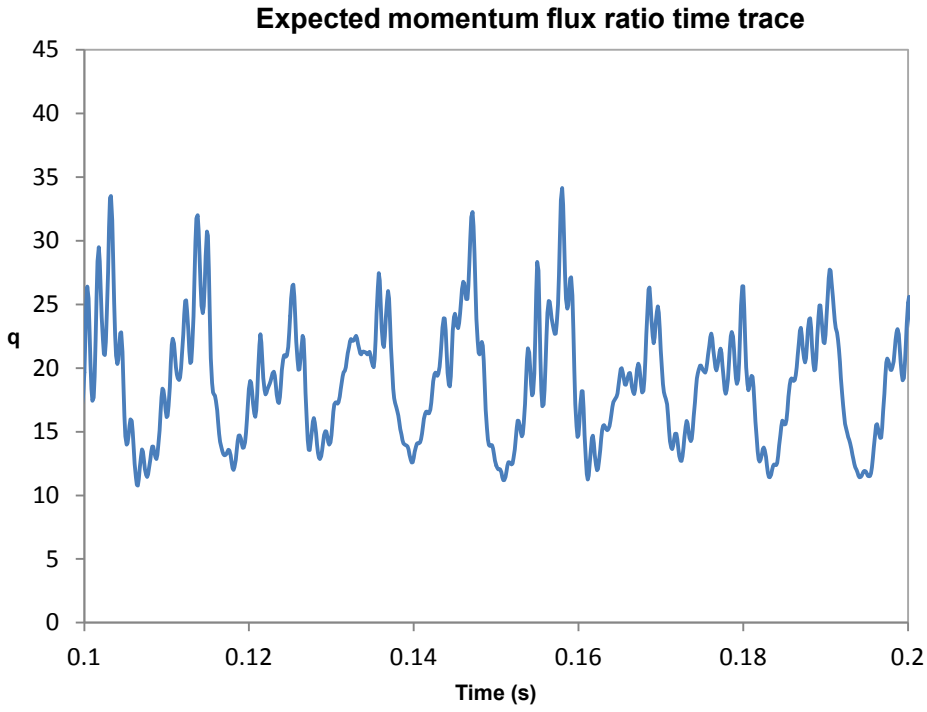

Figure 29. Expected momentum flux ratio time trace: Case 1 - P=2.04 atm We=18 q=18 f=90 Hz MDL=10%

- FFT is again performed on the expected momentum flux ratio calculated in the previous step. Then, a comparison of the spectra from the momentum flux ratio obtained through observation from the images and the momentum flux ratio expected from the instantaneous velocity is performed, as shown in Figure 30.

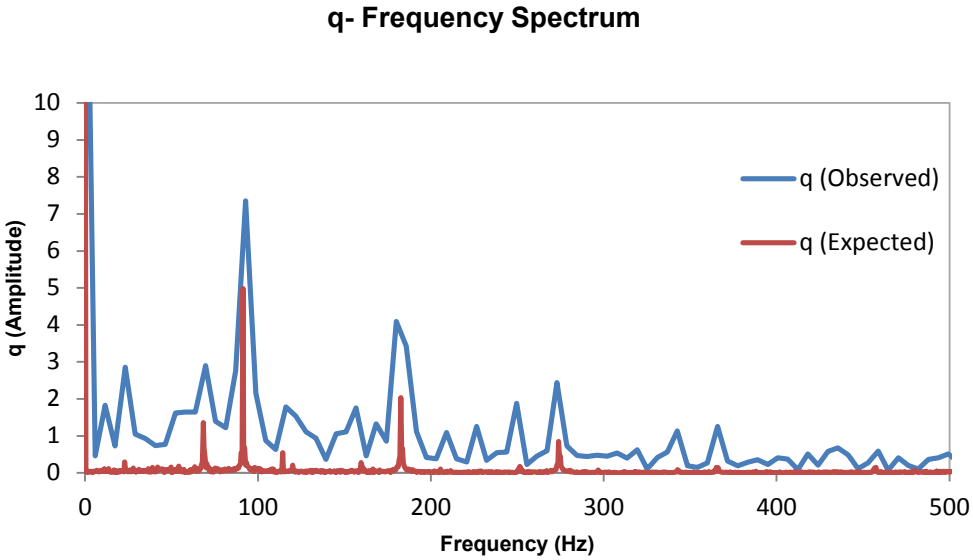

Figure 30. Comparison of observed and expected momentum flux ratio spectra: Case 1 - P=2.04 atm We=18 q=18 f=90 Hz MDL=10%

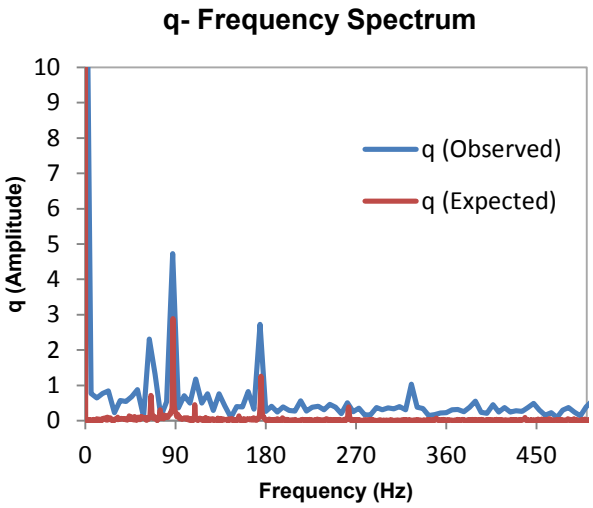

Figure 31. Comparison of observed and expected momentum flux ratio spectra: Case 2 - P=2.04 atm We=175 q=18 f=90 Hz MDL=10%

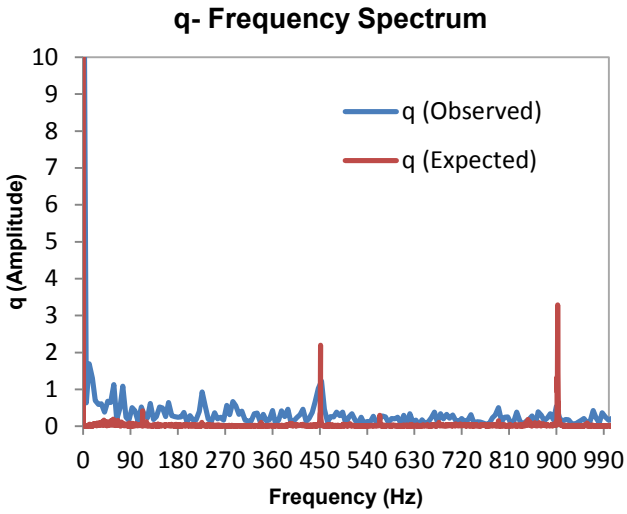

Figure 32. Comparison of observed and expected momentum flux ratio spectra: Case 3 - P=2.04 atm We=175 q=18 f=450 Hz MDL=10%

- It can be observed from the spectra of the three cases in Figures 30-32 that the amplitude of the jet column response, as measured by the parameter momentum flux ratio, shows significant difference with a change in modulating frequency. It should be noted that the frequency resolution of the observed and the expected momentum flux ratio spectra are different, with their values being 5.81 Hz and 0.49 Hz respectively. This is due to the differences in sampling rate and the number of samples obtained in the imaging and pressure signal acquisition systems. Also, the expected momentum flux ratio is calculated based on the signals from the pressure sensors upstream of the nozzle. A correction is required to reflect the velocity level at the nozzle based on calibrations. Therefore, in spite of the amplitude spectra displaying a marked qualitative trend, basing conclusions solely on the amplitude spectrum readouts might be prone to errors.
- To overcome the problem of comparing spectra with different frequency resolutions, the power spectrum is utilized. The utility of comparing power instead of amplitudes in the current study is explained in Appendix C. For each case, the fraction of power in a frequency band of 15 Hz around the interested peak frequency is calculated by dividing the power in the band by the total power in the observed momentum flux ratio signal. Similarly, the power fraction in the expected momentum flux ratio spectrum is also calculated after correcting for the velocity level differences between the upstream measurement location and the nozzle location.
- Since the power equals square of the RMS amplitude in the time domain, the square root of the power fraction is equal to the RMS amplitude in the frequency band of interest normalized by the RMS amplitude of the entire signal. The ratio of the normalized RMS amplitudes of the observed momentum flux ratio to the expected momentum flux ratio is

then analogous to the respective normalized amplitude ratio. This quantity is therefore very useful in comparing the amplitude gains accurately and will be hereafter referred to as Normalized Amplitude Ratio (*NAR*). *NAR* can be expressed as Eq. (12).

$$\text{Normalized Amplitude Ratio} = \sqrt{\frac{\dfrac{\text{Power at the modulation frequency in the response signal}}{\text{Total power in the response signal}}}{\dfrac{\text{Power at the modulation frequency in the input signal}}{\text{Total power in the input signal}}}} \quad (12)$$

For an input signal *g(t)* and response signal *h(t)*, where *t* is discrete time from 0 to *n*, *G* and *H* represent the amplitudes of *g* and *h* in the frequency domain respectively, *f* represents frequencies in a narrow band around the modulation frequency (15 Hz band used in this study), and f_1 and f_2 represent the bounds of the frequency band of interest, *NAR* can be expressed as Eq. (13).

$$NAR = \sqrt{\frac{\left(\dfrac{2\sum_{f_1}^{f_2}|H(f)|^2}{\left(\dfrac{\sum_{t=0}^{n}|h(t)|^2}{n+1}\right)}\right)}{\left(\dfrac{2\sum_{f_1}^{f_2}|G(f)|^2}{\left(\dfrac{\sum_{t=0}^{n}|g(t)|^2}{n+1}\right)}\right)}} \quad (13)$$

The procedure is summarized in the form of a flowchart in Figure 33. While calculating power at the interested frequency, the power is calculated in a 15 Hz band around the interested frequency to account for the differences in the frequency bin location from FFT spectrum and the actual interested frequency.

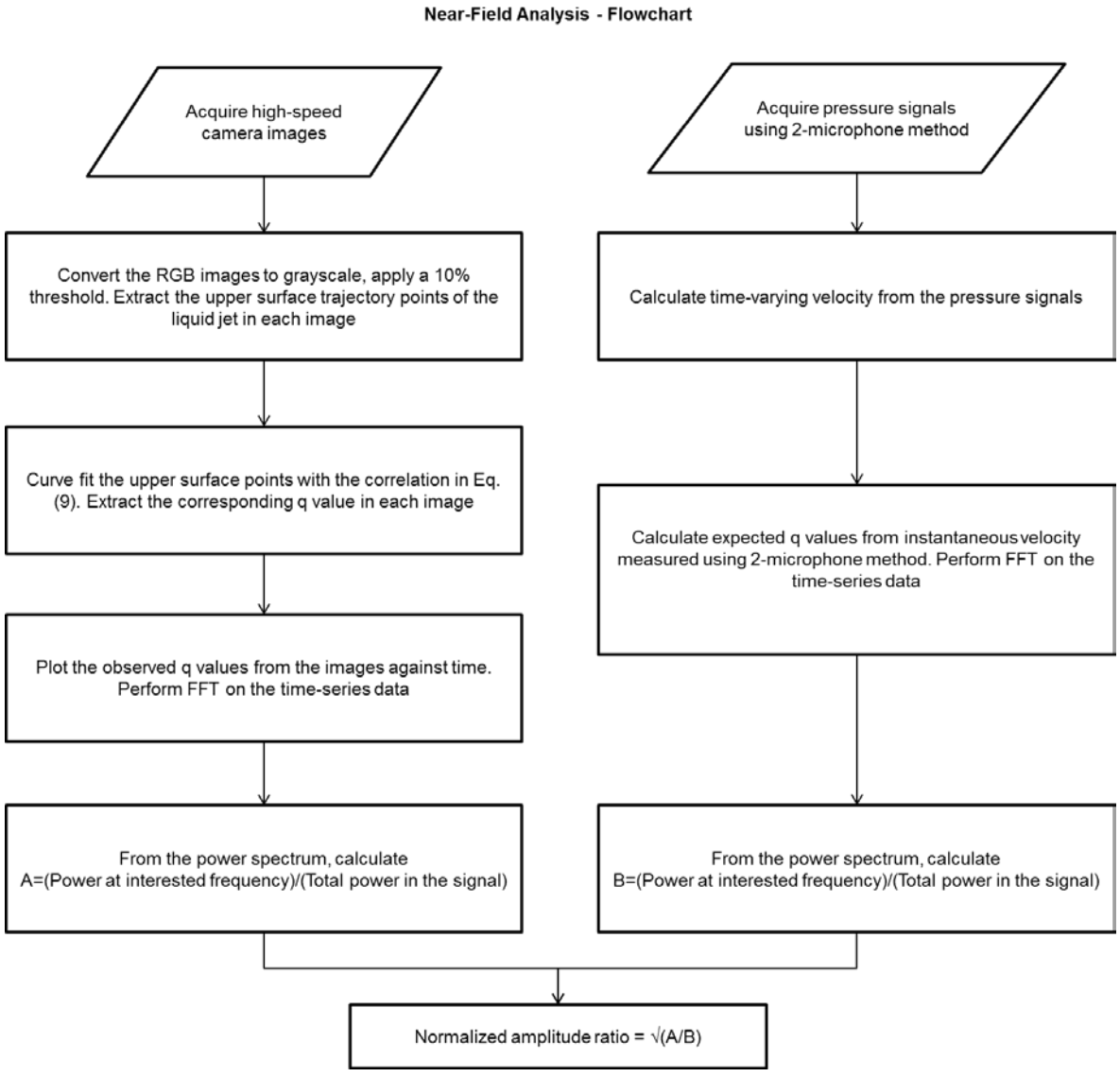

Figure 33. Flowchart summarizing the steps involved in near-field analysis

3.2.2 Results

FFT was performed on the observed and expected momentum flux ratios and normalized amplitude gains were calculated for a wide range of test conditions to study the effect of oscillation frequency, modulation level and other factors.

3.2.2.1 Effect of oscillating crossflow on the liquid column trajectory

The primary question of whether the liquid column responds to the crossflow oscillations is answered by taking a look at the momentum flux ratio amplitude spectra. Figure 34 is a reproduction of the observed and expected momentum flux ratio spectra for Case 3 showing a wider frequency range. It is clear from the spectrum that the liquid column has a strong response at the modulating frequency. It is interesting to note that the column also responds in varying degrees to the higher harmonics in the modulated crossflow and that this response, though weaker, is evident even at frequencies over 1000 Hz. The higher harmonics are thought to be present as a result of the interaction of the crossflow with the standing waves in the test rig. The response of the jet at higher harmonics with velocity fluctuation amplitudes greater than or equal to the fundamental is also included for quantitative analysis in the succeeding sections.

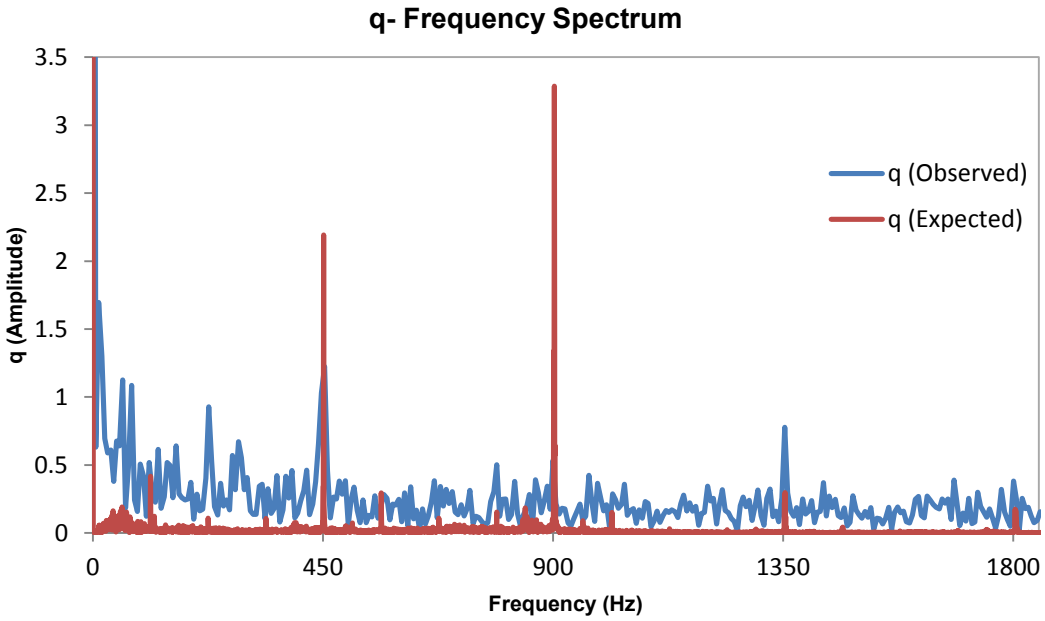

Figure 34. Observed and expected momentum flux ratio spectra: Case 3 - P=2.04 atm We=175 q=18 f=450 Hz MDL=10%

3.2.2.2 Effect of modulating frequency and crossflow Weber number

The normalized amplitude ratio for various Weber numbers with momentum flux ratio of 18 and modulation level of 10% is plotted against oscillation frequency in Figure 35. It can be observed that the amplitude ratio, which is analogous to the amplitude gain, is higher at the lower frequency of f=90 Hz with values closer to unity. This indicates that the liquid jet column fluctuates at an amplitude close to that expected from the input modulation.

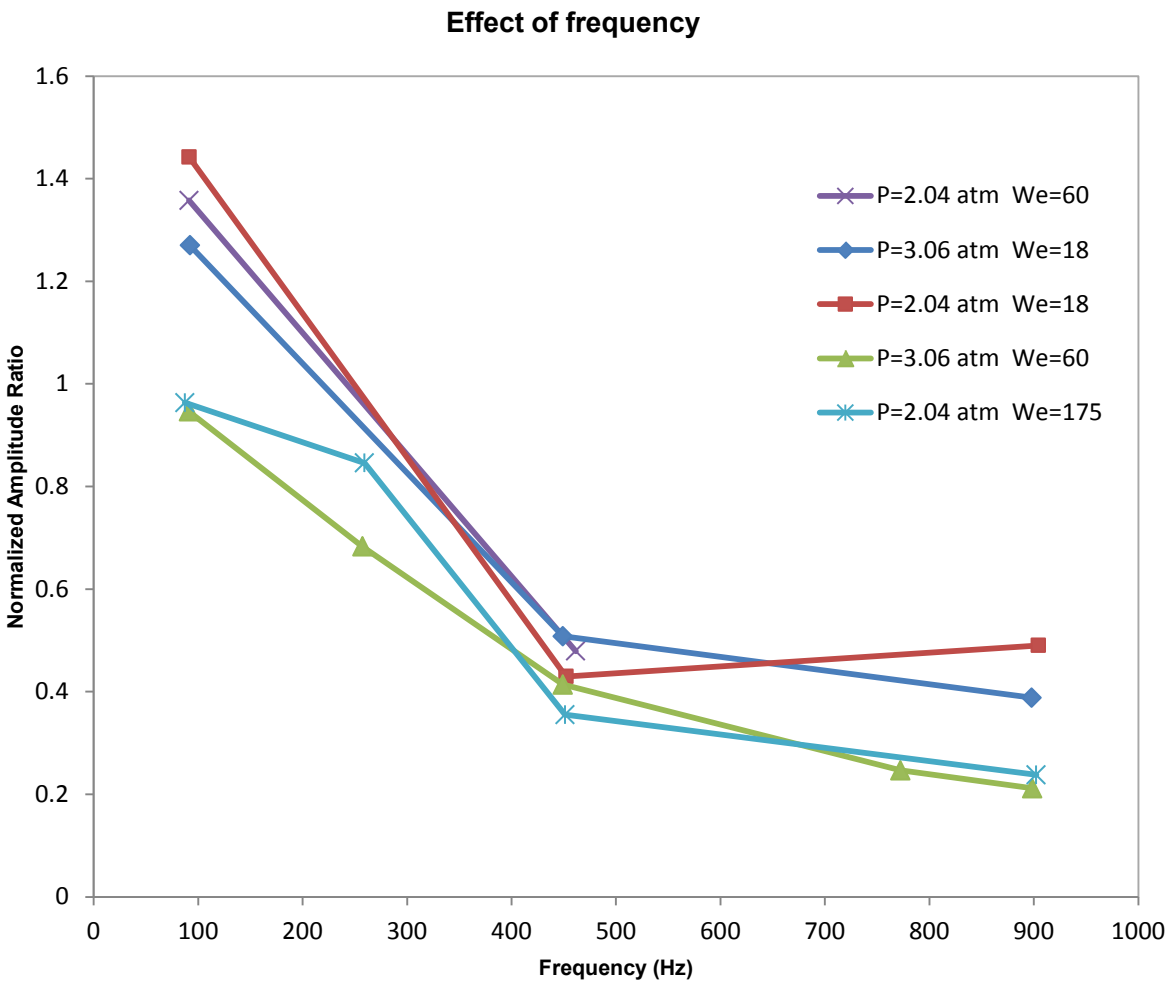

Figure 35. Variation of Normalized Amplitude Ratio with modulating frequency: q=18 and MDL=10% for all cases

As the frequency increases to *f*=260 Hz, the amplitude ratio begins to reduce to values around 0.75 indicating that the jet column fluctuates at a lower amplitude than expected with an increase in frequency. This trend continues to the higher frequencies too, as shown by the cluster of data points at *f*=450 Hz, which have amplitude gains between 0.35 and 0.50. It is notable that the trend remains the same irrespective of the crossflow static pressure and Weber number, hinting at the explanation that the liquid jet response is a function of primarily the input crossflow modulation frequency.

In order to provide a physical explanation for the observed phenomenon, consider the model of a liquid jet in Video 4. The video shows a typical liquid jet in a crossflow of Weber number 18 and static pressure of 2.04 atm, with a momentum flux ratio of 18. The two polar plots show the phase of oscillation for *f*=90 Hz and *f*=450 Hz as the liquid jet emanates from the nozzle. A constant injection velocity is assumed for the liquid jet in this illustration since the region of interest is within *x/d*=6.

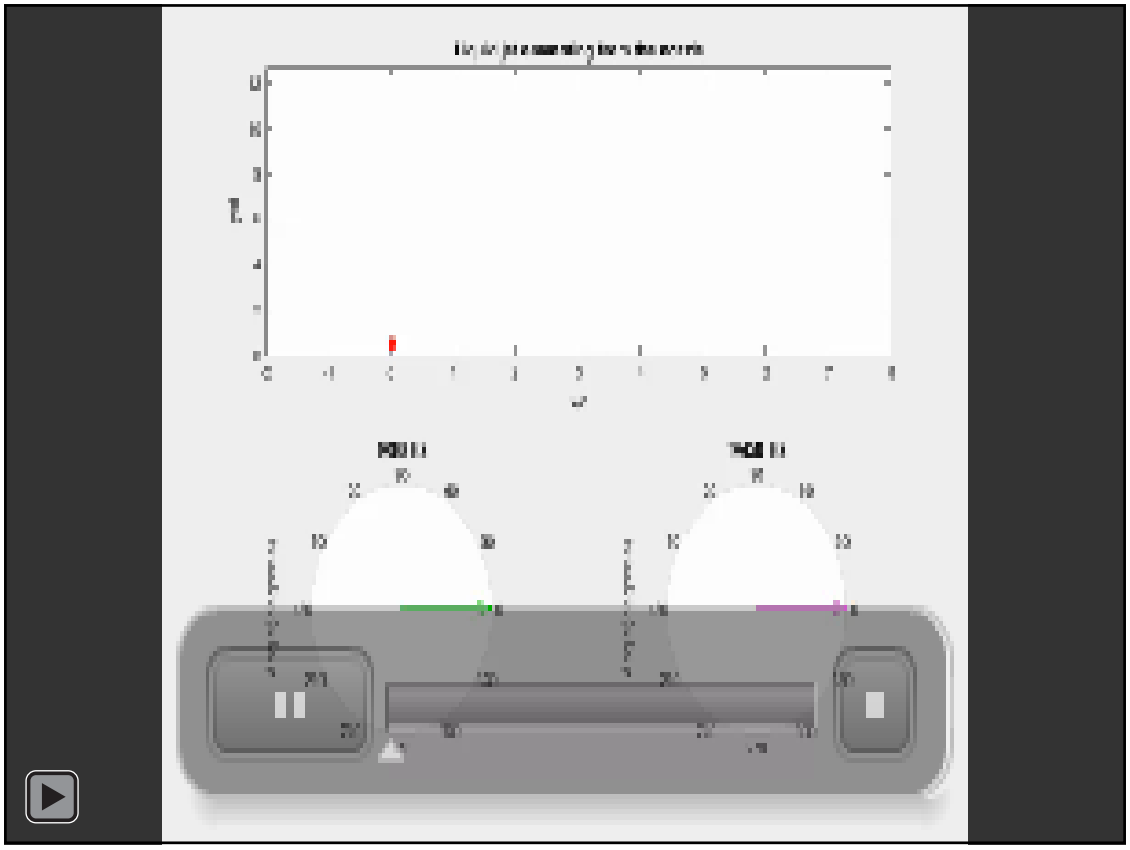

Video 4. Video showing a comparison of the phase of the crossflow fluctuation encountered by the liquid jet in (left) f=90Hz modulated crossflow and (right) f=450 Hz crossflow

When a liquid jet is injected into a crossflow, the liquid column gets deformed by the crossflow and breaks up at the column breakup point. The instantaneous momentum flux ratio depends upon the ratio of dynamic pressure of the liquid jet to the dynamic pressure of the crossflow, and

is thus indicative of the "degree of bend" in the trajectory of the liquid column. In a modulated crossflow such as the one under study, the liquid dynamic pressure is maintained constant while the crossflow dynamic pressure fluctuates with the velocity, thereby providing scope for a fluctuation in the momentum flux ratio, causing a flapping action of the liquid column.

Comparing the two frequencies f=90 Hz and f=450 Hz in Video 4, it is apparent that the relative angular velocity of crossflow oscillation encountered by the liquid jet upon injection is going to be different at the two frequencies. The liquid jet in the same flow conditions sees a phase difference of ϕ=137.31° between the injection location and x/d=6 in f=450 Hz crossflow, whereas the jet would see a phase difference of only ϕ=27.46° in f=90 Hz crossflow. The relative phase for different downstream points with respect to the nozzle is given in Table 4.

Table 4. Comparison of the phase difference between injection location and downstream locations for f=90 Hz and f=450 Hz

Axial location in x/d	Relative phase for f=90 Hz (in degrees)	Relative phase for f=450 Hz (in degrees)
0	0	0
1	4.63	23.13
2	9.18	45.89
3	13.73	68.66
4	18.36	91.79
5	22.91	114.55
6	27.46	137.31

The surface tension of the jet liquid tends to preserve the shape of the liquid in order to have the least surface energy. At low crossflow modulation frequencies, since the angular frequency is small, the liquid jet can exit the injector, interact with the crossflow and reach the column breakup point within a small phase difference. Since the difference in phase is smaller, the conservative action of the surface tension has more time to maintain uniformity of the jet column, and thus respond steadily to the crossflow oscillation. If the liquid column can be considered to be a series of cylindrical packets before injection, each liquid packet would then emanate from the nozzle at a small phase difference from the previous liquid packet. In other words, a liquid packet has sufficient residence time within a small phase difference in the crossflow for the surface tension forces to ensure a steady response to the changes in momentum flux ratio, causing a "flapping" up and down action of the liquid column.

On the other hand, in the case of the higher modulation frequency of f=450 Hz, the liquid jet encounters a phase difference of about 137 degrees within six diameters downstream of the nozzle. Hence, each successive liquid packet is subjected to a larger phase difference, thus encountering a larger momentum flux ratio difference. In other words, the different points in the liquid column experience different momentum flux ratio within a shorter axial distance. This rapid change in momentum flux ratio would then attempt to have different penetration of the liquid jet at different points but will be counteracted by the conservative action of surface tension force. Therefore, since the rate of change of phase is high enough that the liquid column cannot align itself to one particular phase, the amount of up and down "flapping" is expected to be dampened while the slope of the windward trajectory is expected to vary with downstream distance in the near-field.

Evidence for this effect can be observed in Figure 36 and Figure 37, which show the instantaneous spray images at f=90 Hz and f=450 Hz crossflow respectively for the same test condition of P=2.04 atm, Weber number=18 and momentum flux ratio=18. The images are acquired at a time lag of 0.1 ms and the first image in the sequence is arbitrarily given a phase of zero degrees. It is seen in the images in Figure 36 that within 0.8 ms and a phase difference of 25.92 degrees, the liquid jet, and the spray after column breakup, display a predominantly uniform trajectory. The white lines in the images indicate that the liquid column and the large bag like structures follow the same trajectory in the near-field region. Thus, any flapping motion observed in the liquid column is also observed in the resulting spray in the near-field.

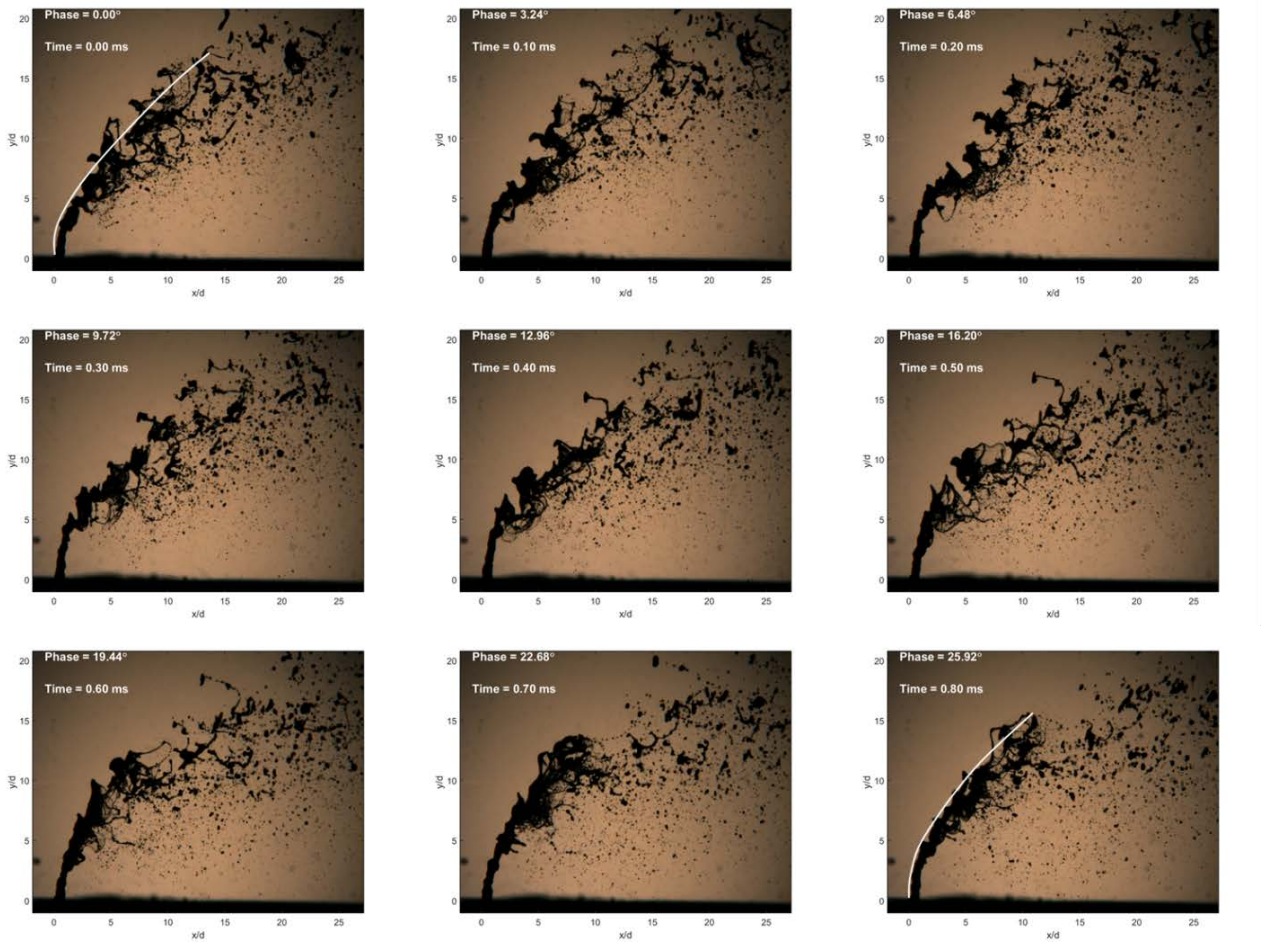

Figure 36. Instantaneous spray images in f=90Hz crossflow within 0.8 ms : Test condition - P=2.04 atm We=18 q=18 MDL=10%

The instantaneous images in Figure 37, corresponding to the 450 Hz modulation, show a different phenomenon. As hypothesized in the jet response model, it is seen that while the jet upon injection is bent in a certain trajectory, there are variations in the trajectory due to variations in the momentum flux within the small downstream distance. These variations in momentum flux are experienced at such a high rate that the jet is unable to respond uniformly to the changes in momentum flux. For instance, the image at phase difference of 16.20 degrees shows that while the liquid column begins to bend more in the crossflow direction, the bag

structures after column breakup preserve their earlier higher momentum flux and penetrate higher. While the smaller droplets can be expected to respond to the higher rate of change of momentum flux, the liquid column itself contends with surface tension and inertial effects. Therefore, the frequency of modulation of crossflow, and by extension, the associated angular rate of change, is a major factor that determines the up and down "flapping" response of the liquid jet.

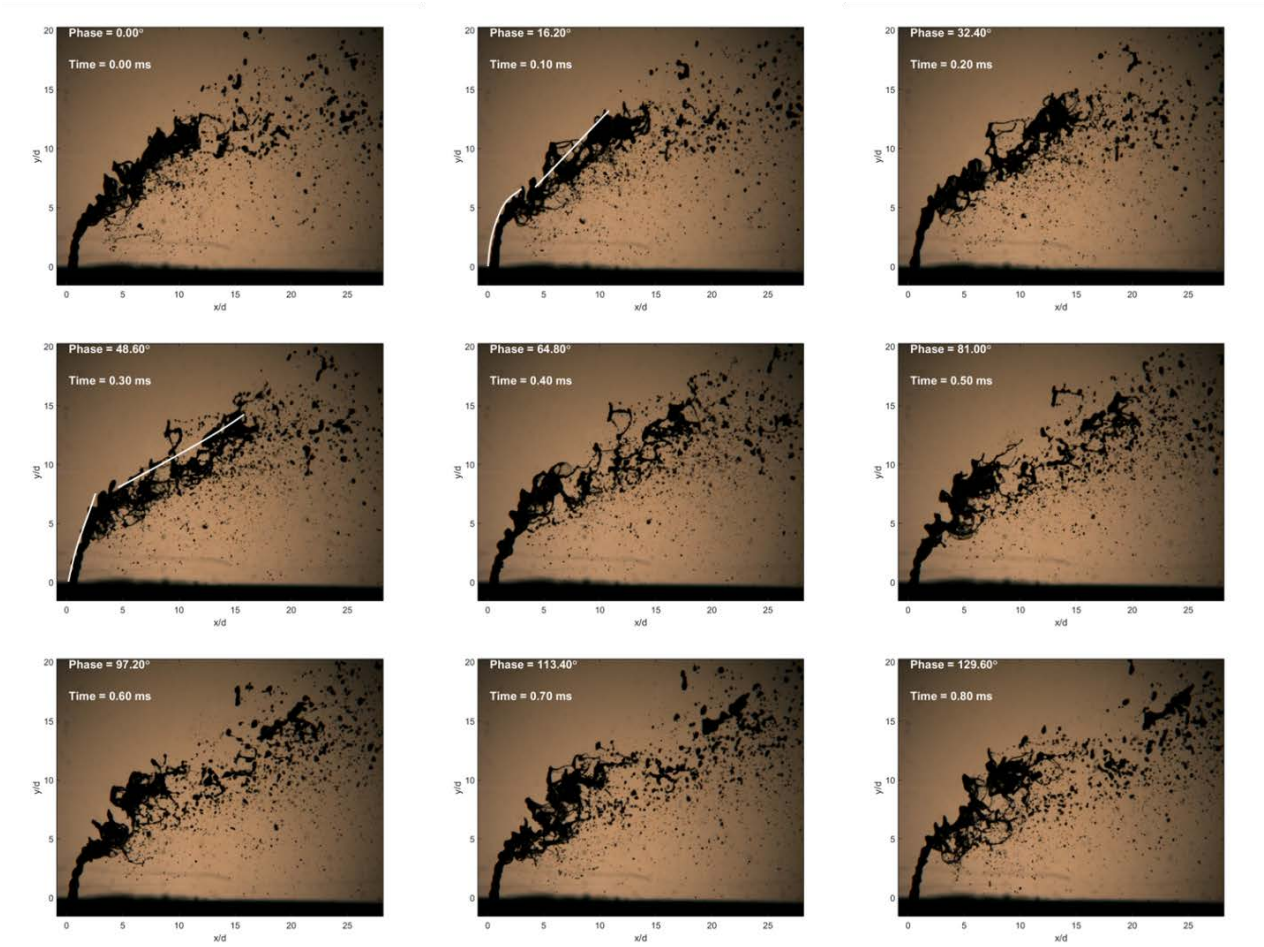

Figure 37. Instantaneous spray images in f=450Hz crossflow within 0.8 ms : Test condition - P=2.04 atm We=18 q=18 MDL=10%

Figure 38 shows that the trend is applicable across a range of Weber number, momentum flux ratio and modulation levels.

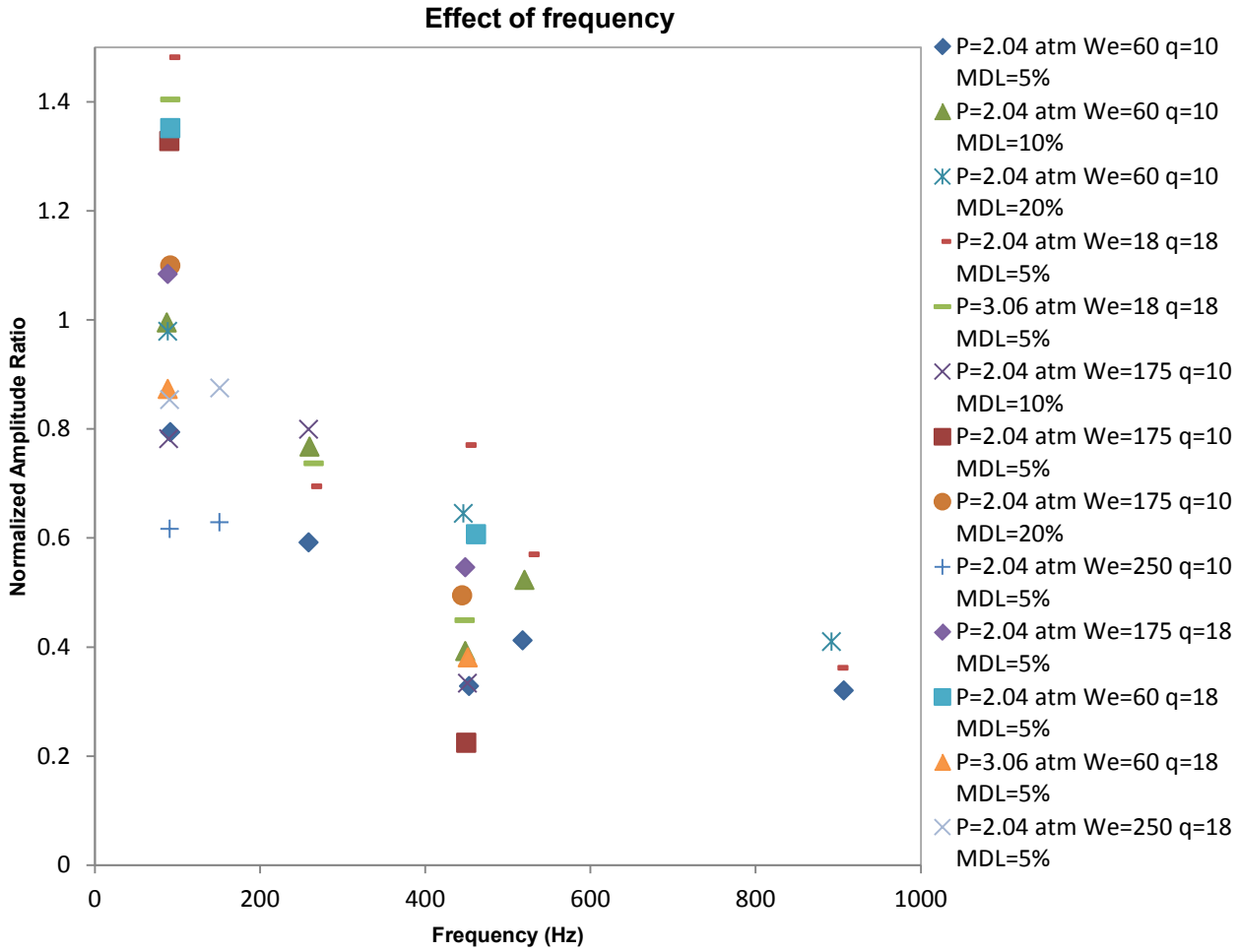

Figure 38. Normalized Amplitude Ratio plotted against modulation frequency for a range of Weber number, momentum flux ratio, static pressure, and modulation level

With an increase in Weber number, the composition of the liquid jet structure in the near-field changes. While the existence of the liquid column, with bag-like structures breaking away near the column breakup point, is observed in lower Weber number case of We=18, the column intensely gets stripped off droplets in the higher Weber number case of We=175. The larger

droplets and the liquid column preserve the injection momentum for a longer time compared to the smaller droplets generated in the shear breakup. This is because the smaller droplets owing to their lower inertia get entrained by the crossflow due to enhanced momentum transfer. It can therefore be expected that the lower Weber number cases will have higher response to the modulating crossflow compared to higher Weber number cases with respect to near-field penetration. The results in this study however do not provide conclusive evidence for this effect although the trend is observed in f=90 Hz cases and further study may be necessary to better characterize the effect of Weber number.

3.2.2.3 Effect of momentum flux ratio

A liquid jet emanating from the nozzle inherently tries to follow a straight path. In the presence of a crossflow, the aerodynamic drag force bends the jet in the crossflow direction and the bend is characterized by the momentum flux ratio. During the course of a period of oscillation of the crossflow velocity, the liquid jet momentarily attains a point with maximum momentum flux ratio in that period. In the near-field region, the jet retains most of its injection momentum and thus has a more stable phase at the time when the crossflow velocity reaches a minimum, and momentum flux ratio reaches a maximum, in the period. This expected behavior is evidenced by comparing the observed momentum flux ratio from the images and the expected momentum flux ratio computed from velocity measurement as shown in Figure 39. The green circles represent the points where the liquid jet remains in the high momentum flux ratio region rather than respond immediately to the change in phase of the velocity. These spikes could explain the increased amplitude of the response signal, and thus the amplitude gains higher than unity for the test cases at low frequency of f=90 Hz. It is to be noted, however, that the degree of synchronization between the pressure signal acquisition and image acquisition is uncertain in

these cases and knowledge of time lag between the two signals could be used in the future to accurately observe the phase difference in response of the jet.

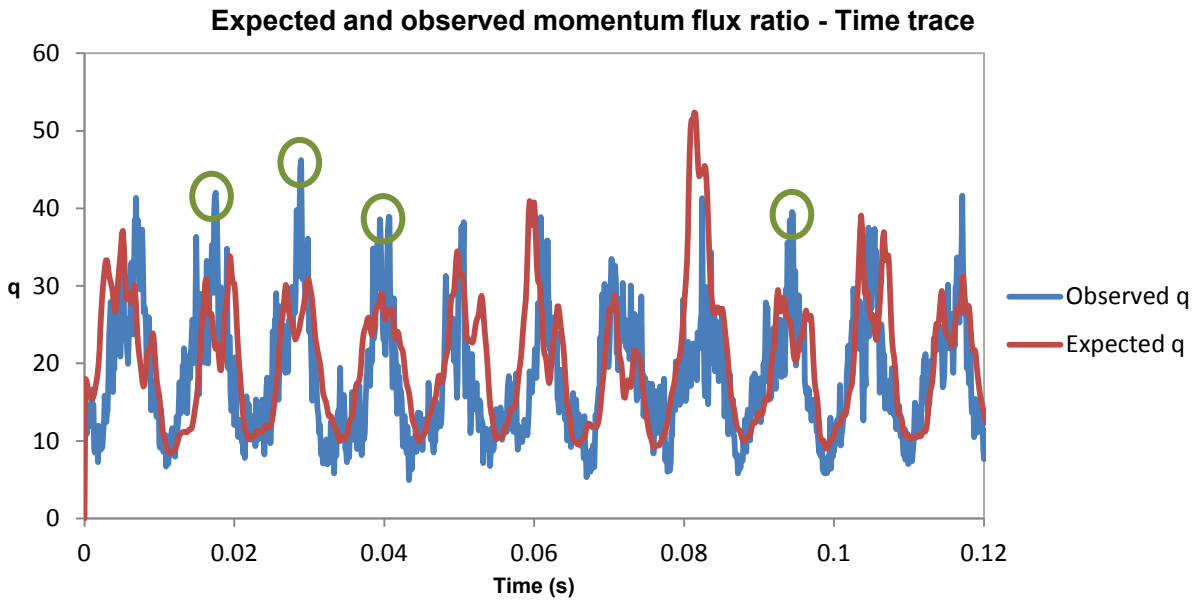

Figure 39. Comparison of momentum flux ratio observed from images and calculated from pressure data: Case - P=2.04 atm We=60 q=18 f=90 Hz MDL=10%

A comparison is then made by studying the jet response in cases with the same crossflow conditions but different momentum flux ratio. Figure 40 shows the case of *We*=60 and crossflow static pressure of 2.04 atm modulated at 90 Hz and 450 Hz, both at the same modulation level of 10% at different momentum flux ratio. It is seen that the normalized amplitude ratio of the observed to expected momentum flux ratio fluctuation remain around the same level in each case. Noting that the range of momentum flux is small, the behavior suggests that the amount of fluctuation in the liquid jet changes proportionally with the expected change. Consequently, it would mean that the response of the liquid jet is affected by other crossflow conditions more than the momentum flux ratio for the same jet breakup mechanism.

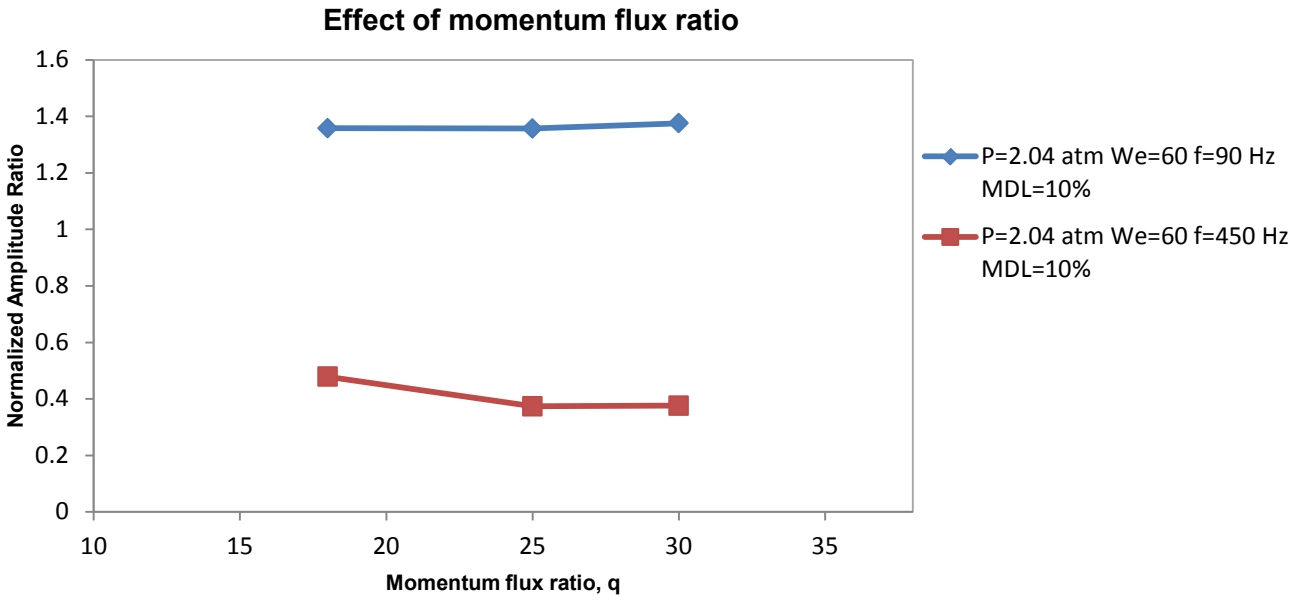

Figure 40. Effect of change in momentum flux ratio on liquid jet response to crossflow modulation

3.2.2.4 Effect of modulation level

The effect of the crossflow modulation level is then analyzed by considering test cases with the same crossflow conditions and momentum flux ratio but with different modulation levels at the modulation frequencies. Figure 41 shows the variation in the power fraction obtained at the modulating frequency from the spectrum of momentum flux ratio extracted from the images. It can be seen that as the modulation level is increased, the spectral power fraction displays a positive correspondence. Since the spectral power fraction is proportional to the square of the normalized amplitude, it can be surmised that the amplitude of momentum flux ratio fluctuation increases with an increase in modulation level.

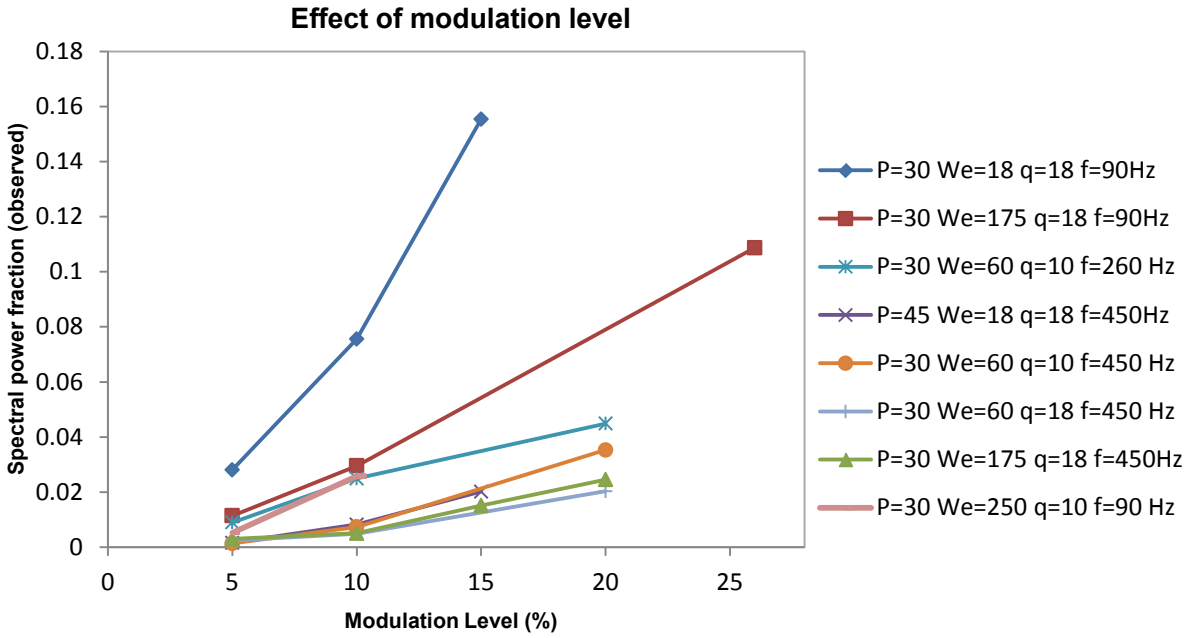

Figure 41. Plot of spectral power fraction from the observed momentum flux ratio spectrum against modulation level

Figure 42 shows the trend of normalized amplitude ratio for the same conditions plotted in Figure 41. Although it is seen that the amplitude of the momentum flux ratio increases monotonously with modulation level, the normalized amplitude ratio does not reflect the same trend. There is a weak increase in the normalized amplitude ratio at 20% modulation level in some of the cases but a dominant trend cannot be discerned. The values predominantly fall in a narrow band of each other for different modulation levels with the same crossflow conditions and momentum flux ratio. This phenomenon is related to the fact that even as the amplitude of momentum flux ratio fluctuation increases in the observed images, the increase is in proportion to the increase in expected momentum flux ratio amplitude. This strengthens the suggestion that in the range of momentum flux ratio and modulation levels under study, the liquid jet response in the near-field is primarily a function of the crossflow modulation frequency.

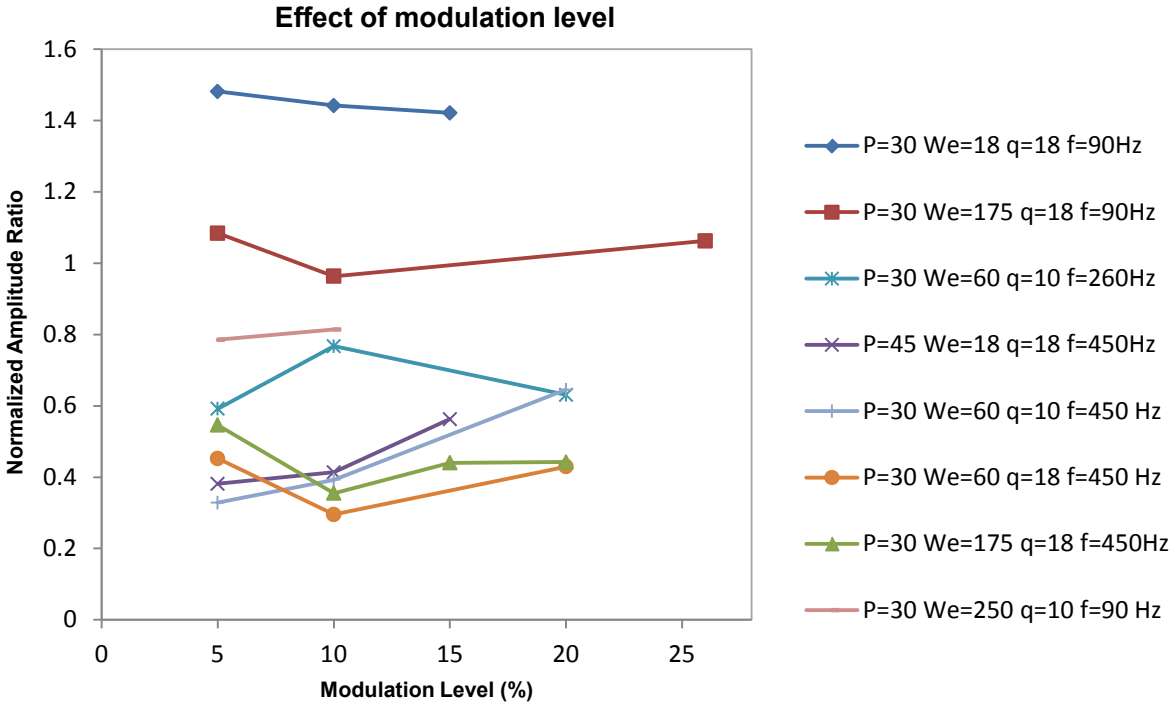

Figure 42. Effect of modulation level - Plot of Normalized Amplitude Ratio against modulation level

4 Liquid Spray Far-Field Analysis

The far-field of the liquid jet in crossflow is the region where the large droplets and ligaments from the column breakup region are further broken down into smaller droplets. In this study, the far-field region is defined to be the region at 50 jet diameters downstream from the liquid injection location (x/d=50). The liquid jet upon breakup consists of a mix of larger droplets near the top of the spray and smaller droplets near the bottom of the spray in the column and bag breakup regimes. The composition of the spray varies in the shear breakup regime where the droplets are smaller after primary breakup. Thus the penetration of the liquid spray in the far-field is different from the near-field penetration, being dependent upon various factors, and by extension, the response to modulation would also depend on multiple variables.

4.1 Far-field Analysis using High-Speed Camera Images

The far-field region is first studied using high-speed camera images to identify the mode of spray response in oscillating crossflows. The test conditions correspond to the conditions mentioned in Table 3.

Figure 43 and Figure 44 show the liquid jet in a crossflow with Weber number 18 and static pressure 2.04 atm, and at momentum flux ratio of 18 in two different modulation frequencies of f=90 Hz and f=450 Hz. The blue line represents the x/d=50 location. Noting that the phase in all the figures is relative to the first frame, it can be seen that the spray displays noticeable up and down flapping motion in the f=90 Hz case. The flapping motion is hard to discern in the f=450 Hz case.

Figure 45 and Figure 46 show the liquid jet behavior in a crossflow with higher static pressure of 3.06 atm and Weber number 60 at two different modulation frequencies of f=90 Hz and f=260 Hz. The same observation is made in the lower frequency case of f=90 Hz, with the liquid spray showing evident up and down motion at x/d=50. In the f=260 Hz case, there is still a noticeable movement of the spray but it appears dampened compared to the lower frequency case. Having made this qualitative observation, the next step describes the attempt to quantitatively compare the spray response in various conditions.

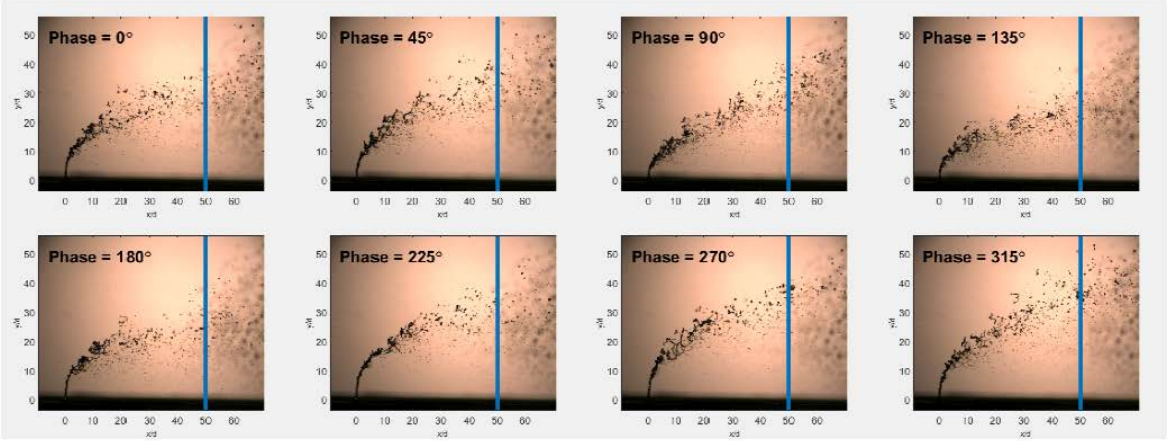

Figure 43. Far-field images at different phases: Case - P=2.04 atm We=18 q=18 f=90 Hz MDL=10%

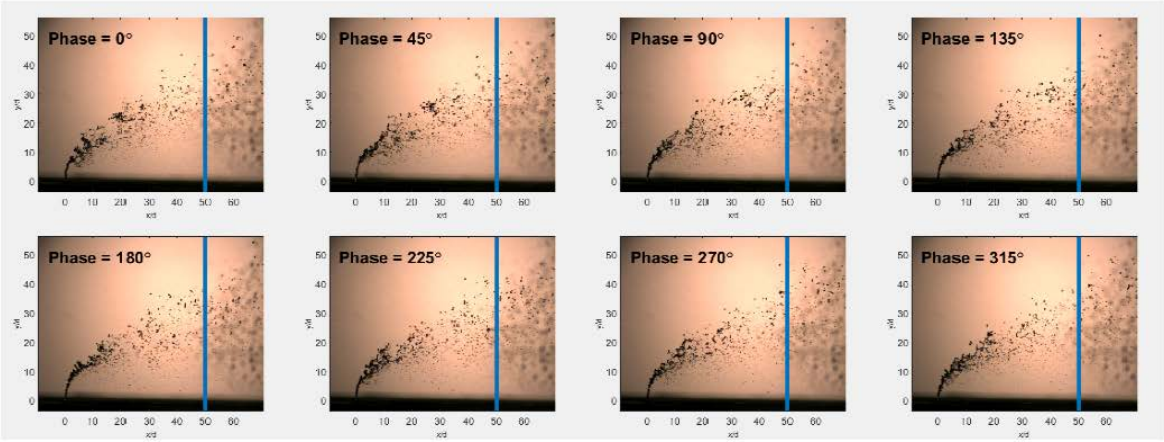

Figure 44. Far-field images at different phases: Case - P=2.04 atm We=18 q=18 f=450 Hz MDL=10%

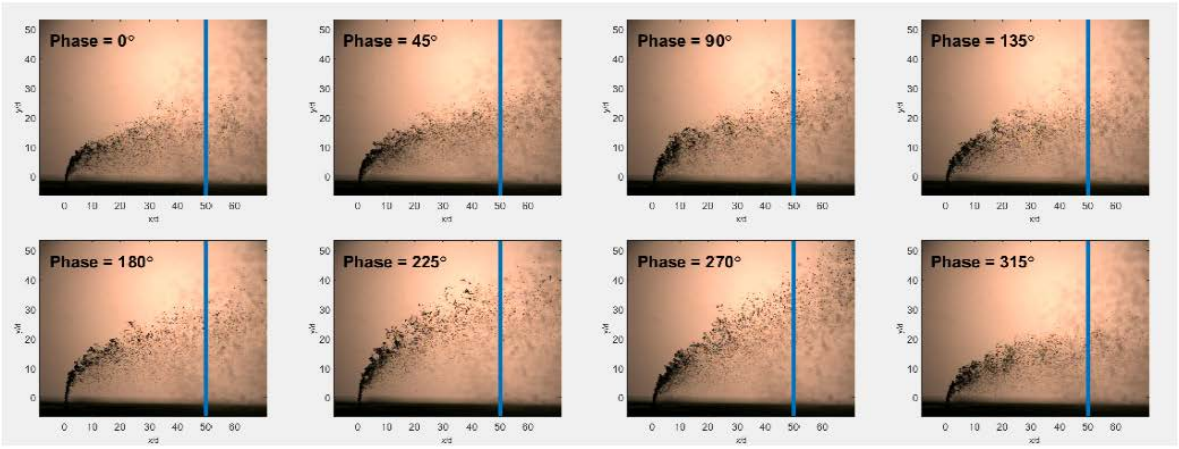

Figure 45. Far-field images at different phases: Case - P=3.06 atm We=60 q=18 f=90 Hz MDL=10%

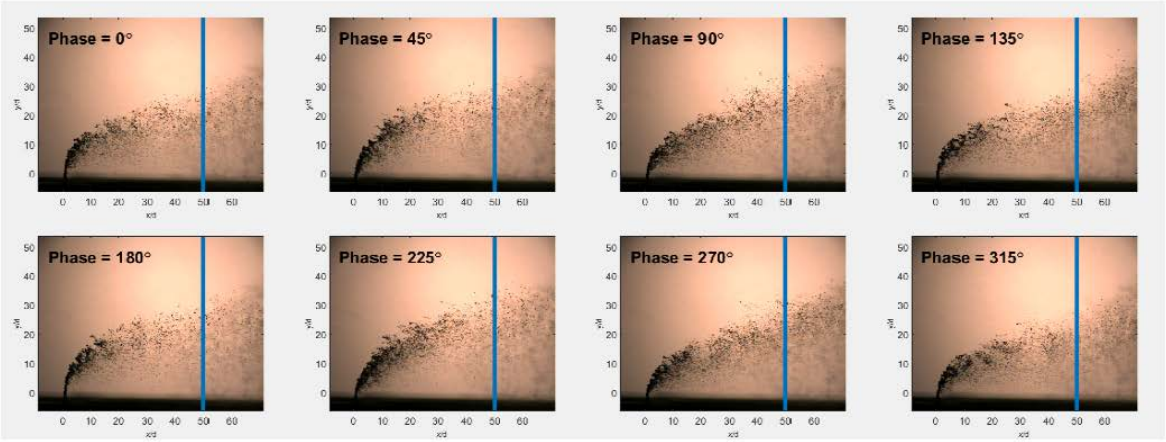

Figure 46. Far-field images at different phases: Case - P=3.06 atm We=60 q=18 f=260 Hz MDL=10%

4.1.1 Analysis Procedure and Results

The analysis is performed by measuring the change in intensity produced by the movement of droplets in each frame. In order to do this, the first step is to prepare a background from which the change in intensity can be measured. The average of all the frames acquired for the test condition can be used as the background, which means that any change in intensity from the background is a measure of deviation from the mean. Figure 47 shows an example of averaged image created for the condition corresponding to the images in Figure 45 [P=3.06 atm We=60 q=18 f=90 Hz MDL=10%].

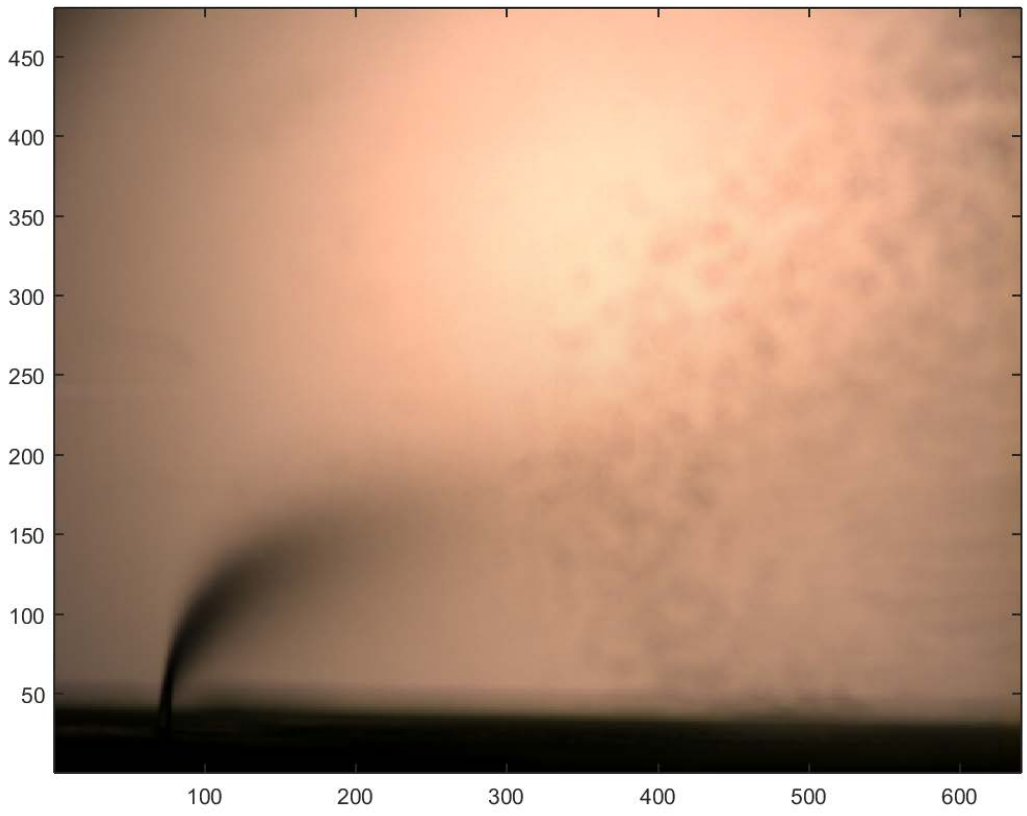

Figure 47. Sample averaged image: Case - P=3.06 atm We=60 q=18 f=90 Hz MDL=10%

The next step is to divide the image height into ten equal sized bins. Since the image height is 480 pixels, each bin has a height of 48 pixels. The width of the bin is chosen such that the bin would encompass five pixels upstream and five pixels downstream of the *x/d*=50 location. Thus each bin is 11 pixels wide. Figure 48 is a sample instantaneous frame showing the bin locations.

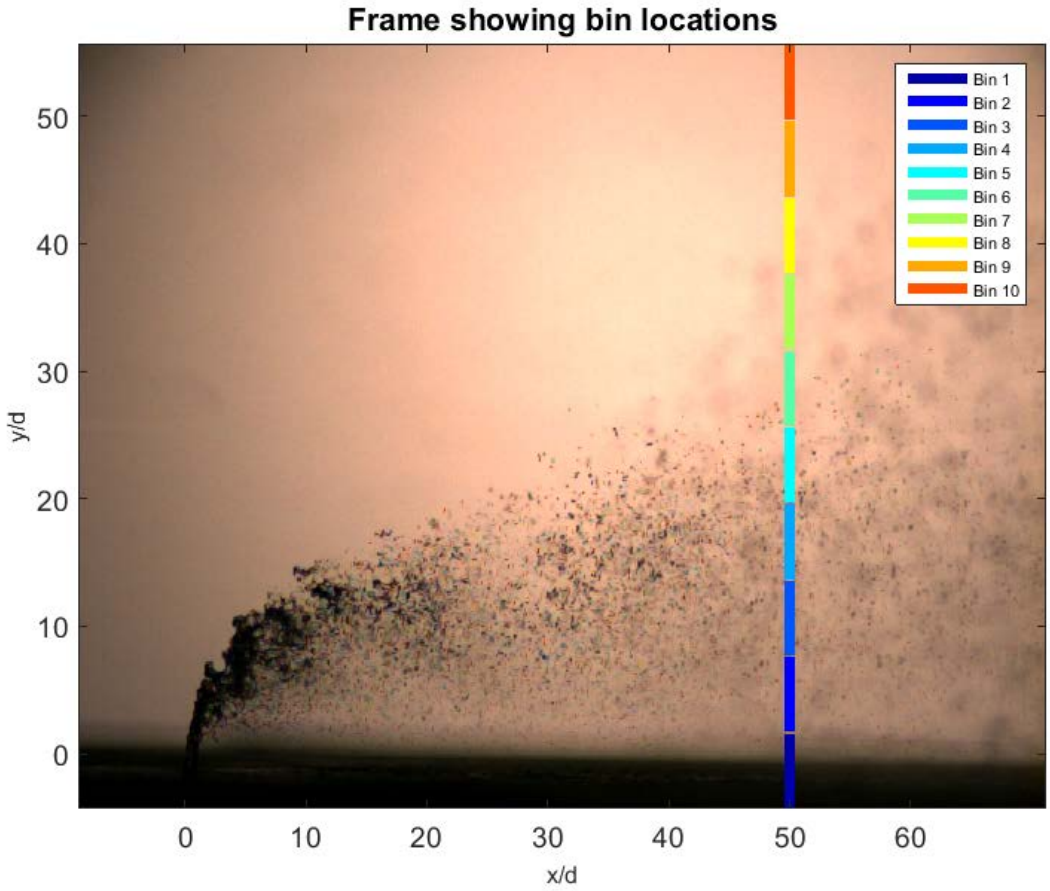

Figure 48. Bin locations

In each instantaneous image, the intensities of the pixels deviating from the averaged image lying within each bin are added to the respective "BinSum". The threshold for considering a pixel intensity to have deviated from the averaged image is calculated by first subtracting intensities of each column from the corresponding column in averaged image, then calculating the mode near zero of the difference, and then adding one standard deviation of the difference to the mode. This process ensures the robustness of the code in identifying droplets. Figure 49 shows a sample time trace of the sum of intensities in a bin. The sum of intensities will hereafter be referred to as Bin Sum. Thus, the Bin Sum can be approximated as the "area flow of droplets" in the bins in the 2-D plane.

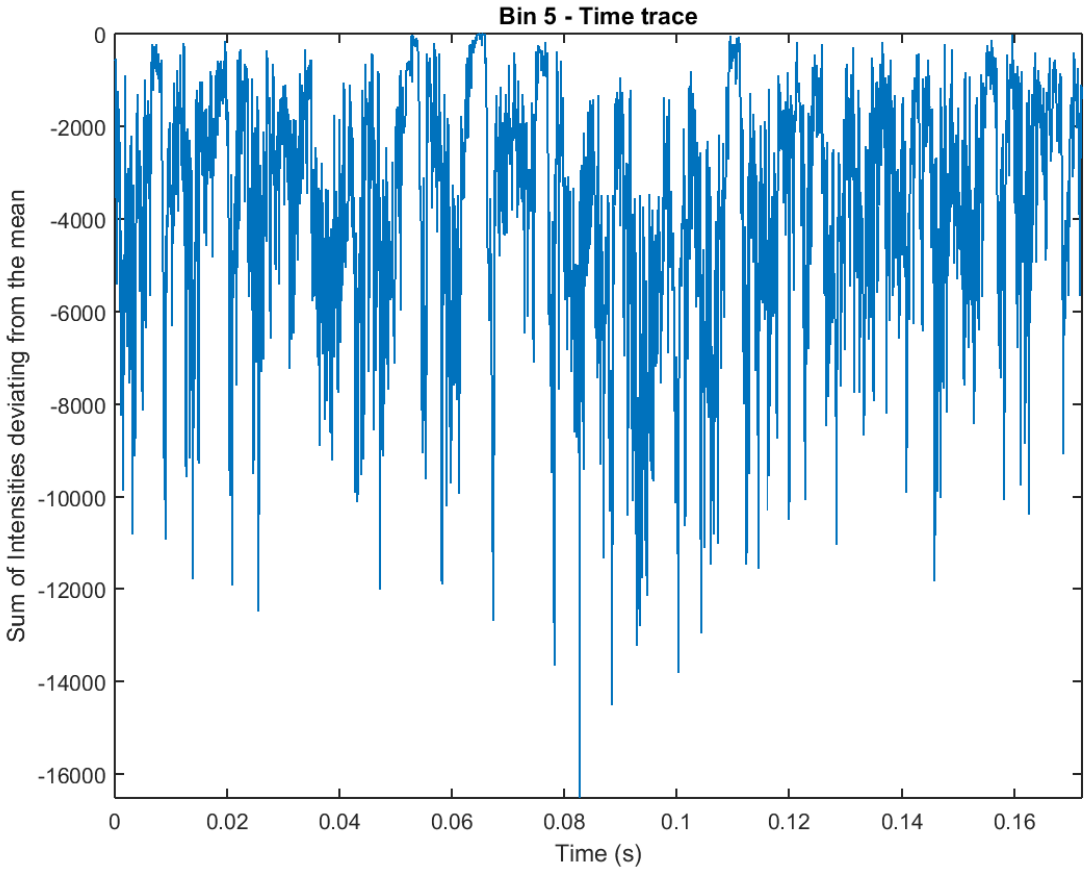

Figure 49. Sample of time trace of sum of intensities obtained from a bin: Case - P=3.06 atm We=60 q=18 f=90 Hz MDL=10%

The Bin Sums in all the bins normalized by the respective mean of Bin Sums is shown in Figure 50. It can be seen that the signal is periodic; therefore an FFT is performed on the Bin Sums to identify the frequency components. Figure 51 shows the amplitude spectrum of the ten bins and it is observed that, in this case, all the bins show a response at the forcing frequency of the crossflow of 90 Hz. However, this response has different amplitudes in the different bins due to the variance in the number and size of droplets passing through each bin.

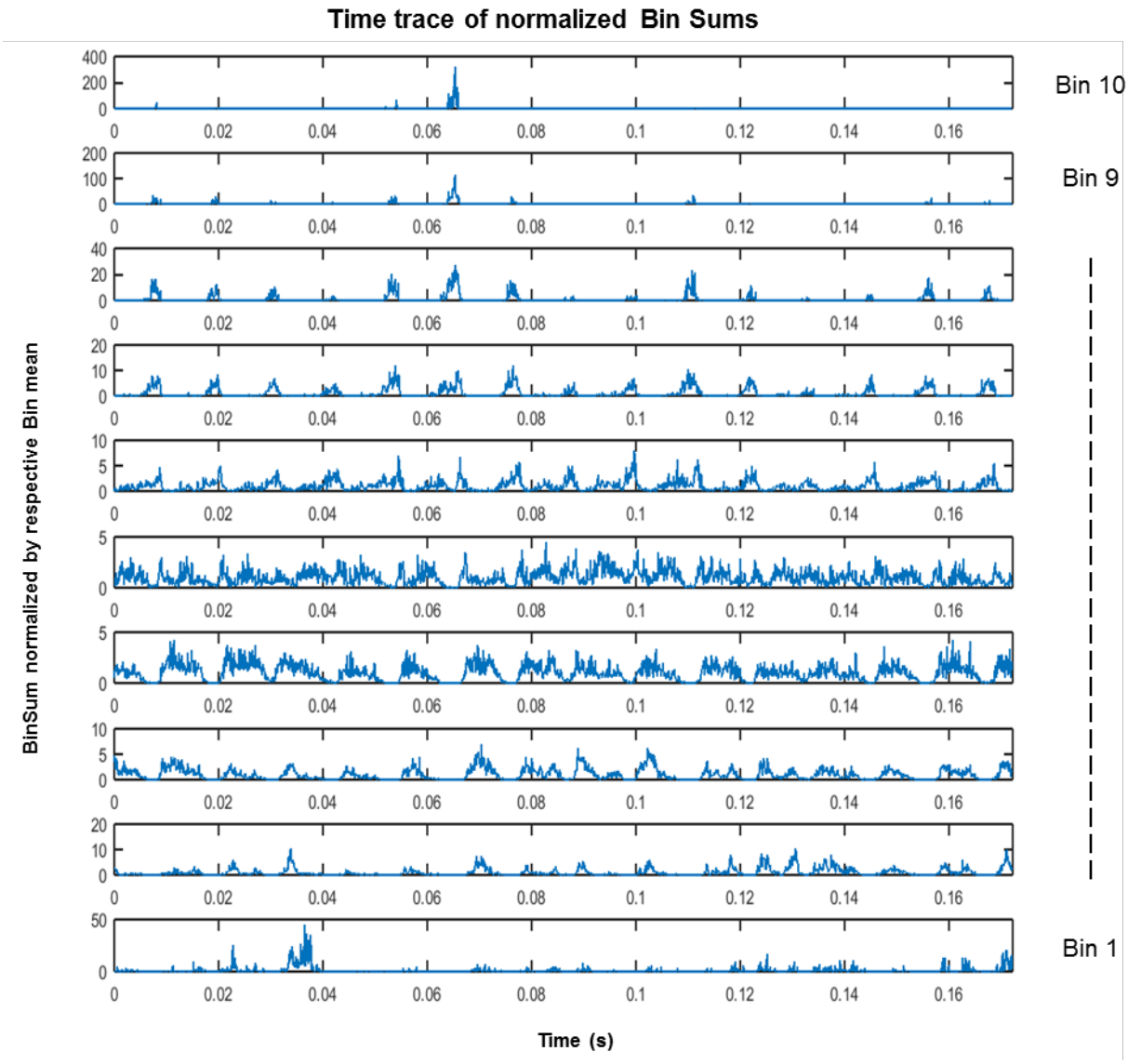

Figure 50. Time trace of Bin Sums normalized by respective mean of Bin Sum: Case - P=3.06 atm We=60 q=18 f=90 Hz MDL=10%

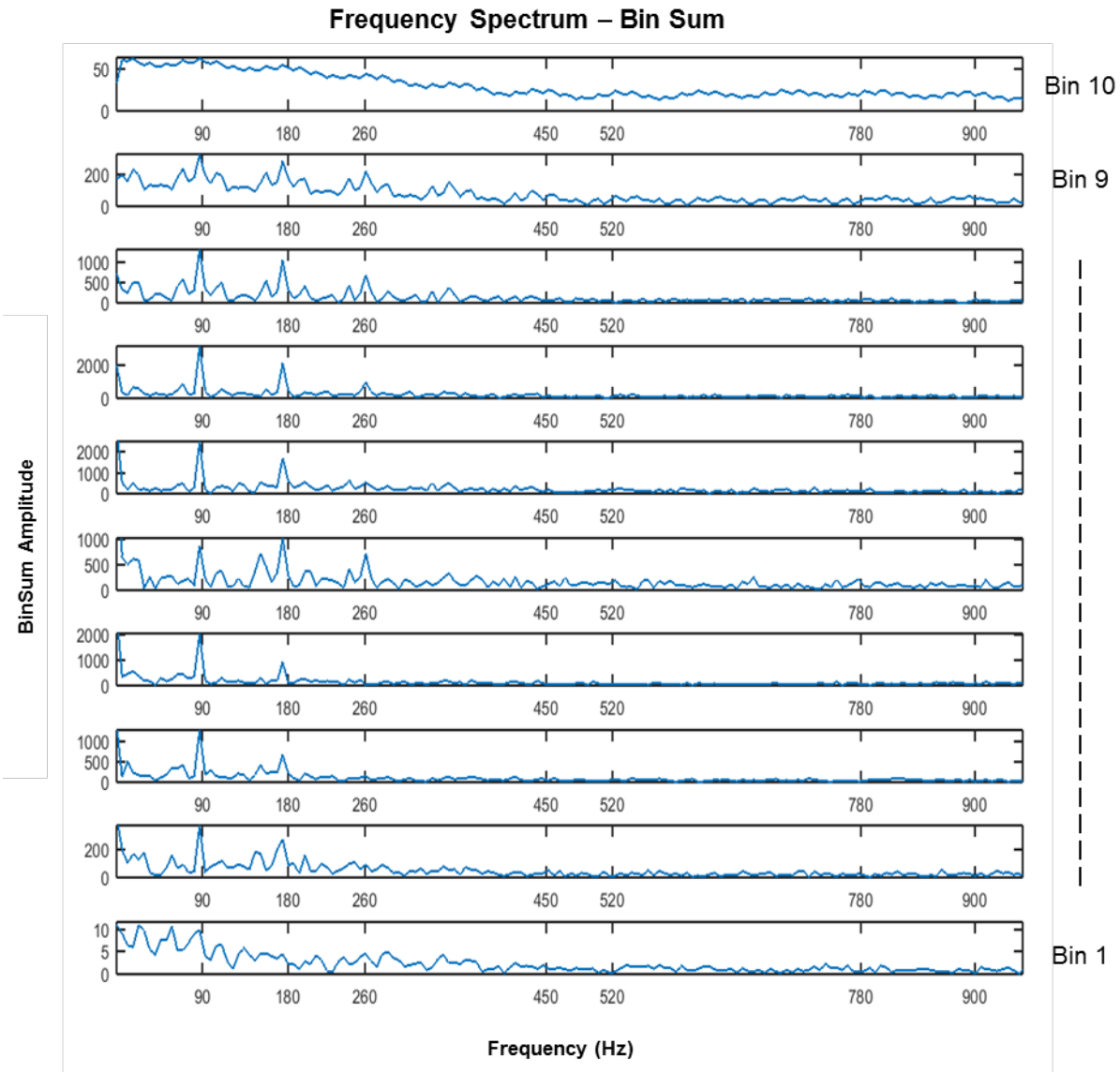

Figure 51. FFT of Bin Sums: Case - P=3.06 atm We=60 q=18 f=90 Hz MDL=10%

Even though the frequency spectrum provides the response at specific frequencies, information about the difference in phase between the various bin signals will be vital in understanding the jet behavior. Therefore, the Bin Sums were normalized to zero mean and unit variance and then filtered at the peak modulation frequency (in a 60 Hz bandwidth) using a second-order Butterworth filter as shown in Figure 52. It is clear from observation that while some Bins are in

phase with each other, others are out of phase. Also, some Bins have a very weak value which signifies that the spray droplets pass through those bins minimally.

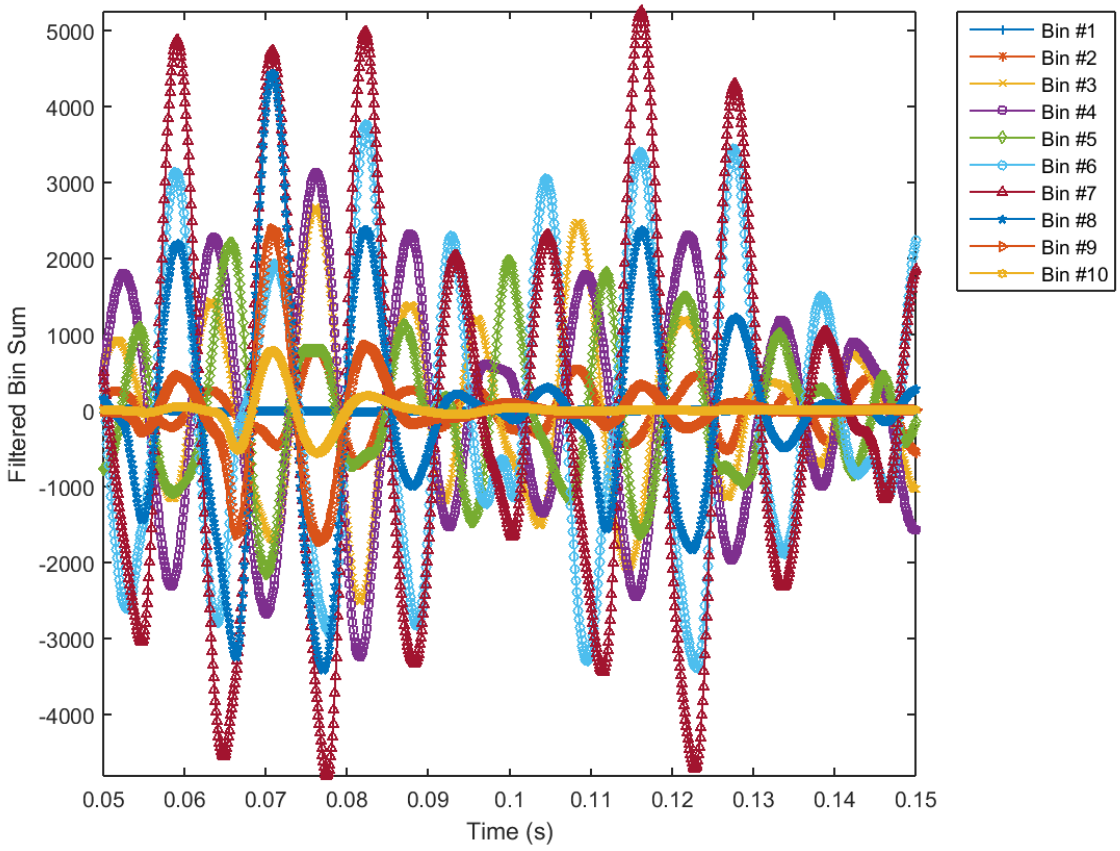

Figure 52. Normalized Bin Sums filtered at the peak modulation frequency: Case - P=3.06 atm We=60 q=18 f=90 Hz MDL=10%

In order to filter out the bins which receive the lowest fraction of the spray and might throw errors while calculating phase differences, the Bin Sums, which are vectors of temporal information, were summed up to obtain the sum of Bin Sums in the ten bins. These ten values were again summed up to obtain the total sum of intensities in all the pixels covered by the bins, which was then used to calculate the fraction of the sum of intensities in each bin. Since the sum

of intensities is considered to be proportional to the area of the droplets passing through the pixels, the fractions correspond to the fraction of droplets passing through the bins.

Figure 53 shows a bar diagram of the fraction of sum of Bin Sums in each bin. It is seen that the fractions are highest in the middle bins and taper off towards the top and bottom bins. Comparing the f=90 Hz cases, and f=450 Hz and f=260 Hz cases, the lower frequency cases have well distributed fractions while the higher frequency cases tend to have high fractions concentrated in the middle bins. The bins with fractions less than 1% were then removed from the calculations to get the phase difference between the bins.

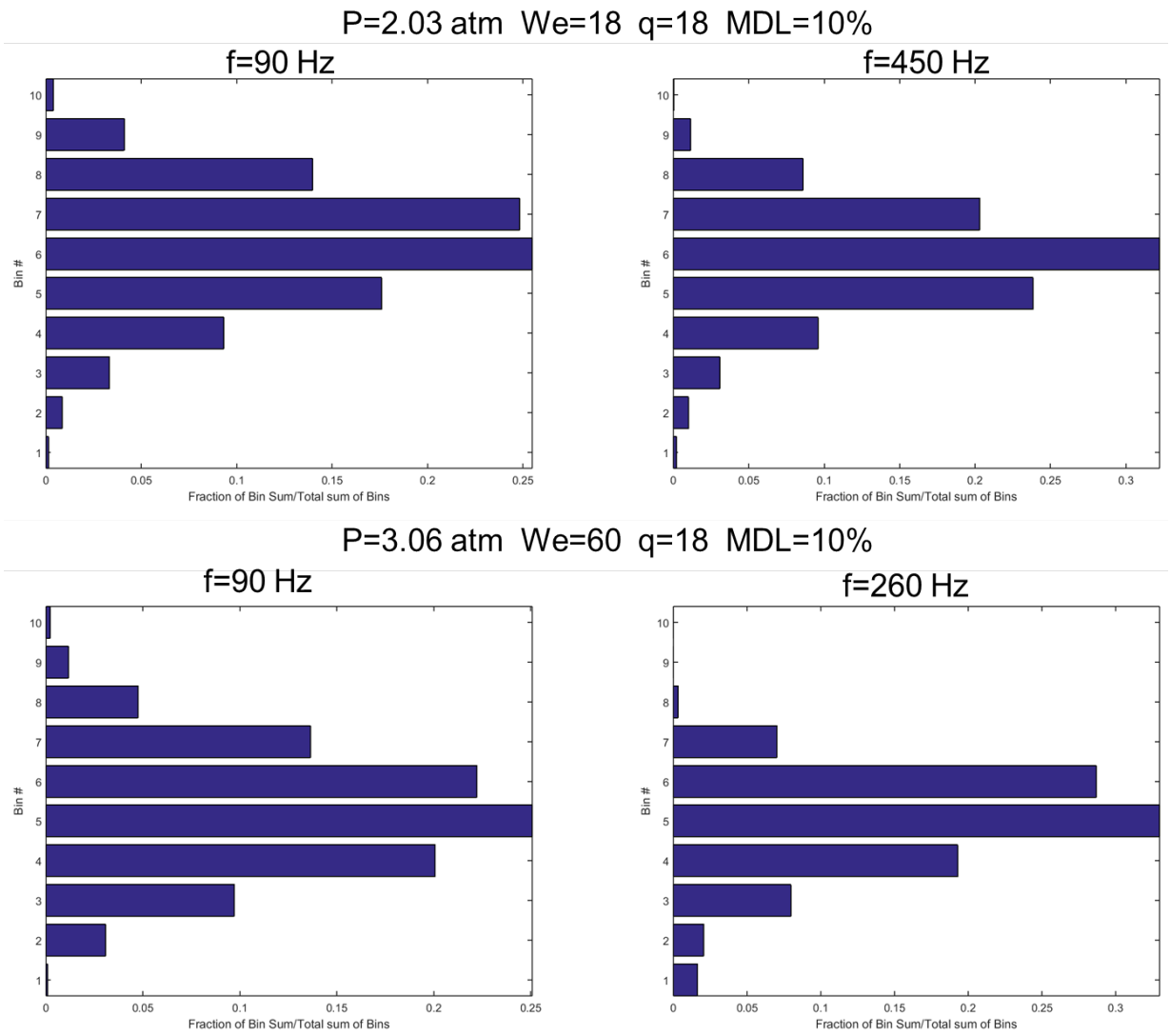

Figure 53. Comparison of normalized Bin Sum fractions: (Top, Left) P=2.03 atm We=18 q=18 f=90 Hz MDL=10%; (Top, Right) P=2.03 atm We=18 q=18 f=450 Hz; MDL=10% (Bottom, Left) P=3.06 atm We=60 q=18 f=90 Hz MDL=10%; (Bottom, Right) P=3.06 atm We=60 q=18 f=260 Hz MDL=10%

Figure 54 shows a comparison of phase plot for four different test conditions. The angle between the bins is calculated by the cross-correlation method from the filtered normalized Bin Sums. For example, the phase lag between two signals A and B can be found by cross-correlating the two signals, and finding the time when the cross-correlation attains its maximum. This gives the time

lag between the two signals, which can then be converted to phase lag since the frequency is known. The phase plot radius vector is proportional to the amplitude from the filtered normalized Bin Sums signals. It is observed that in the lower frequency cases of f=90 Hz, the phase difference between the bins is almost 180 degrees. Also, the amplitudes are comparable in magnitude except for the end bins. This signifies that when the spray is concentrated at one of the end bins, the BinSum value reaches a local maximum while the opposite end bin has a reduction in BinSum, and therefore is out of phase. However, in the higher frequency cases of f=450 Hz and f=260 Hz, the amplitudes have a sharp drop from the bins where most of the spray is concentrated. Further, the bins are closer to each other in phase compared to the lower frequency cases.

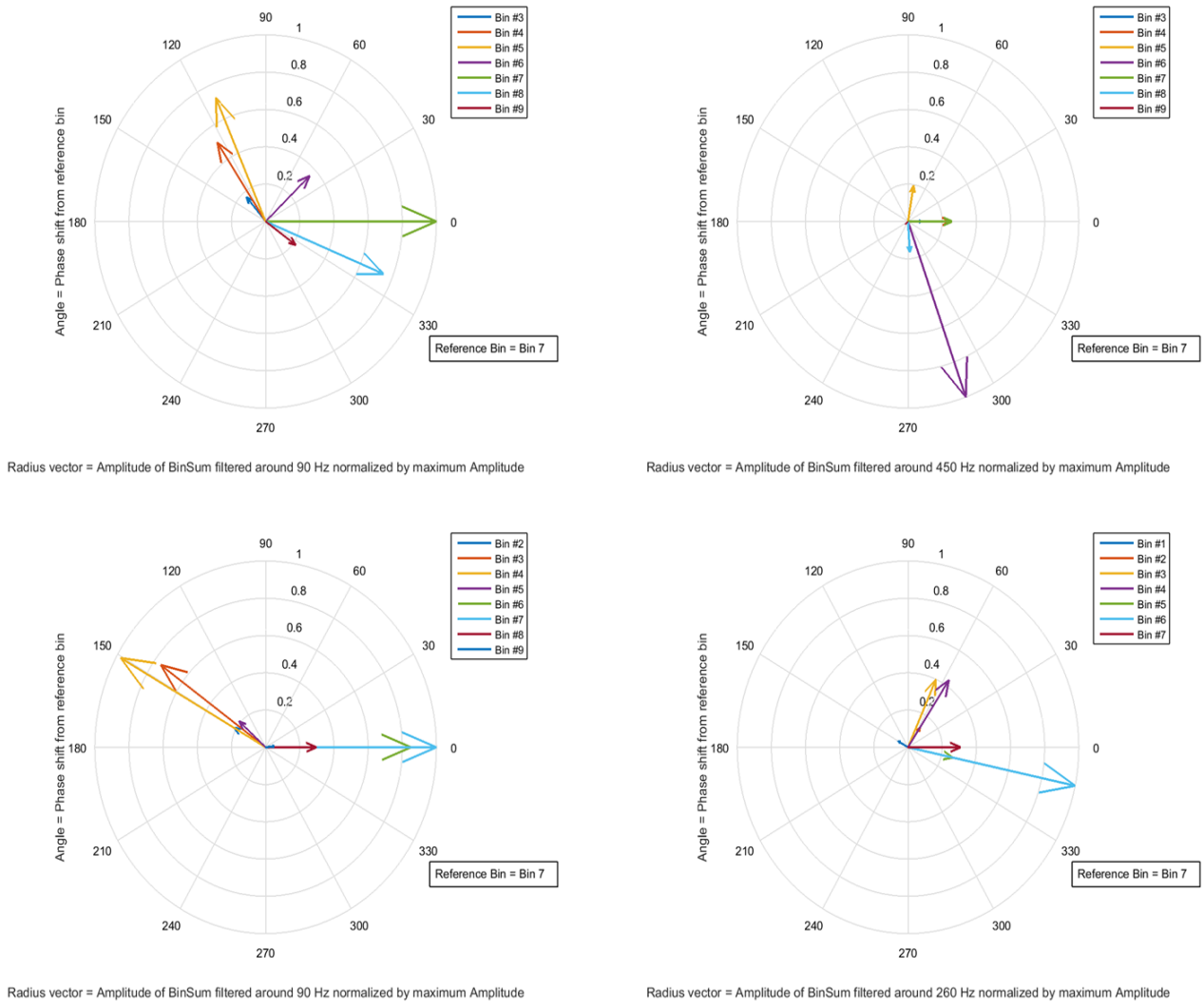

Figure 54. Comparison of phase plots of four test conditions: (Top, Left) P=2.03 atm We=18 q=18 f=90 Hz MDL=10%; (Top, Right) P=2.03 atm We=18 q=18 f=450 Hz; MDL=10% (Bottom, Left) P=3.06 atm We=60 q=18 f=90 Hz MDL=10%; (Bottom, Right) P=3.06 atm We=60 q=18 f=260 Hz MDL=10%

In order to quantify the degree of spread of the phase angles, the circular variance of the phase angles was calculated with the amplitudes acting as the weights using Circular Statistics Toolbox in MATLAB [24]. The circular variance is indicative of how much the data is spread out in an

angular sense, with higher spread tending towards circular variance of 1 and lower spread towards circular variance of 0.

If the $i=1,2,\ldots,n$ phase angles, each represented by θ_i, are converted to vectors r_i, as shown in Eq. (14),

$$\vec{r}_i = \begin{bmatrix} \cos\theta_i \\ \sin\theta_i \end{bmatrix} \quad (14)$$

then the magnitude of the mean resultant of the vectors, R, is given by Eq. (15),

$$R = \left\| \frac{1}{n} \sum_{i=1}^{n} \vec{r}_i \right\| \quad (15)$$

and the circular variance, S, is given by Eq. (16).

$$S = 1 - R \quad (16)$$

For example, if two vectors point in the same direction, they will have circular variance of 0 while vectors pointing in opposite directions will have circular variance of 1.

To get a measure of the shape of the spray spread, the data in bar plots such as in Figure 53 were converted into distributions. This is possible since the data is a set of fractions totaling one and can be converted to an equivalent frequency of samples in each bin. Then, the standard deviation of the distribution was calculated to quantify the spread of the spray among the bins.

The far-field analysis is summarized in the form of a flowchart in Figure 55.

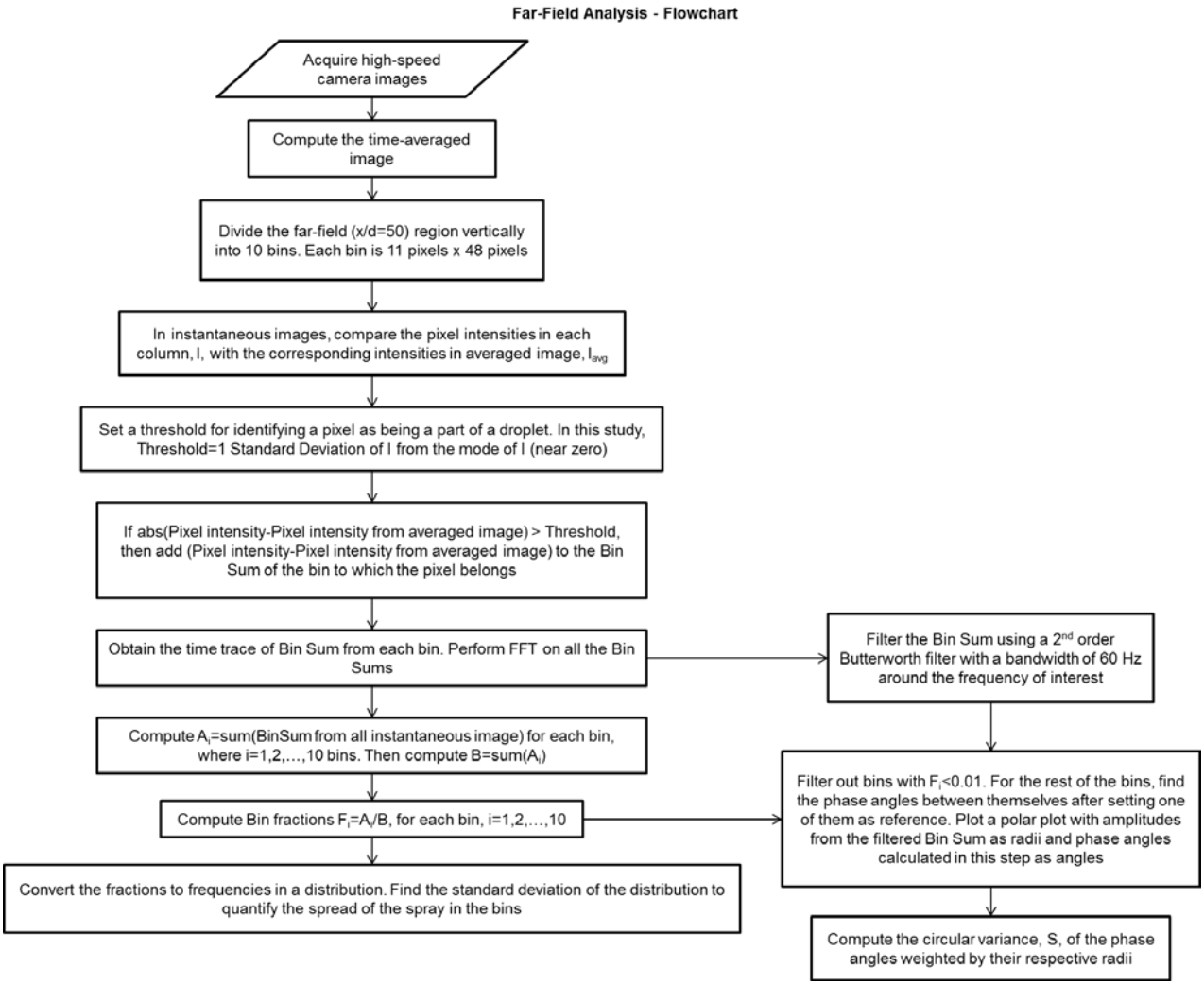

Figure 55. Flowchart summarizing far-field analysis

Figure 56 and Figure 57 are plots showing the effect of frequency on the standard deviation of the normalized Bin Sum fractions and the circular variance of the phase differences between Bins respectively. Both the plots show a general trend of a decrease in their respective values with increasing frequency. A decrease in the standard deviation suggests that the distribution from which it was calculated gets more concentrated around the mean value. In this case, it translates to mean that the spray is restricted to fewer bins around the mean position. Also, it is seen that with an increase in modulation level, the standard deviation increases substantially at

the lower frequency of 90 Hz. The circular variance plot has to be viewed in conjunction with the plot on standard deviation of normalized Bin Sum fractions. The reduction in circular variance suggests that the phase difference between the bins is reduced, which is possible when the up and down flapping motion of the spray is curtailed. When the circular variance is closer to unity, it signifies that the bins tend to have a phase difference of 180 degrees, which is possible when the spray flaps between a larger number of bins with the corresponding bins from each end being out of phase with each other. Juxtaposing the two results, it is observed that with an increase in frequency, the standard deviation of the bins is reduced, signifying that the spray gets concentrated around the mean position. At the same time, the circular variance also decreases, lending credence to the argument that the up and down flapping motion of the liquid spray is dampened with increasing frequency.

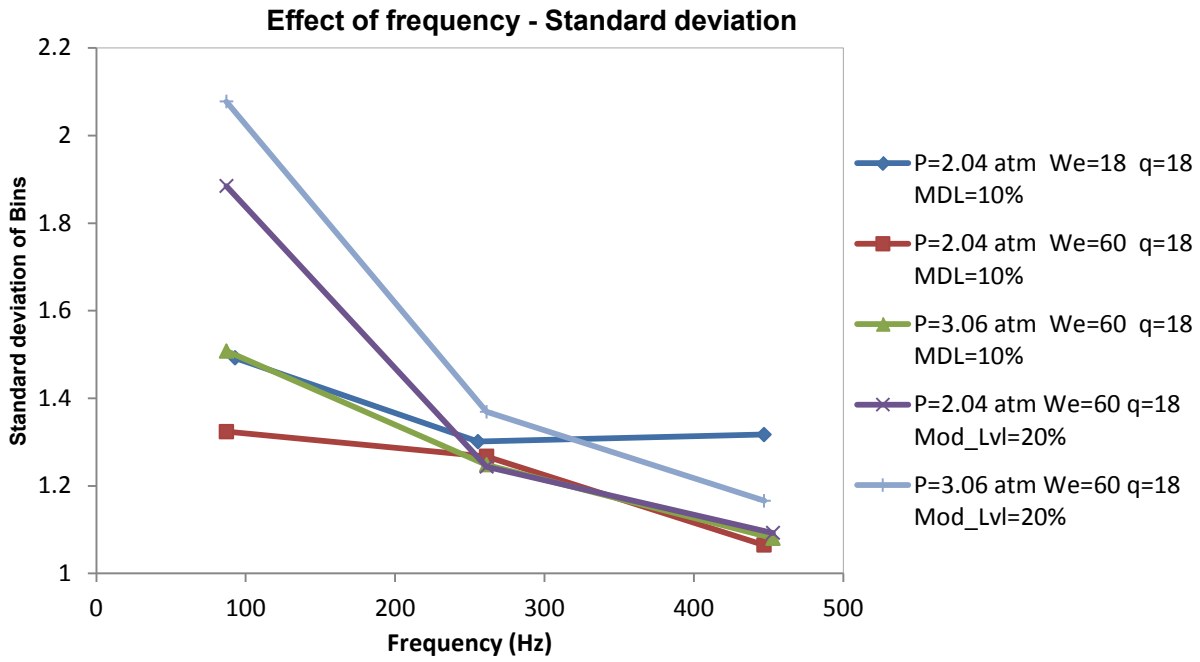

Figure 56. Variation of standard deviation of Bins with modulation frequency

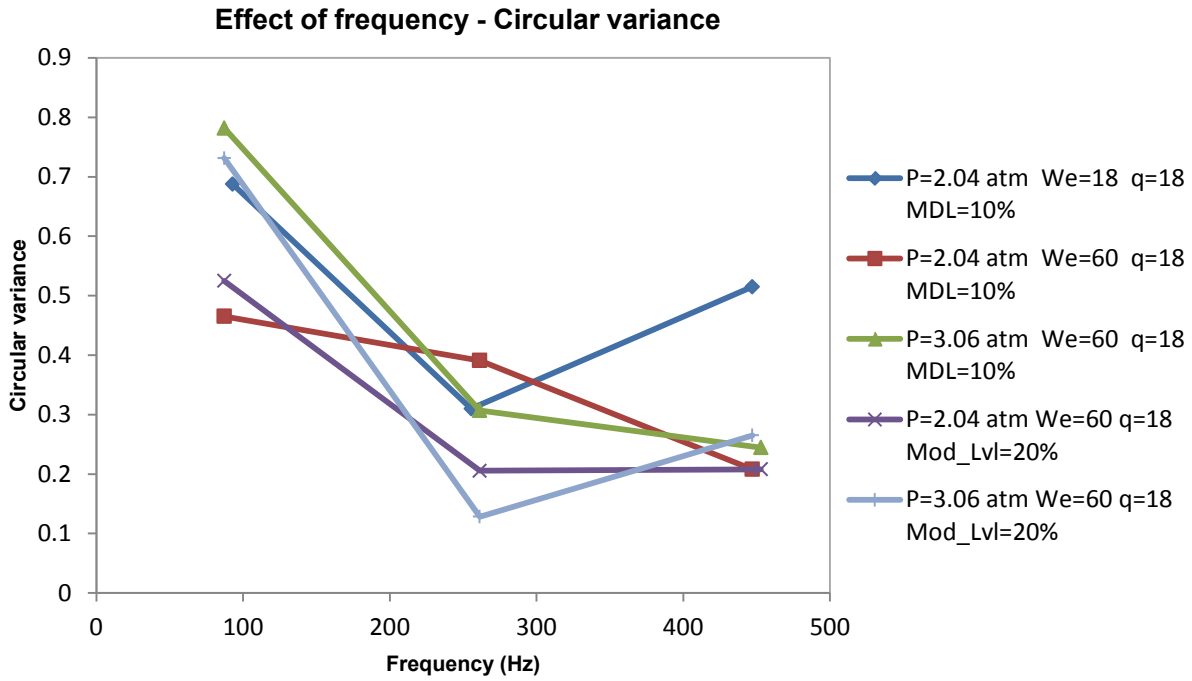

Figure 57. Variation of circular variance of the phase difference between Bins with modulation frequency

Video 5 illustrates the change in Bin Sum values as the liquid spray flaps between the bins. However, it is unfiltered and contains background noise. The Bin Sums are then filtered around the modulating frequency and the animated time series of bar plots is shown in Video 6 and Video 7 for modulating frequencies 90 Hz and 450 Hz respectively.

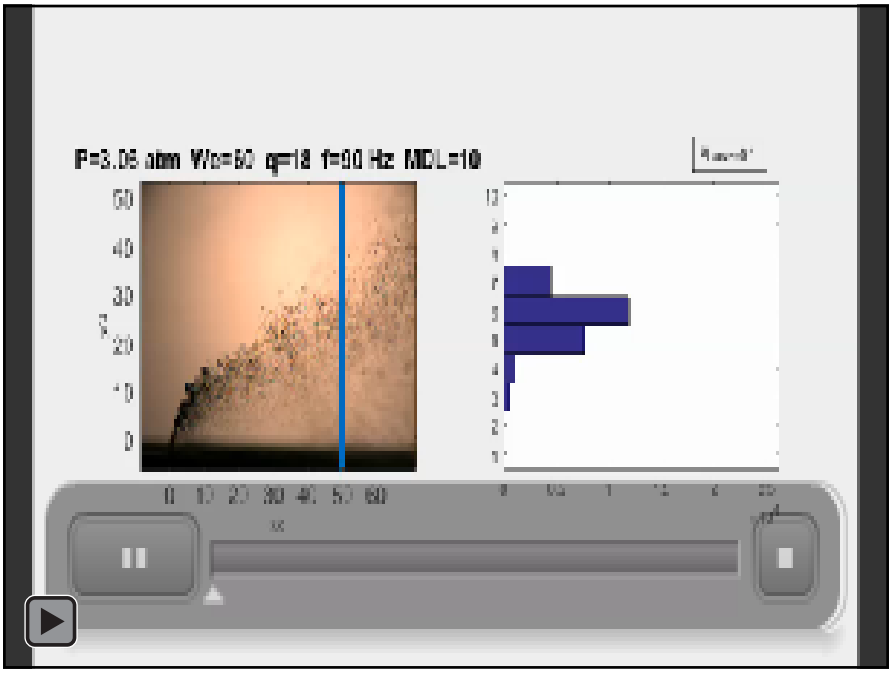

Video 5. Video showing the flapping of the liquid column and the corresponding variations in Bin Sum: Case - P=3.06 atm We=60 q=18 f=90 Hz MDL=10%

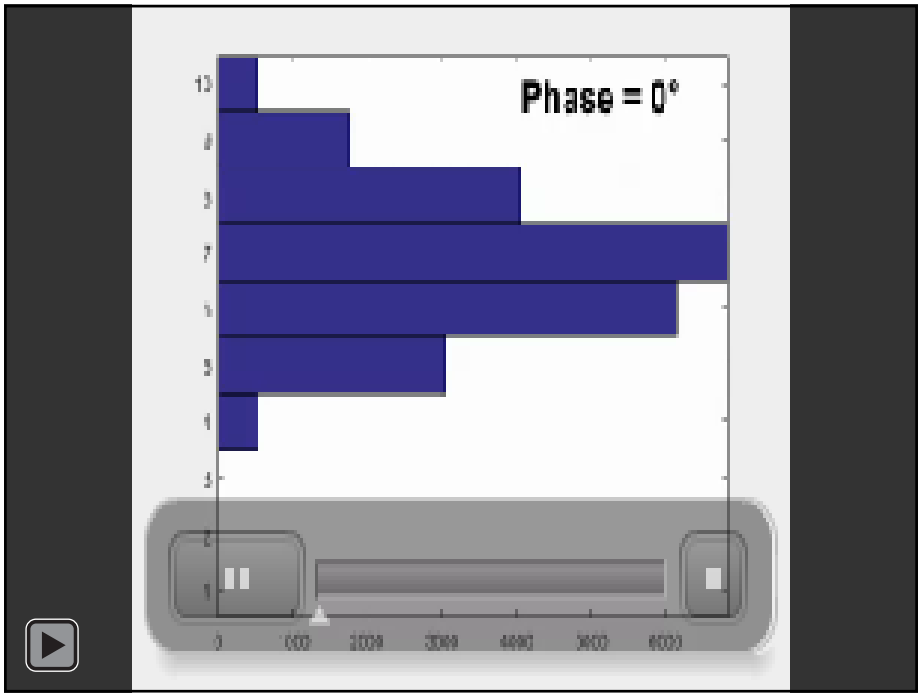

Video 6. Video showing the variation of Bin Sum filtered at modulating frequency: Case - P=3.06 atm We=60 q=18 f=90 Hz MDL=10%

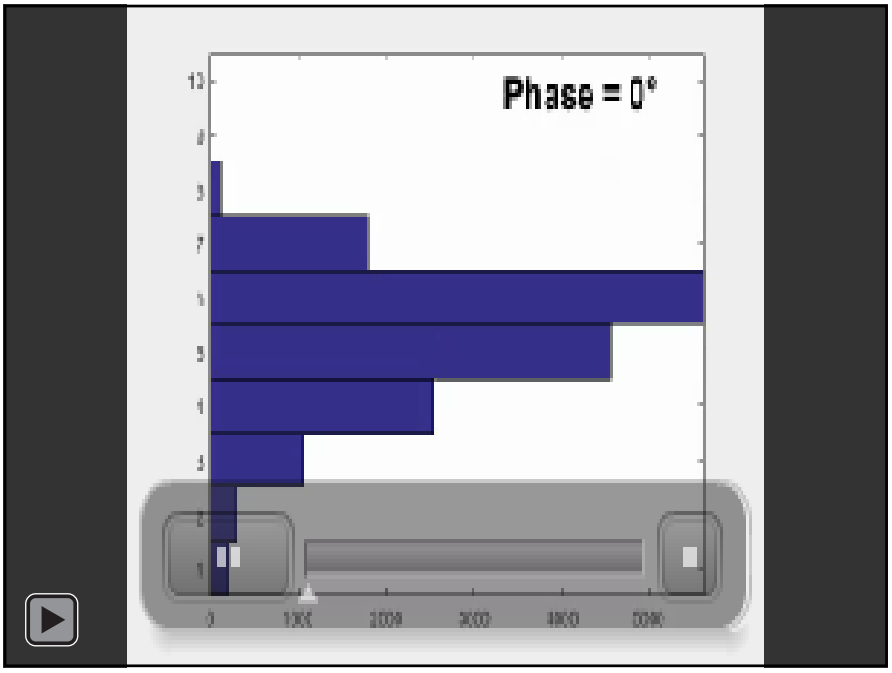

Video 7. Video showing the variation of Bin Sum filtered at modulating frequency: Case - P=3.06 atm We=60 q=18 f=450 Hz MDL=10%

Figure 58 and Figure 59 are snapshots from Video 6 and Video 7 respectively at different phases within a period of modulation of crossflow. It can be observed from the videos and the figures that in the 90 Hz case, the spray flapping is observed in the bar plots between bins 2 and 10. At phase of 0 degrees, the spray passes through bins 4 through 10 and at a phase of 176 degrees (~180 degrees), the opposite end bins from 2 through 5 receive the spray. This behavior is restricted in the higher frequency case of 260 Hz, where most of the spray fluctuates between the central bins 3 through 7.

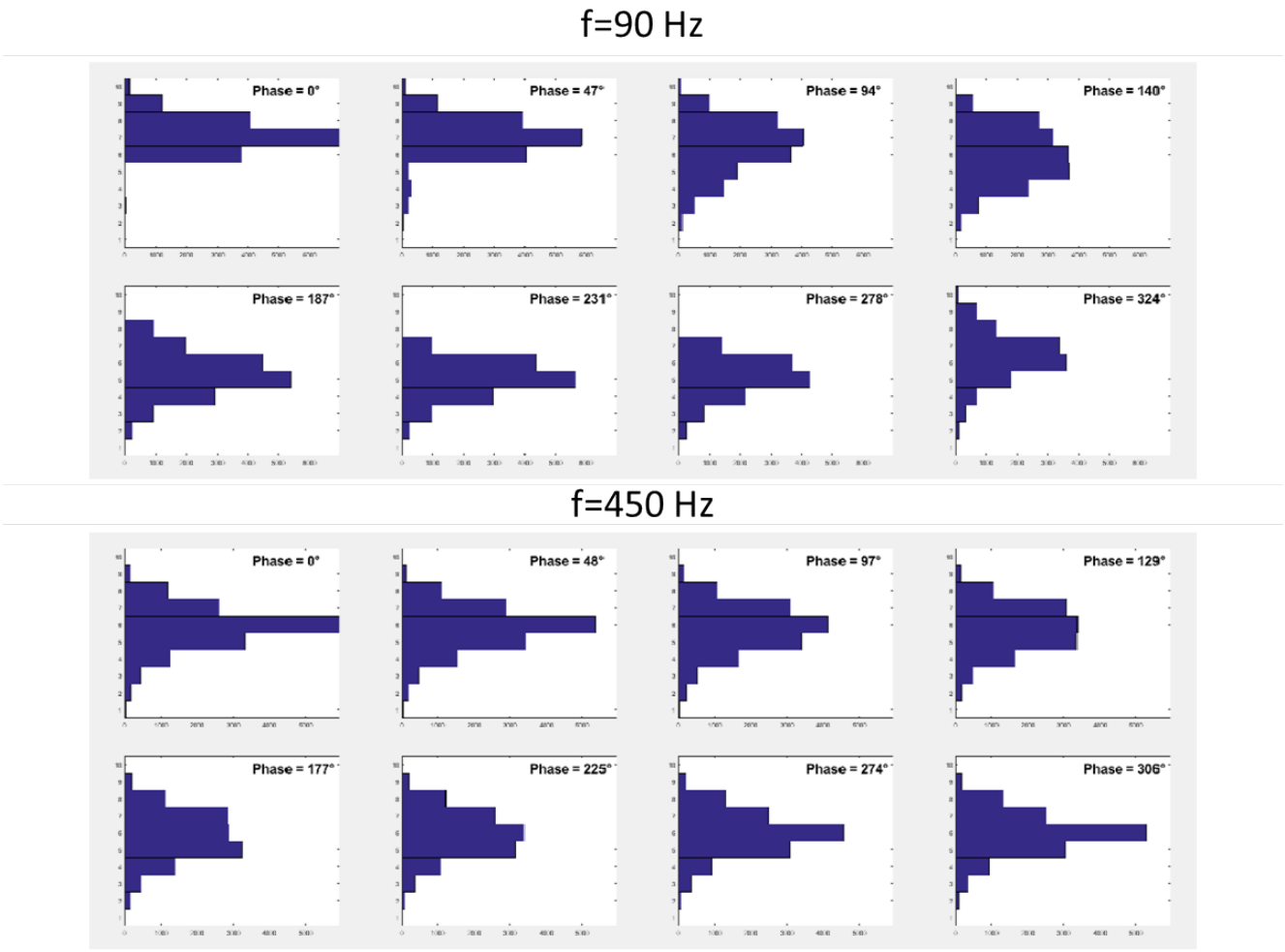

Figure 58. Bar plots of Bin Sums filtered at modulating frequency at different phases for 2 different frequencies: Case - P=2.04 atm We=18 q=18 MDL=10% [x axis: Filtered Bin Sum yaxis: Bin #]

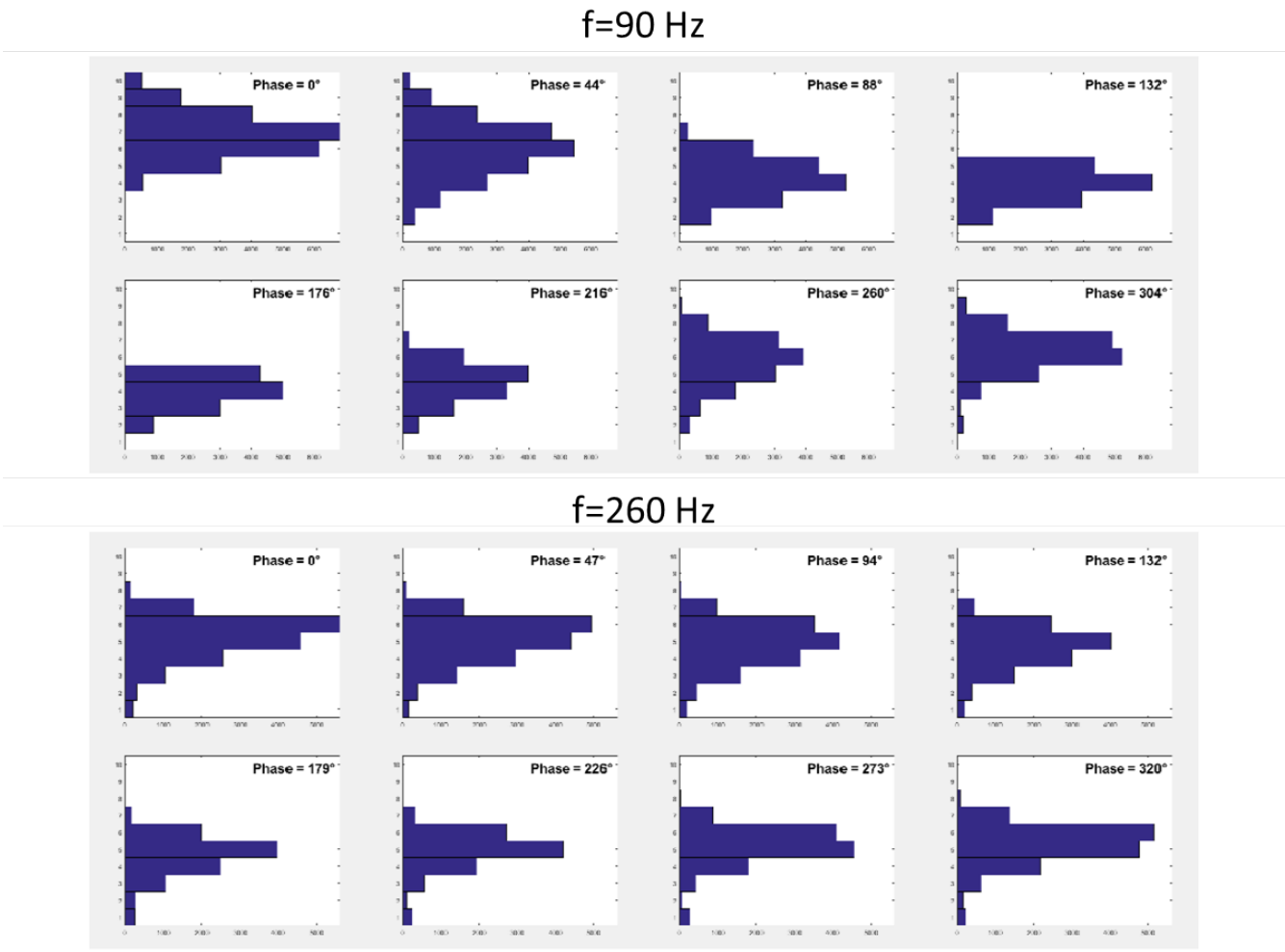

Figure 59. Bar plots of Bin Sums filtered at modulating frequency at different phases for 2 different frequencies: Case - P=3.06 atm We=60 q=18 MDL=10% [x axis: Filtered Bin Sum yaxis: Bin #]

5 Far-Field Analysis using Spray Cross-Section Images

In the discussion in the preceding section, the behavior of the liquid spray at *x/d*=50 was quantified with the help of "bins". While this was useful in analyzing and describing the response, a more quantifiable description of the liquid spray characteristics in the far-field is desirable. The spray cross-section images are acquired to supplement the side-view image analysis. Since the spray is illuminated in this case by a laser, the acquired images are that of Mie-scattering intensity from the spray at *x/d*=50. The Mie scattering intensity in a plane is proportional to the total surface area of the droplets in the plane, and therefore, is dependent on the droplet size distribution [19].

The camera is positioned at an angle of 45 degrees to the cross-section while acquiring the images. In order to convert the images into cross-sectional views, a projective transform is performed on each image by correlating the pixel lengths with actual test-section dimensions. Figure 60 shows an example of the projective transform with an averaged cross-section image. From the transformed images, the center of the intensities (z_{CI},y_{CI}) in the spray region was calculated using Eqs. (17) and (18) (I_i is the intensity of the point (z_i,y_i) where $i \in n$, the pixels in the spray region):

$$z_{CI} = \frac{\sum_{i=1}^{n} I_i z_i}{\sum_{i=1}^{n} I_i} \qquad (17)$$

$$y_{CI} = \frac{\sum_{i=1}^{n} I_i y_i}{\sum_{i=1}^{n} I_i} \qquad (18)$$

After applying a thresholding procedure to filter out the noise as described in Appendix D, the spray's lateral extent is measured to obtain the width and the vertical extent to obtain the height. A sample instantaneous image frame showing the center of intensity, spray's lateral and vertical extents is shown in Figure 61.

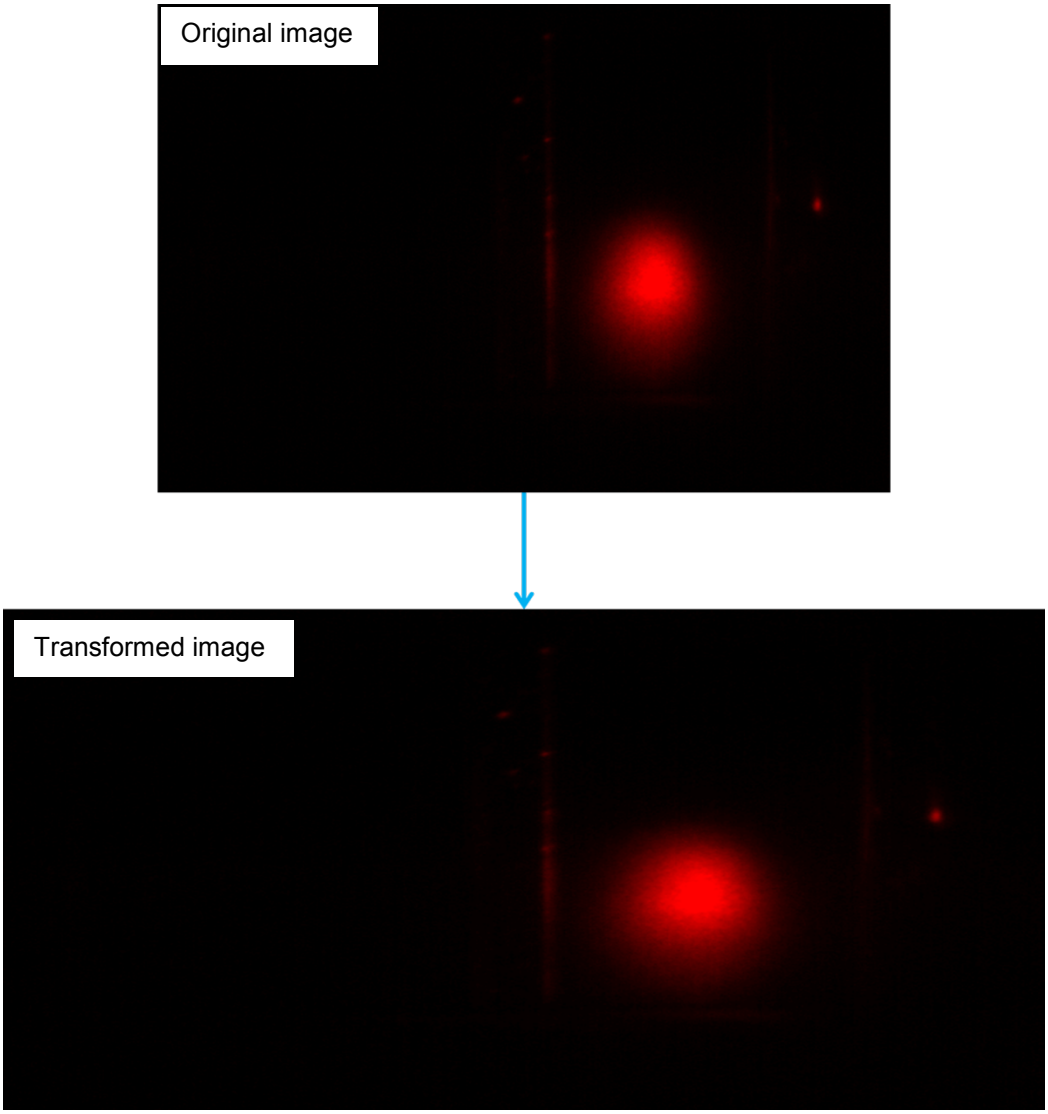

Figure 60. Projective transform: Before (Top) and After (Bottom)

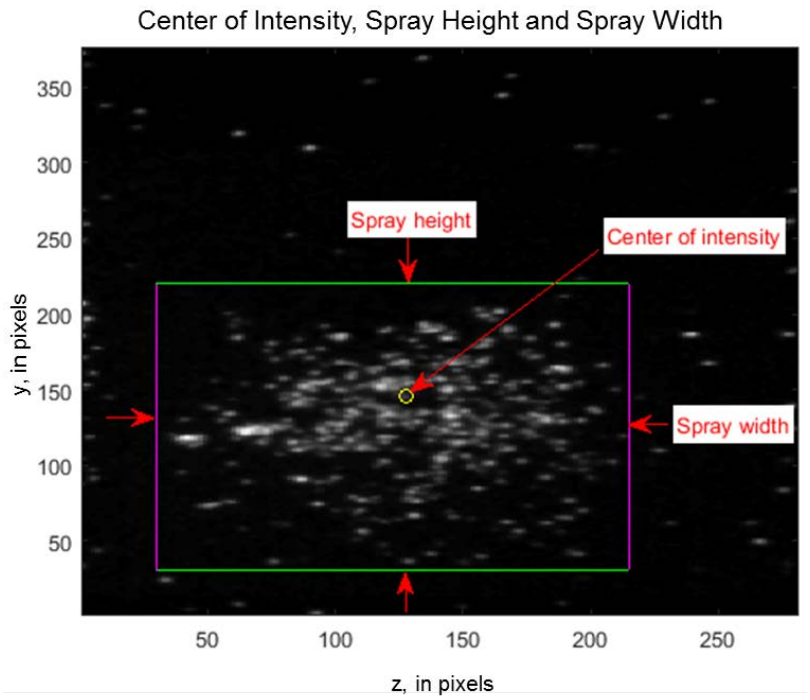

Figure 61. Instantaneous image showing Center of Intensity, Spray Width and Spray Height

5.1 Observations and Discussion

Time-varying signals of the spray's center of intensity, spray height, spray width and the total Mie-scattered intensity from the spray are generated from the instantaneous camera images. Figure 62 through Figure 69 show the time traces and their respective frequency domain spectra of the center of intensity, spray lateral spread, vertical spread and the total sum of intensities in the spray. A periodic variation can be discerned in the center of intensity time trace, but the other time-domain signals have a much lower signal-to-noise ratio. From the frequency spectra, it is observed that all the quantities under consideration have a periodic response at the modulation frequency.

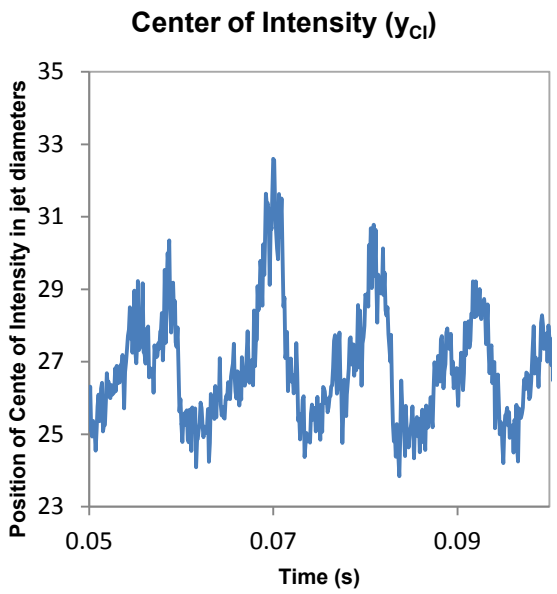

Figure 62. Time trace of Center of Intensity: Case - P=2.04 atm We=60 q=18 f=90 Hz MDL=10%

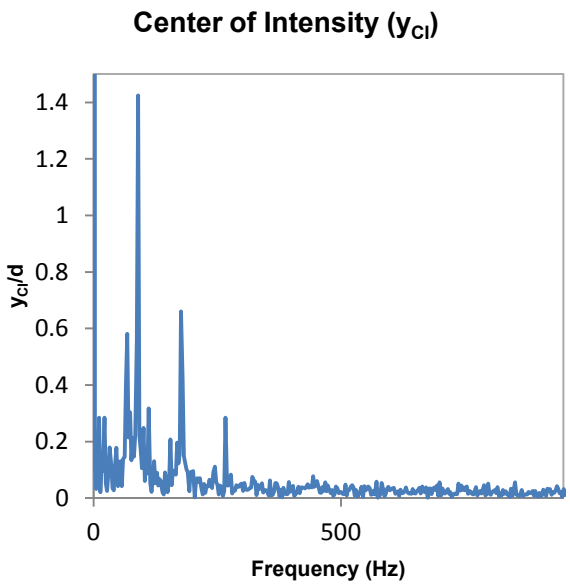

Figure 63. Frequency sprectrum of Center of Intensity: Case - P=2.04 atm We=60 q=18 f=90 Hz MDL=10%

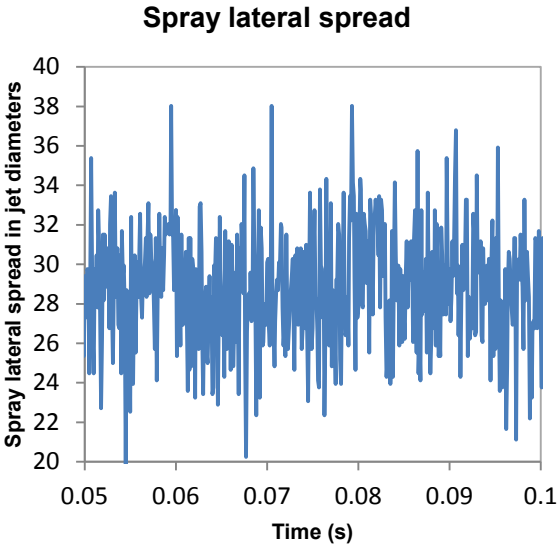

Figure 64. Time trace of lateral spread of spray: Case - P=2.04 atm We=60 q=18 f=90 Hz MDL=10%

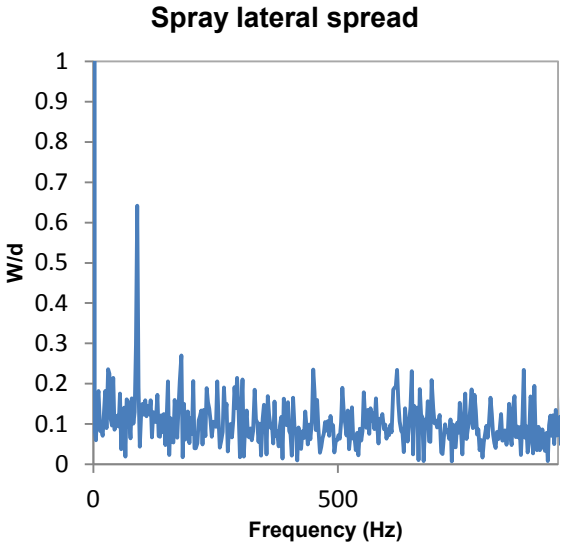

Figure 65. Frequency spectrum of lateral spread of spray: Case - P=2.04 atm We=60 q=18 f=90 Hz MDL=10%

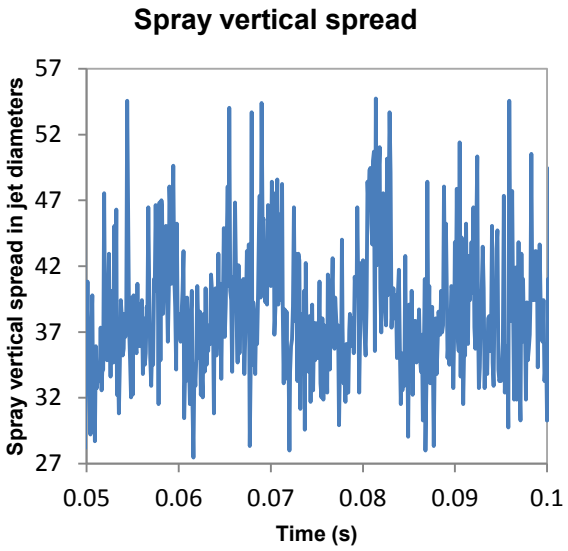

Figure 66. Time trace of vertical spread of spray: Case - P=2.04 atm We=60 q=18 f=90 Hz MDL=10%

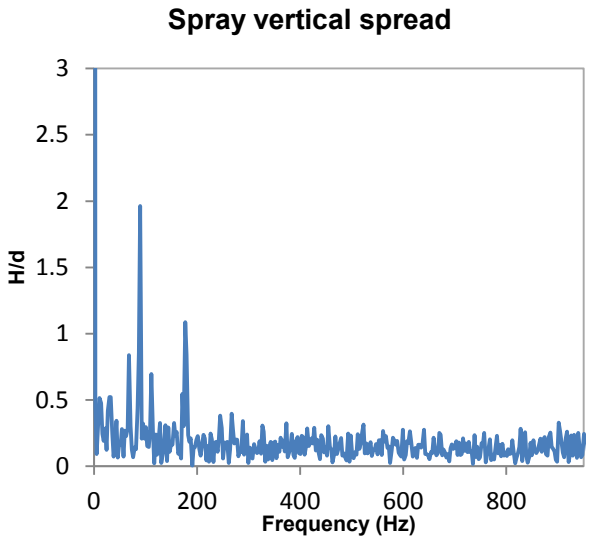

Figure 67. Frequency spectrum of vertical spread of spray: Case - P=2.04 atm We=60 q=18 f=90 Hz MDL=10%

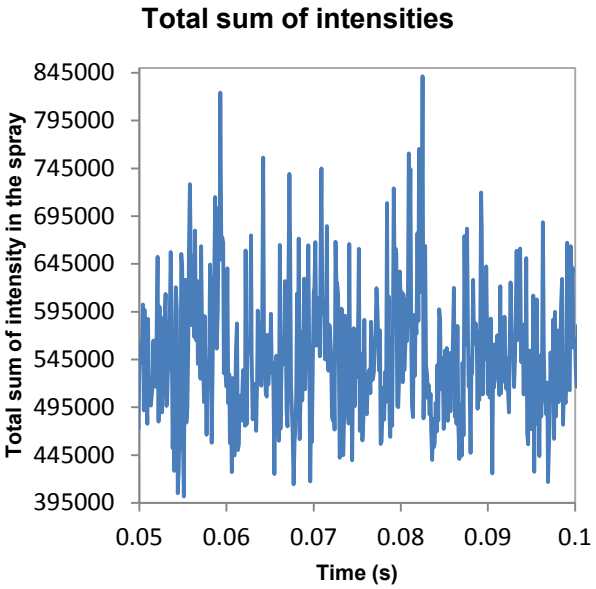

Figure 68. Time trace of total sum of spray pixel intensities: Case - P=2.04 atm We=60 q=18 f=90 Hz MDL=10%

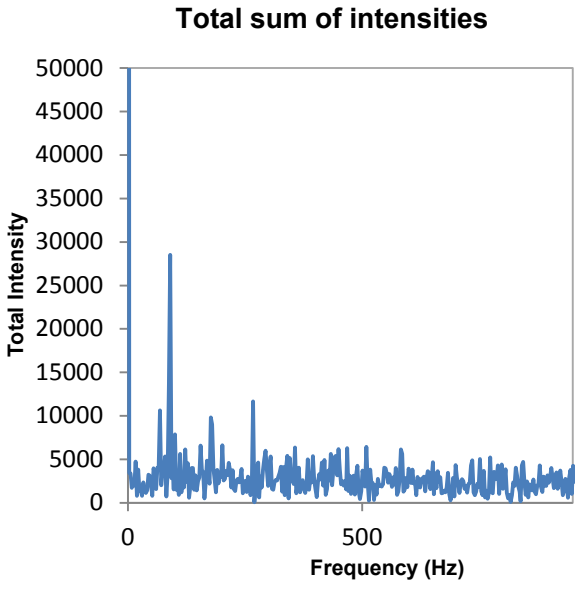

Figure 69. Frequency spectrum of total sum of spray pixel intensities: Case - P=2.04 atm We=60 q=18 f=90 Hz MDL=10%

The center of intensity is a parameter representative of the position and penetration of the liquid spray which is less subjective to errors which are associated with thresholding the image to obtain the upper penetration boundary. Similar to the procedure used in analyzing the near-field spectra, the power fractions were calculated from the center of intensity spectra at the modulating frequency and their square roots computed. These quantities are analogous to the RMS amplitude at the modulation frequency normalized by the RMS amplitude of the signal, as given in Eq. (19). For a signal *h(t)* where *t* is discrete time from 0 to *n*, *H(f)* is the amplitude in frequency domain at frequency *f*, and f_1 and f_2 are the bounds of the frequency band of interest around the modulation frequency (15 Hz band used in this study), normalized RMS amplitude can be expressed as Eq. (20). This quantity is then compared between the various test conditions to notice spray behavior.

$$Normalized\ RMS\ Amplitude = \sqrt{\frac{Power\ of\ the\ signal\ at\ the\ frequency\ of\ interest}{Power\ in\ the\ total\ signal}} \qquad (19)$$

$$Normalized\ RMS\ Amplitude = \sqrt{\frac{2\sum_{f_1}^{f_2}|H(f)|^2}{\left(\frac{\sum_{t=0}^{n}|h(t)|^2}{n+1}\right)}} \qquad (20)$$

It is observed in Figure 70 that the center of intensity, whose response can be expected to be similar to that of momentum flux ratio in the near-field, responds about 4 times (or greater) at

lower frequency of f=90 Hz compared to the higher frequency of f=450 Hz. The trend of the response weakening as frequency of modulation increases suggests that the up-and-down flapping action of the spray in the far-field is related to the penetration in the near-field.

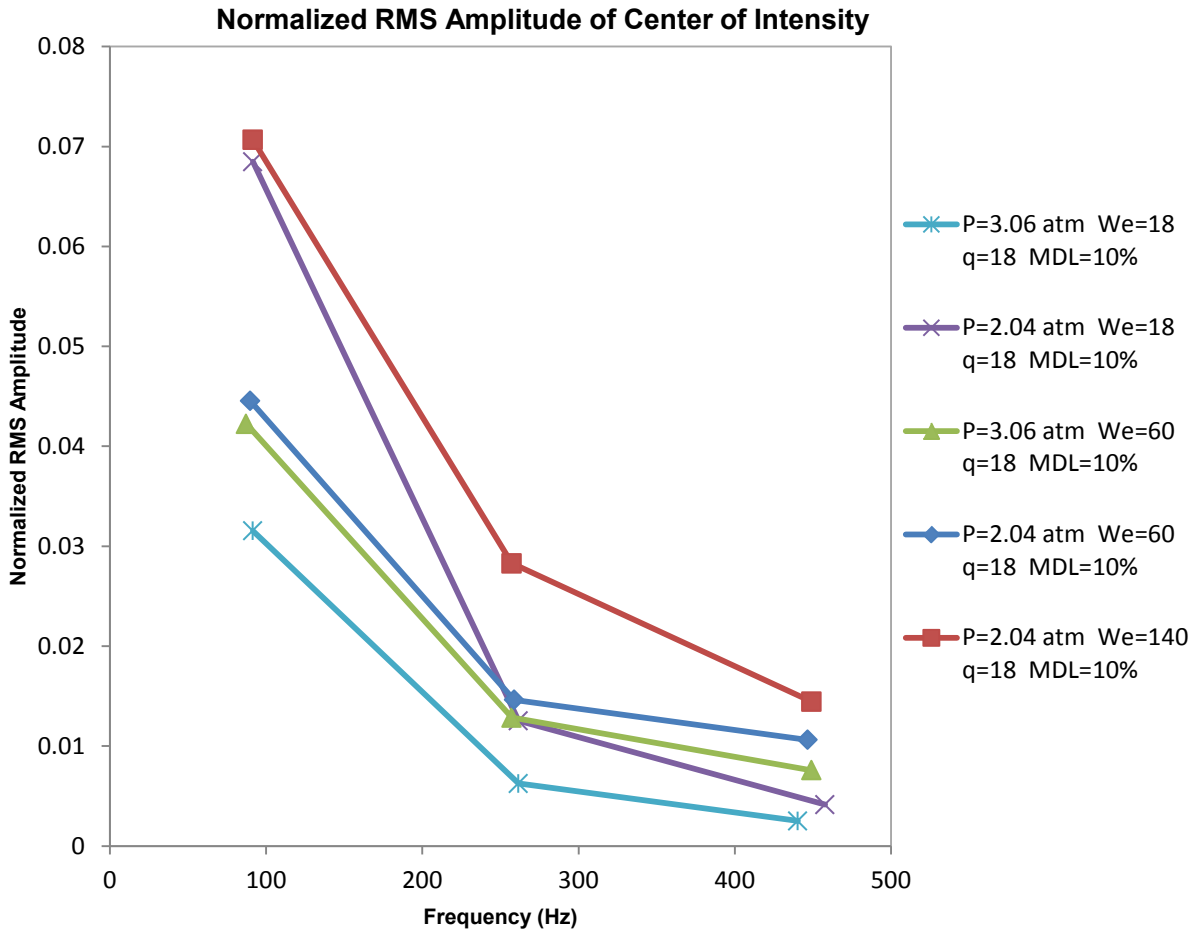

Figure 70. Response of center of intensity at different frequencies

A corresponding plot is created with the information obtained from the spectra of response of the vertical extent (spray height) of the spray and is shown in Figure 71. The trend in this plot is quite similar to the one observed from the corresponding center of intensity information. It signifies that the vertical height of the spray varies about 4 times more in the lower frequency

cases compared to higher frequencies. It suggests a possible coupling between the center of intensity's movement and the change in vertical spread of the spray, which will be explored later in this chapter.

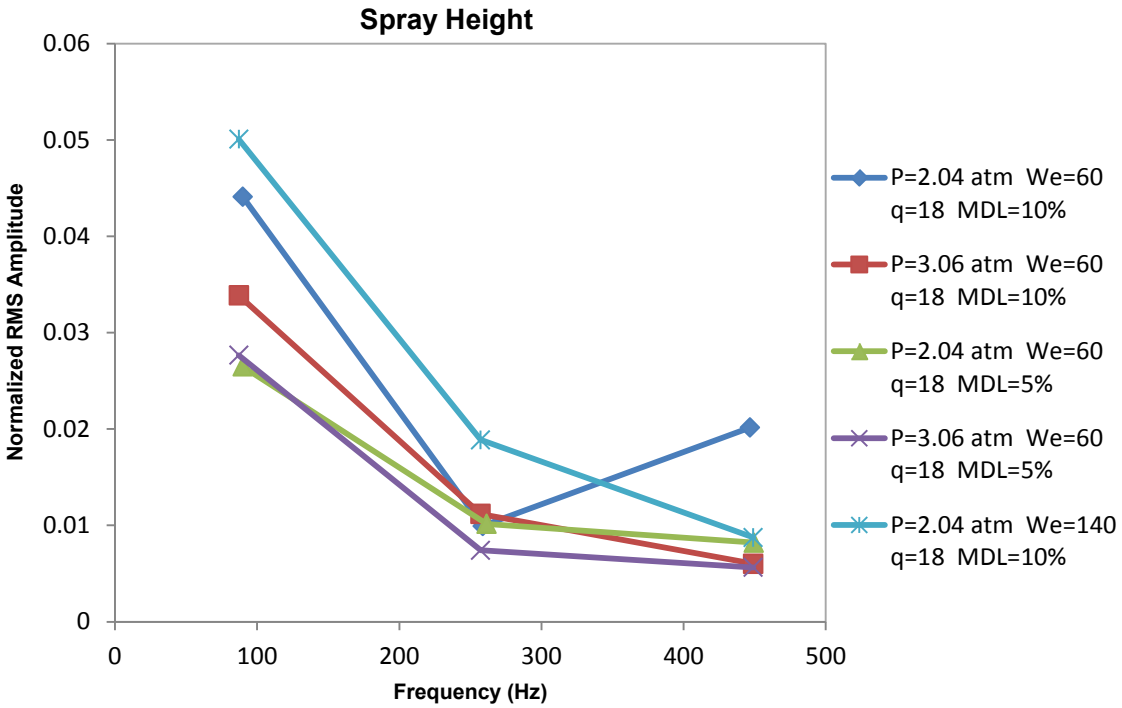

Figure 71. Response of vertical extent of the spray at different frequencies

Figure 72 shows the effect of modulation level at two different frequencies. As expected, the movement of the center of intensity increases with modulation level. The increase is moderate for the higher frequency of 450 Hz while the normalized amplitude of the response jumps to about twice its value on increasing modulation level from 5% to 10% at f=90 Hz.

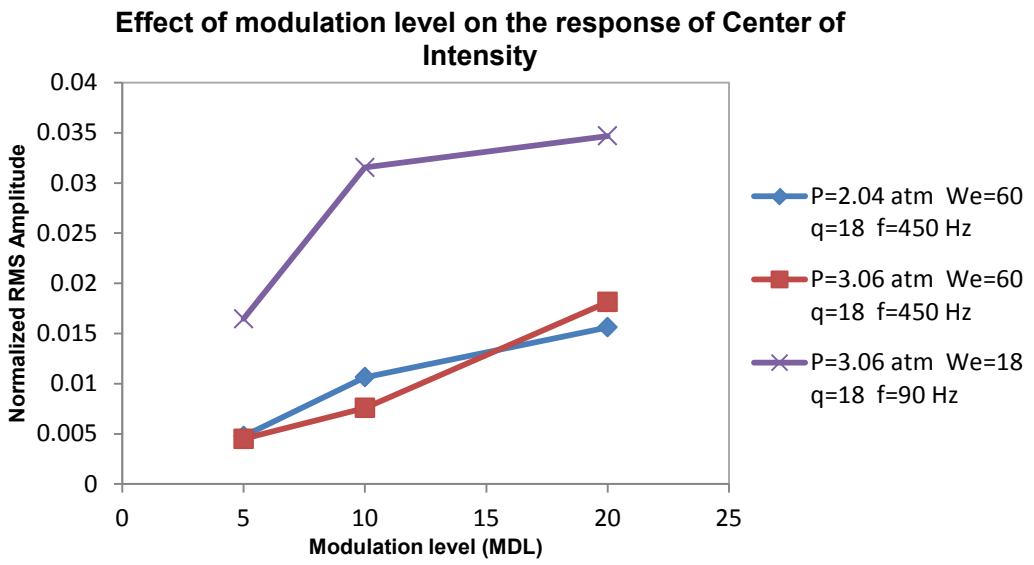

Figure 72. Effect of modulation level on the response of Center of Intensity: Case - P=2.04 atm We=60 q=18 f=90 Hz MDL=10%

From the response of the center of intensities and the vertical spray extent, it is apparent that the phase difference between the signals would offer significant insight into spray behavior. Figure 73, Figure 74 and Figure 75 show the juxtaposed signals of center of intensity with vertical extent, lateral extent and total sum of intensity respectively, after normalizing all the signals to zero mean and unit variance. It is observed that the signals, despite the noise, appear to be in phase with each other. This would indicate that as the spray flaps to its higher point, the spray expands both vertically and laterally to its maximum extent. Also, the total Mie-scattering intensity which is proportional to the surface area of the droplets in the spray, reaches its maximum value in the period. In order to see if the observation holds for all the test cases, the signals were then filtered around the peak modulation frequency and then plotted together for different flow conditions. The phase difference between them was calculated using cross-correlation.

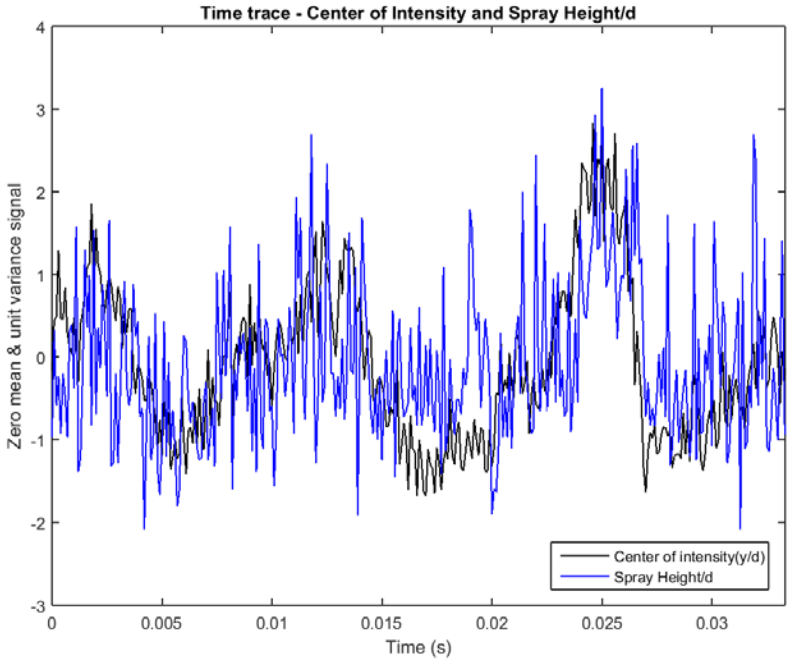

Figure 73. Center of intensity and vertical spread of spray: Case - P=2.04 atm We=60 q=18 f=90 Hz MDL=10%

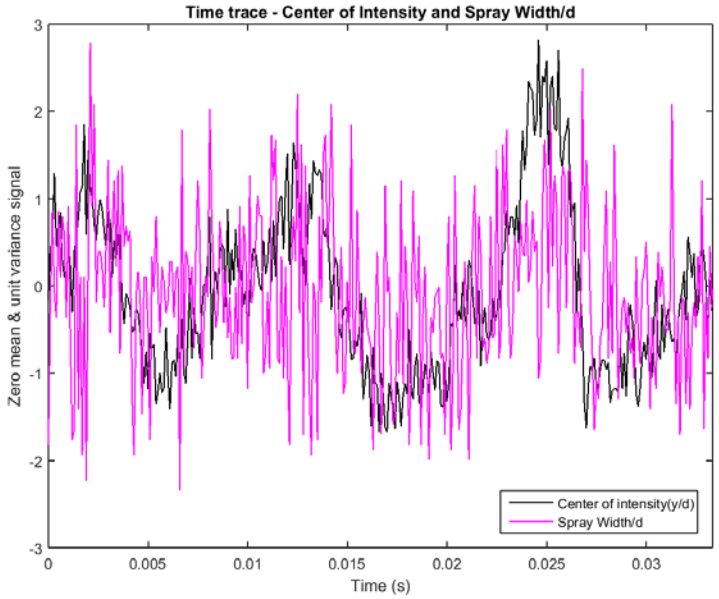

Figure 74. Center of intensity and lateral spread of spray: Case - P=2.04 atm We=60 q=18 f=90 Hz MDL=10%

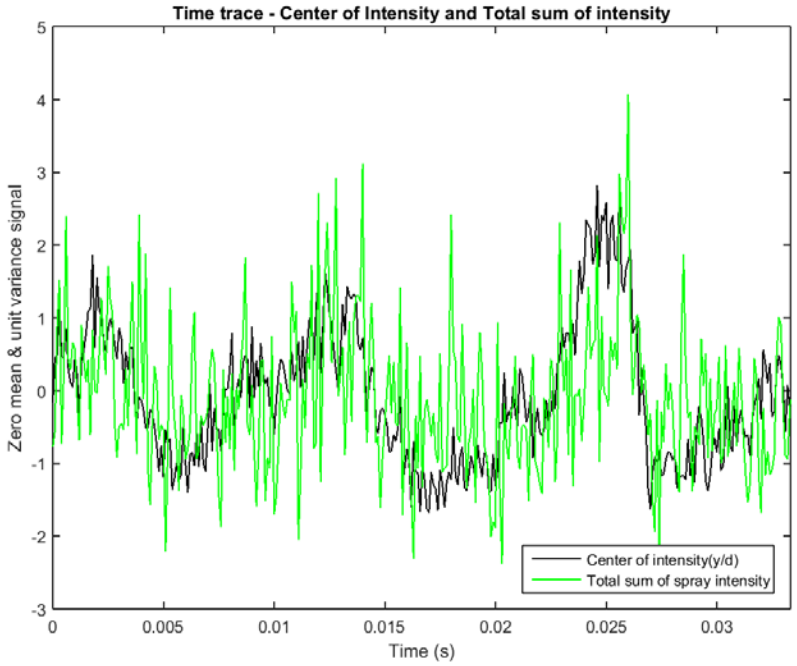

Figure 75. Center of intensity and total sum of intensity in the spray: Case - P=2.04 atm We=60 q=18 f=90 Hz MDL=10%

Figure 76 to Figure 79 show the signals filtered using a second-order Butterworth filter (with a bandwidth of 60 Hz around the fundamental frequency), in the same time interval. The Weber number=18 cases contain only center of intensity and total sum of intensity signals while the Weber number=60 cases show the lateral spread and vertical spread of the spray additionally. It can be observed that the total sum and the center of intensity are phase shifted for both the frequencies 90 Hz and 260 Hz in the *We*=18 cases shown in Figure 76 and Figure 77. However, it is interesting to note that in the lower frequency case of *f*=90 Hz in *We*=60, all the signals are in phase with each other but they are phase shifted with an increase in frequency to *f*=450 Hz (Figure 78 and Figure 79).

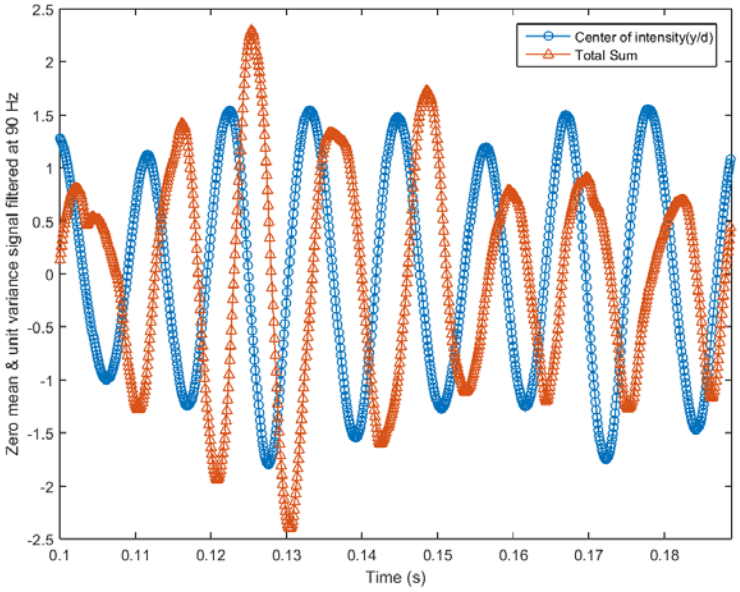

Figure 76. Center of intensity and Total sum of intensities: Case - P=3.06 atm We=18 q=18 f=90 Hz MDL=10%

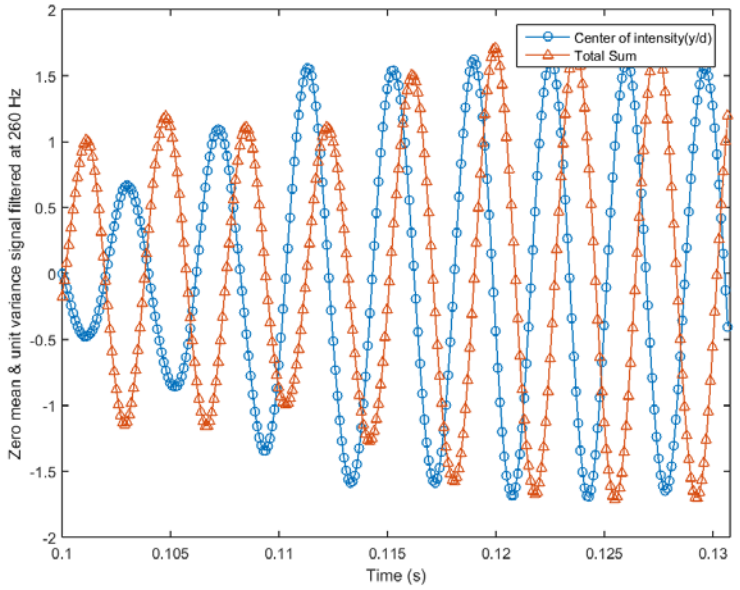

Figure 77. Center of intensity and Total sum of intensities: Case - P=3.06 atm We=18 q=18 f=260 Hz MDL=10%

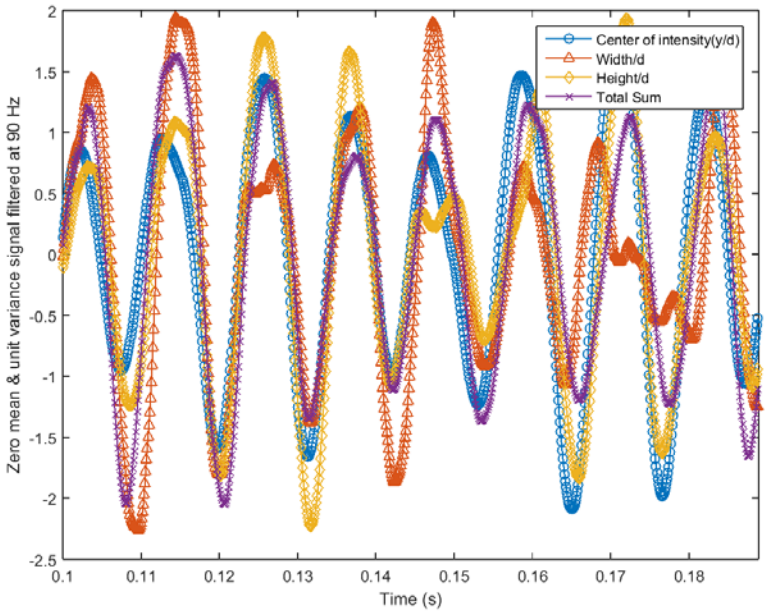

Figure 78. Center of intensity and Total sum of intensities: Case - P=2.04 atm We=60 q=18 f=90 Hz MDL=10%

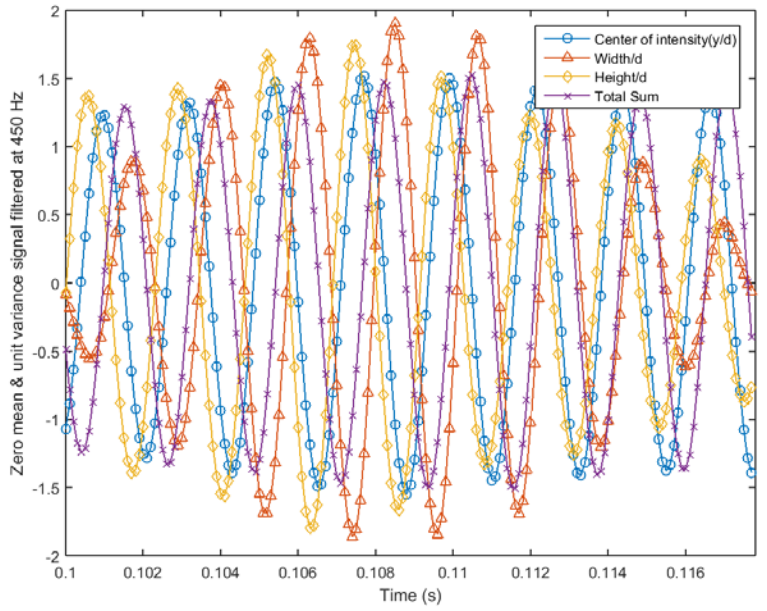

Figure 79. Center of intensity and Total sum of intensities: Case - P=2.04 atm We=60 q=18 f=450 Hz MDL=10%

The observation that the signals corresponding to movement of center of intensities and the total sum of intensities possess variable phase differences between themselves is of significance. It implies that there might be a difference in the time when the spray attains its maximum penetration point and its maximum volume flux point. To explain the phase differences in the two Weber number conditions, consider the corresponding frames where the spray is seen to attain its maximum penetration.

Consider the far-field (x/d=50) penetration in the Weber number=18 case at a modulation frequency of 90 Hz (Figure 80). It was observed from the instantaneous images that due to the lower crossflow velocity, the droplets generated after column breakup point in this breakup regime were noticeably larger compared to higher Weber number cases. The larger droplets are generated when the momentum flux ratio reaches a local maximum within one period of modulation of crossflow in the near-field. These larger droplets, owing to their greater inertia, penetrate the farthest in the crossflow and convect downstream slower compared to the smaller droplets. By the time the droplets arrive at the far-field, the near-field momentum flux ratio would have decreased and due to the higher crossflow velocity, smaller droplets are formed from the column breakup point. The smaller droplets attain the crossflow velocity much faster due to their smaller mass. Therefore by the time the larger droplets arrive at the far-field, the smaller droplets follow close behind. This is noticed in the time traces in Figure 76 where the maximum height is reached by the center of intensities and after a phase lag, the total sum of intensities reaches its maximum.

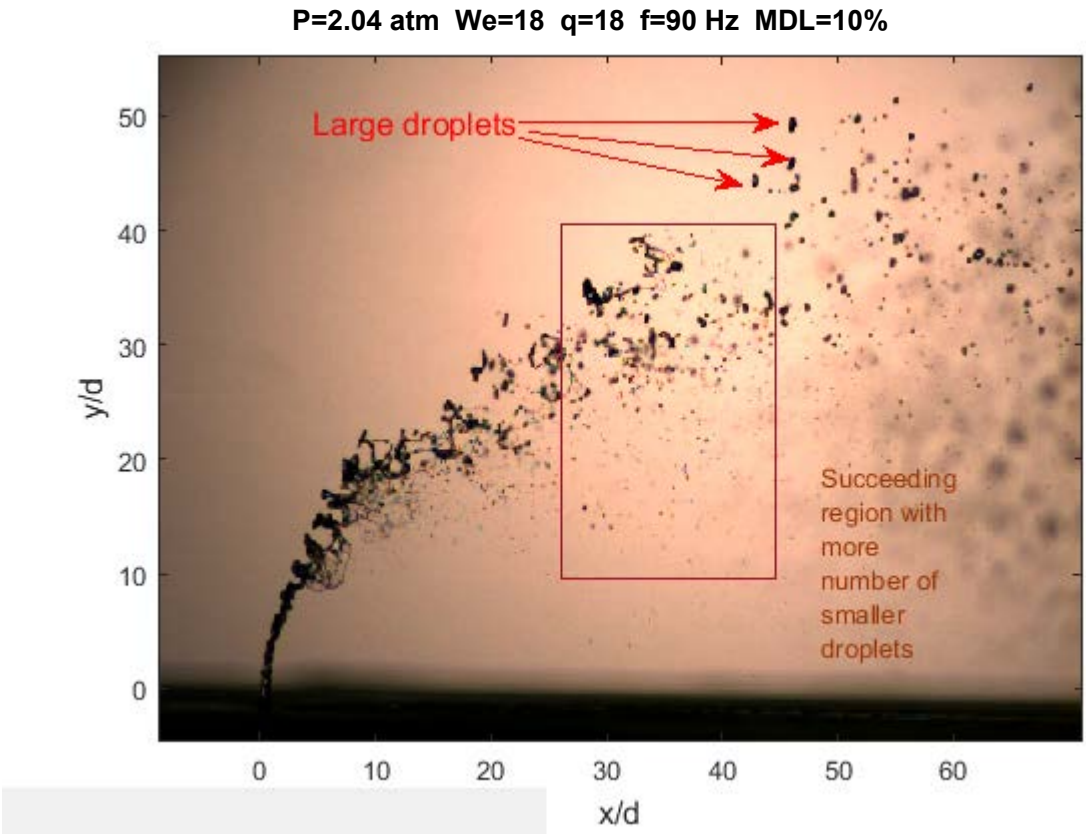

Figure 80. Frame corresponding to spray attaining maximum penetration in the far-field: Case - P=2.04 atm We=18 q=18 f=90 Hz MDL=10%

In case of higher Weber numbers (multimode and shear breakup), the behavior is explained with the case of We=60 at modulation frequency *f*=90 Hz. Figure 81 is a frame of the time when the spray attains maximum penetration in the far-field. Similar to the case of We=18, the momentum flux ratio reaches a local maximum in the modulation period in the near-field. At that point, in addition to being the moment when more mass of liquid is injected, the droplets generated by the column are larger within the period of oscillation. They begin to penetrate higher into the crossflow after column breakup. However, because of the higher mean crossflow velocity, the larger droplets undergo additional breakup and generate small droplets. At the same time, it is noticed that the column undergoes shear stripping at a short transverse distance after injection

and generates small droplets. Thus, the spray front generated has a larger vertical extent and is composed of a large number of small droplets. Owing to the relatively uniform size distribution in comparison to the lower Weber number cases, the droplets' arrival time is also close to each other. The same behavior is also noticed in the shear breakup regime at We=140. The reason for the phase-synchronized response at f=90 Hz of center of intensity, vertical extent and the total sum of intensities of the spray is therefore expected to be dependent on the droplet size and velocity.

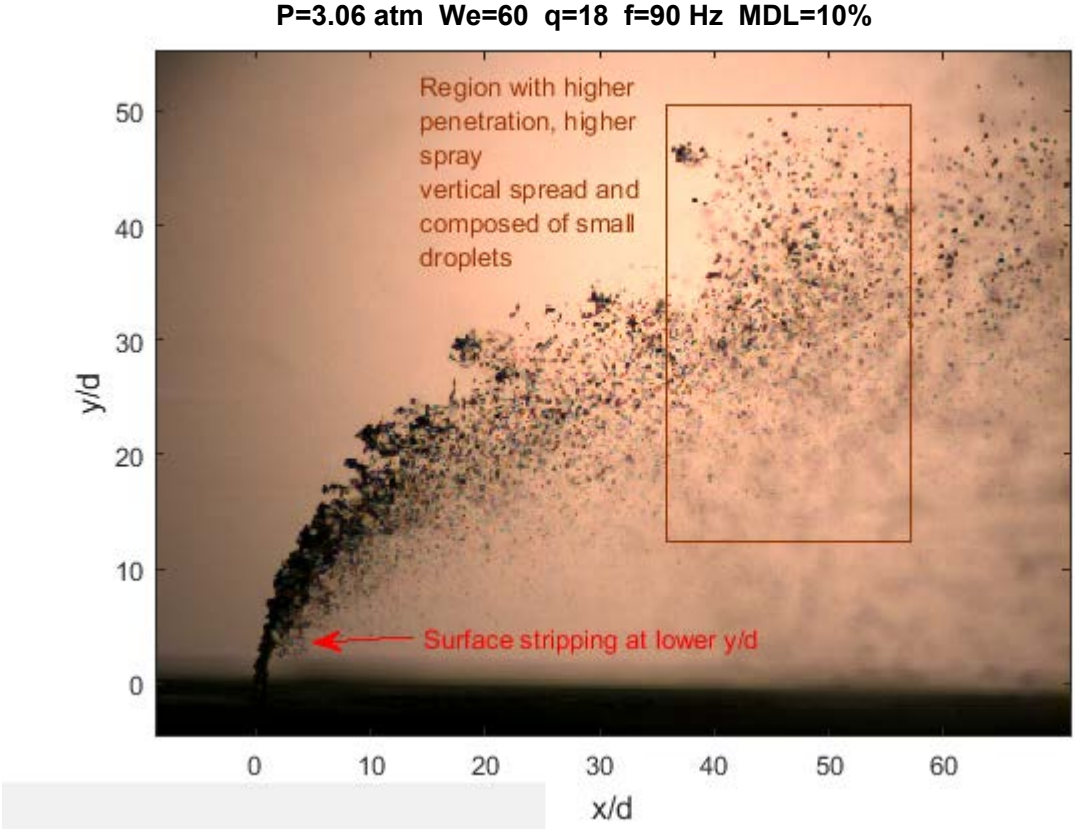

Figure 81. Frame corresponding to spray attaining maximum penetration in the far-field: Case - P=3.06 atm We=60 q=18 f=90 Hz MDL=10%

At higher modulation frequencies, the angular frequency of modulation is an additional factor that interacts with the droplet size and velocity. Since the droplets are subjected to variable

crossflow velocity, information about the instantaneous velocity in the flow-field would be necessary to characterize the phase differences between total sum of intensity fluctuation and center of intensity fluctuation at higher frequencies.

5.2 Comparison of Near-Field and Far-Field Response

It can be recalled that the near-field response was quantified by the parameter momentum flux ratio. The momentum flux ratio was related to the liquid column upper trajectory by Eq. (11), which is given by:

$$\frac{y}{d} = 1.3265 * q^{0.4131} * \left(\frac{x}{d}\right)^{0.5464} \qquad (11)$$

Since *y/d* is proportional to $q^{0.4131}$, the amplitude of upper trajectory *y/d* in the presence of crossflow modulation normalized by the mean is calculated using Eq. (21):

$$\frac{(y/d)_{Amp}}{(y/d)_{Mean}} = \left(\frac{q_{Amp}}{q_{Mean}}\right)^{0.4131} \qquad (21)$$

The movement of the center of intensity is used to analyze the movement of the spray in the far-field. Therefore, the amplitude of center of intensity (in jet diameters) normalized by the mean position of center of intensity is used here for the comparison. However, it must be noted that the center of intensity's movement need not always reflect the movement of the spray upper boundary, but it is representative of the spray position and is useful in comparing the order of the flapping behavior in the far-field.

Figure 82 (a) and (b) show a comparison of the near-field and far-field response respectively. Note that the amplitudes of fluctuations are normalized by respective mean values. After taking

this fact, and the fact that the comparison is between upper penetration in near-field and center of spray in far-field, into consideration, it can be seen that the near-field response is much stronger (~ 33% to 70%) compared to the far-field response (~ 1% to 8%).

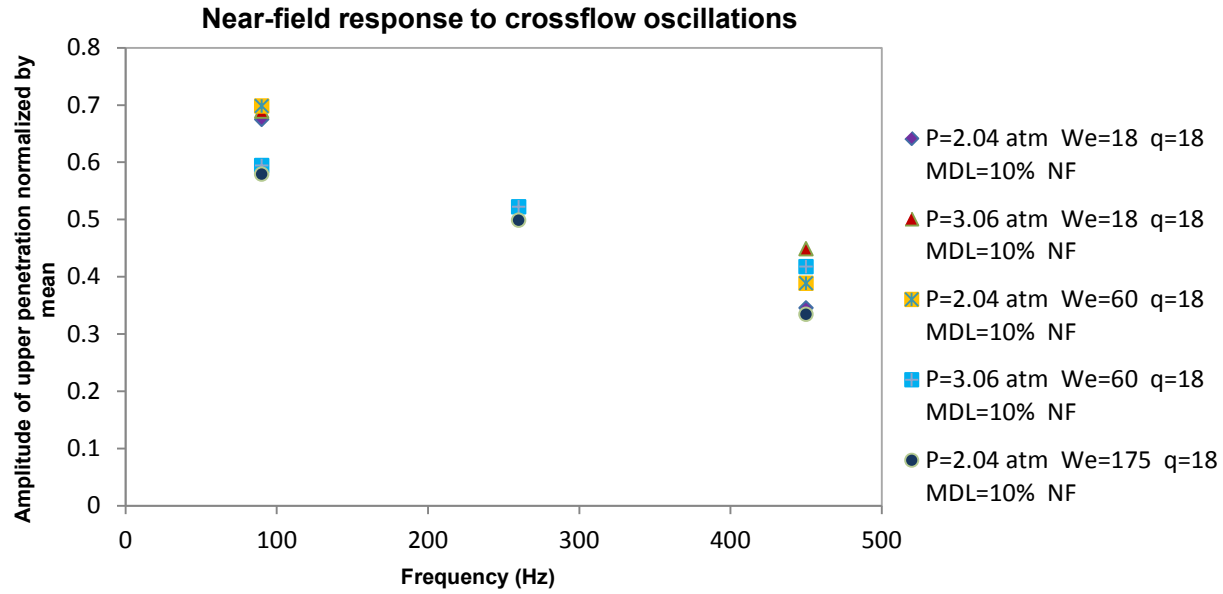

(a)

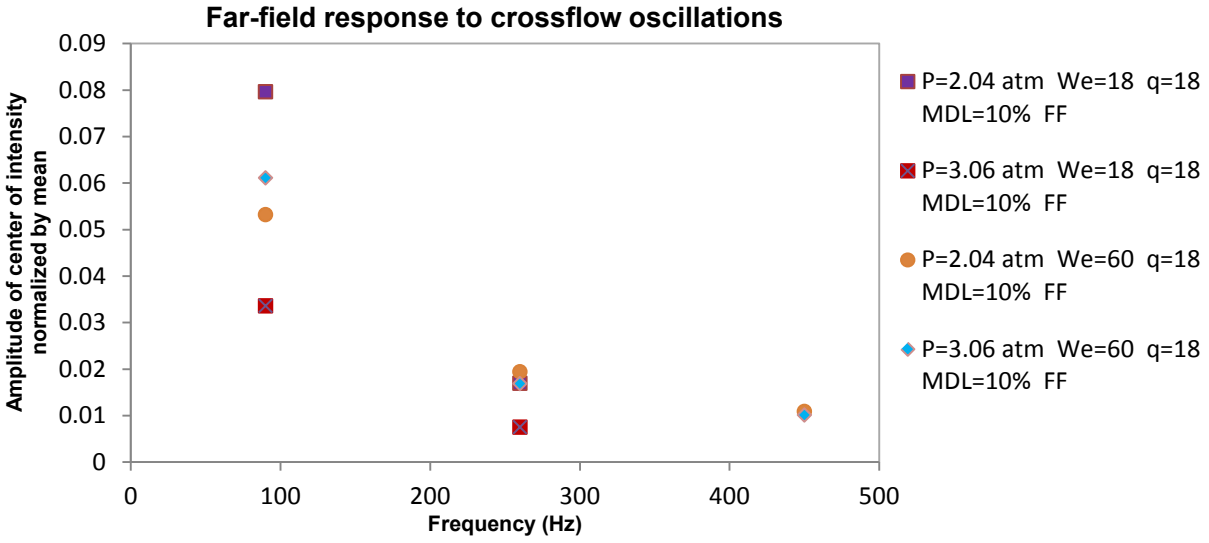

(b)

Figure 82. Comparison of near-field and far-field response

6 Conclusion and Recommendations for Future Work

6.1 Conclusion

A study on the response of a liquid jet in the presence of crossflow oscillations has been carried out to model liquid fuel placement in a combustor in the presence of combustion instabilities. Since the jet penetration in the near-field (within $x/d \approx 8$) influences the spray penetration and spatial distribution in the far-field ($x/d \approx 50$), this study investigates the spray response in both the regions. Since the liquid and gas phase properties also affect the fuel spray distribution, the Weber number is varied in the experiments from 18 to 250, to encompass the bag, multimode and shear breakup regimes, and the momentum flux ratio is varied from 10 to 30. In order to observe the effect of frequency of instability, the crossflow oscillation frequency is varied between 90 Hz and 450 Hz while the effect of variable oscillation strengths is explored by varying the modulation level between 5% and 20%. While high speed shadowgraphy provides information about the spray response in the 2-D plane aligned with both the crossflow and liquid injection directions, laser Mie-scattering intensity is used to observe the spray response in the cross-sectional plane.

The near-field penetration responds to crossflow oscillations in all flow conditions and in all modulation frequencies investigated in this study. The windward jet trajectory fluctuates in the presence of crossflow oscillation, but the strength of response is dependent on a number of flow parameters. The crossflow oscillation frequency is a major factor governing the strength of near-field response since the frequency is related to the time scale of jet exposure to the oscillation. At lower crossflow frequency (f=90 Hz), the liquid jet encounters a small phase difference between the time of injection and breakup point whereas in higher frequencies, there is a larger phase

shift due to the higher angular velocity. Evidently, the jet can attain uniform penetration with a small phase shift but will try to attain variable penetration with an increase in phase shift, which is curtailed by the cohesive forces within the jet. Consequently, the jet response is stronger in the lower frequency cases and becomes weaker as the crossflow frequency is increased. The response in the various breakup regimes is also found to be of comparable magnitude, and thus, the effect of crossflow Weber number is less apparent in this study. The momentum flux ratio and the modulation level also influence the jet response. With an increase in modulation level, the fluctuation of the liquid jet column increases. However, when normalizing the observed response by the expected response, it emerges that the effect of momentum flux ratio and the modulation level in changing the level of response is minimal, with the frequency deciding the level of response.

The far-field spray, being influenced by the near-field jet fluctuations, is also found to respond to the crossflow fluctuations both spatially and temporally. The spray executes oscillations in the transverse direction (in the direction of fuel injection, normal to the crossflow direction), as observed from both the high-speed shadowgraph images and the center of intensity's movement in the cross-sectional plane in Mie-scattering intensity images. The spray oscillatory flapping motion in the far-field, similar to the near-field response, is stronger in lower crossflow oscillation frequency cases and becomes weaker with increase in frequency. Further, there is a temporal response in the droplet size distribution and flux, as evidenced by the response in total Mie-scattering intensity of the spray in the cross-section and the droplet area calculated in the binning method. The spray height and width, both influencing the spatial distribution of droplets in the cross-sectional plane, are found to respond to the crossflow oscillations. The response of the spray height demonstrates a similar trend to the near-field penetration and far-field spray

movement, with a reduction in strength of response with increase in frequency. This suggests that not only the windward trajectory, but also the entire spray region is affected by crossflow oscillations.

The frequency of combustion instability is thus expected to be the major factor influencing the spatial and temporal distribution of the liquid fuel spray in the combustor.

6.2 Recommendations for Future Work

The present study, while addressing a number of questions on spray response to crossflow oscillations, also enlarges the scope for future work. The finding from this study that the crossflow frequency is a major factor in determining spray response suggests that a study involving a larger frequency range, and a number of intermediate frequencies, would augment the findings. The effect of Weber number is another possible avenue for research, and a study focusing on the flow-field structures and their response to crossflow oscillations in different Weber numbers will be valuable. The knowledge of velocity field of the droplets will be useful in estimating droplet arrival times. The phase difference between the pressure oscillations and near-field and far-field responses can also be explored further, as this information is crucial in estimating the coupling between crossflow oscillations and heat release oscillations.

7 References

[1] Lieuwen, T., and Zinn, B. T., "The Role of Equivalence Ratio Oscillations in Driving Combustion Instabilities in Low NO_x Gas Turbines," *Twenty-Seventh Symposium (International) on Combustion/The Combustion Institute*, 1998, pp. 1809-1816.

[2] Strutt, J. W. (Lord Raleigh), "The explanation of certain acoustical phenomena," *Nature*, Vol. 18, 1878, pp. 319-321.

[3] Wu, P.-K., Kirkendall, K.A., Fuller, R.P., and Nejad, A.S., "Breakup Processes of Liquid Jets in Subsonic Crossflows," *Journal of Propulsion and Powe*r, Vol. 13, No. 1, 1997, pp. 64-73.

[4] Becker, J., and Hassa, C., "Breakup and Atomization of a Kerosene Jet in Crossflow at Elevated Pressure," *Atomization and Sprays*, Vol. 11, 2002, p. 49-67.

[5] Tambe, S.B., Jeng, S.-M., Mongia, H., and Hsiao, G., "Liquid Jets in Subsonic Crossflow," *43rd AIAA Aerospace Sciences Meeting and Exhibit*, 10-13 January 2005, Reno, Nevada.

[6] Sallam, K.A., Aalburg, C., and Faeth, G.M., "Breakup of Round Nonturbulent Liquid Jets in Gaseous Crossflow," *AIAA Journal*, Vol. 42, No. 12, December 2004, pp. 2529-2540.

[7] Leong, M.Y., McDonell, V.G., and Samuelsen, G.S., "Effect of Ambient Pressure on an Airblast Spray Injected into a Crossflow", *Journal of Propulsion and Power*, Vol. 17, No. 5, September-October 2001, pp. 1076-1084.

[8] Elshamy, O.M., Tambe, S., Cai, J., and Jeng, S.-M., "Structure of Liquid Jets in Subsonic Crossflow at Elevated Ambient Pressures," *44th AIAA Aerospace Sciences Meeting and Exhibit*, 9-12 January 2006, Reno, Nevada.

[9] Freitag, S., and Hassa, C., "Spray Characteristics of a Kerosene Jet in Crossflow of Air at Elevated Pressure," *ICLASS 2008*, Como Lake, Italy, Sep. 8-10.

[10] Amighi, A., Eslamian, M., and Ashgriz, N., "Trajectory of Liquid Jets in High Pressure and High Temperature Crossflows," *ICLASS 2009, 11th International Annual Conference on Liquid Atomization and Spray Systems*, Vail, Colorado USA, July 2009.

[11] Ragucci, R., Bellofiore, A., and Cavaliere, A., "Trajectory and Momentum Coherence Breakdown of a Liquid Jet in High-Density Air Cross-Flow," *Atomization and Sprays*, Vol. 17, 2007, pp. 47-70.

[12] Lubarsky, E., Shcherbik, D., Bibik, O., Gopala, Y., and Zinn, B.T., "Fuel Jet in Crossflow- Experimental Study of Spray Characteristics," *Advanced Fluid Dynamics,* Prof. Hyoung Woo Oh (Ed.), ISBN: 978-953-51-0270-0, InTech, Available from: http://www.intechopen.com/books/advanced-fluid-dynamics/fuel-jet-in-crossflow-experimental-study-of-spray-characteristics, 2012.

[13] Wu, P.-K., Kirkendall, K.A., Fuller, R.P., and Nejad, A.S., "Spray Structures of Liquid Jets Atomized in Subsonic Crossflows," *Journal of Propulsion and Power*, Vol. 14, No. 2, March-April 1998, pp. 173-182.

[14] Stenzler, J.N., Lee, J.G., Santavicca, D.A., and Lee, W., "Penetration of Liquid Jets in a Cross-Flow," *Atomization and Sprays*, Vol. 16, 2006, pp. 887-906.

[15] Bellofiore, A., Cavaliere, A., and Ragucci, R., "Air Density Effect on the Atomization of Liquid Jets in Crossflow," *Combustion Science and Technology*, 179: 1-2, 319-342.

[16] Bunce, K., Lee, J. G., and Santavicca, D. A., "Characterization of Liquid Jets-In-Crossflow Under High Temperature, High Velocity Non-oscillating and Oscillating Flow Conditions," *44th AIAA Aerospace Sciences Meeting and Exhibit*, Reno, Nevada, 9-12 January 2006.

[17] McQuay, M. Q., and Dubey, R. K., "The Interaction of Well-Characterized Longitudinal Acoustic Waves with a Nonreacting Spray," *Atomization and Sprays*, Vol. 8, 1998, pp. 419-437.

[18] Anderson, T. J., Kendrick, D. W., and Cohen, J. M., "Measurement of Spray/Acoustic Coupling in Gas Turbine Fuel Injectors," *36th AIAA Aerospace Sciences Meeting and Exhibit,* AIAA 98-0718, 1998.

[19] Song, J., Ramasubramanian, C., and Lee, J. G., "Response of Liquid Jet to Modulated Crossflow," Atomization and Sprays, Vol. 24, 2014, pp. 129-154.

[20] Song, J., and Lee, J. G., "Characterization of Spray formed by Liquid Jet Injected into Oscillation Air Crossflow," *Proceedings of ASME Turbo Expo 2015*, GT2015-43726, 2015.

[21] Anderson, T. J., Proscia, W., and Cohen, J. M., "Modulation of a Liquid-Fuel in an Unsteady Cross-Flow," *Proceedings of ASME Turbo Expo '01*, 2001-GT-0048, 2001.

[22] Waser, M. P., and Crocker, M. J., "Introduction to the Two-Microphone Cross-Spectral Method of Determining Sound Intensity," *Noise Control Engineering Journal*, Vol. 22 ,No. 3, May-June 1984, pp. 76-85.

[23] Lee, H. J., "Combustion Instability Mechanisms in a Lean Premixed Gas Turbine Combustor," Ph. D. Dissertation, Mechanical Engineering, The Pennsylvania State University, August 2009.

[24] Berens, P., "CircStat: A MATLAB Toolbox for Circular Statistics," *Journal of Statistical Software*, Vol. 31, No. 10, September 2009.

[25] Moffat, R. J., "Describing the uncertainties in experimental results," *Experimental Thermal and Fluid Science*, Vol. 1, No. 1, January 1988, pp. 3-17.

[26] Peters, R. D., "Tutorial on Power Spectral Density Calculations for Mechanical Oscillators (with an exhaustive discussion of Units)," Physics Department, Mercer University, Macon, Georgia, January 2012. [http://physics.mercer.edu/hpage/psd-tutorial/psd.html. Accessed 7/06/2015.]

Appendix A: Error Analysis

The sources of errors in this study can be broadly classified into two categories: 1. Experimental, and 2. Post-processing. Calibration of various systems has been performed in order to quantify and reduce the experimental errors. The processing error is inherently more complex to quantify, and therefore, the analysis procedures are rigorously scrutinized to identify possible errors. This section presents a brief discussion of the possible errors in the current experimental study.

Experimental errors

An error analysis is performed to estimate the errors in the primary flow parameters [25]. For example, the error in a quantity X, if X can be expressed in product form by $X=A^aB^bC^c$, can be given in a simple form as Eq. (22).

$$\frac{\Delta X}{X}=\sqrt{\left(a\frac{\Delta A}{A}\right)^2+\left(b\frac{\Delta B}{B}\right)^2+\left(c\frac{\Delta C}{C}\right)^2} \qquad (22)$$

To estimate the error in the air density, for instance, the error in crossflow static pressure and temperature will need to be identified. Noting the error in pressure from the expressed accuracy of the digital gauge to be ΔP=0.05 atm, and assuming a generous estimate of the error in temperature to be 5 K , since the room temperature is maintained around 293 K, the error estimate for crossflow air density at a pressure of 3.06 atm is given by Eqs. (23) and (24).

$$\frac{\Delta \rho}{\rho}=\sqrt{\left(1*\frac{\Delta P}{P}\right)^2+\left(-1*\frac{\Delta R}{R}\right)^2+\left(-1*\frac{\Delta T}{T}\right)^2} \qquad (23)$$

$$\frac{\Delta\rho}{\rho} = \sqrt{\left(1*\frac{0.05}{3.06}\right)^2 + \left(-1*\frac{0}{287}\right)^2 + \left(-1*\frac{5}{293}\right)^2} \qquad (24)$$

Therefore, the percentage error in air density is $\Delta\rho/\rho$=2.4 %.

Similarly, the error in various parameters are computed for a typical case of P=3.06 atm, We=60 and q=18, making maximum error estimates wherever possible, and are presented in Table 5.

Table 5. Error estimates

Flow Parameter	**Estimated error (in %)**
Crossflow air temperature, T	1.7
Crossflow air pressure, P_a	1.7
Crossflow air mass flow rate, $\dot{m}_a$	0.5
Crossflow air density, ρ_a	2.4
Orifice diameter, d	1.0
Orifice exit area, A	2.0
Liquid mass flow rate, $\dot{m}_j$	3.9
Liquid density, ρ_j	0.3
Liquid injection velocity, v_j	4.4
Crossflow air velocity, v_a	2.4
Momentum flux ratio, q	10.4
Crossflow Weber number, We	5.5

Since the estimates presented in Table 5 utilize liberal error estimates in the calculations, the actual experimental errors are expected to be within the bounds of the estimated errors. The errors in some of the measured quantities such as the orifice diameter, the liquid fuel mass flow rate, modulation level, etc. are quantified and minimized with the help of calibrations, as described in Section 2.3.

Post-processing errors

The identification of errors arising from the manipulation of acquired raw data is challenging because of the number of intermediate processes and their obscurity in propagating errors. Therefore, every attempt has been made to keep the processing to a minimum while extracting useful data.

In extracting the windward trajectory points from instantaneous images, a 10% threshold was used. Since the contrast between the background and the jet is very high in instantaneous images, the high intensity gradient assures that the ambiguity is less than 2 pixels approximately in locating the boundary points. In many of the test cases, surface waves on the windward surface offer possible distortion in finding the least-square curve fit. In order to reduce the error, only the points within x/d=2 were utilized, where the amplitudes of surface waves are small.

In the far-field analysis, the errors in the binning method are expected to be insignificant in the data analysis since the actual sum in the bins is only used as an indicator of spray location. Furthermore, the threshold set to locate the droplets is uniform across all the bins, all the images and all the conditions, offering consistency in the analysis.

In the Mie-scattering intensity images, the center of intensity is chosen to study the spray movement since it is less sensitive to noise and the process of thresholding is avoided. While

quantifying the spray movement in the far-field, therefore, the center of intensity offers less subjective and more reliable information.

Appendix B: Extraction of Windward Trajectory Points from Averaged Images

The liquid jet trajectory correlations are sensitive to the spray visualization method as well as to the post-processing technique. For example, many researchers utilize thresholding technique to extract upper trajectory points from shadowgraphs. However, various threshold levels yield different trajectories and the method is thus prone to errors when the difference in intensity between the shadow and the background is small.

For example, consider the following illustration in Figure 83 where a 10% threshold is applied. While the boundary from thresholding matches the spray boundary close to the injector, the error in detection becomes progressively larger with downstream distance from the nozzle.

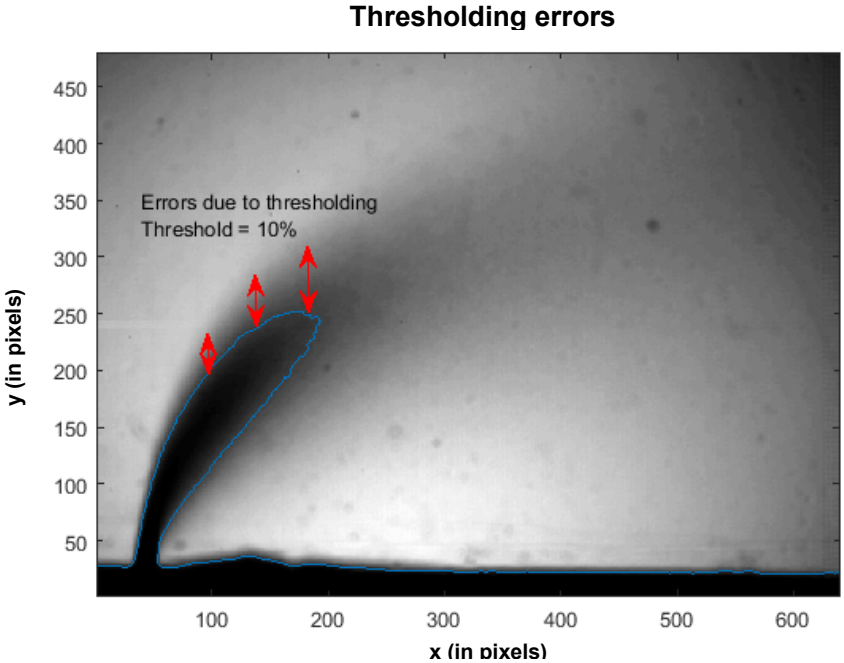

Figure 83. Thresholding errors

Therefore, a new method was conceptualized to extract the boundary points from the averaged images where the hazy portions of the spray are susceptible to be missed by thresholding process. The algorithm for this method can roughly be specified in the following steps:

- The raw RGB averaged image is converted to grayscale image.
- The columns of the grayscale image are converted to column vectors corresponding to their intensities.
- For each column vector of intensities, a smoothing is performed using a 21-point moving average filter in order to make the algorithm insensitive to small peaks in the signal.
- Identifying the unique signal shape, a selection criterion is set which calculates the absolute value of product of slope and height for each point from the point of minimum intensity in the center of the spray. The point in the vicinity of the spray with a maximum of this criterion is selected as the upper boundary point as shown in Figure 84.

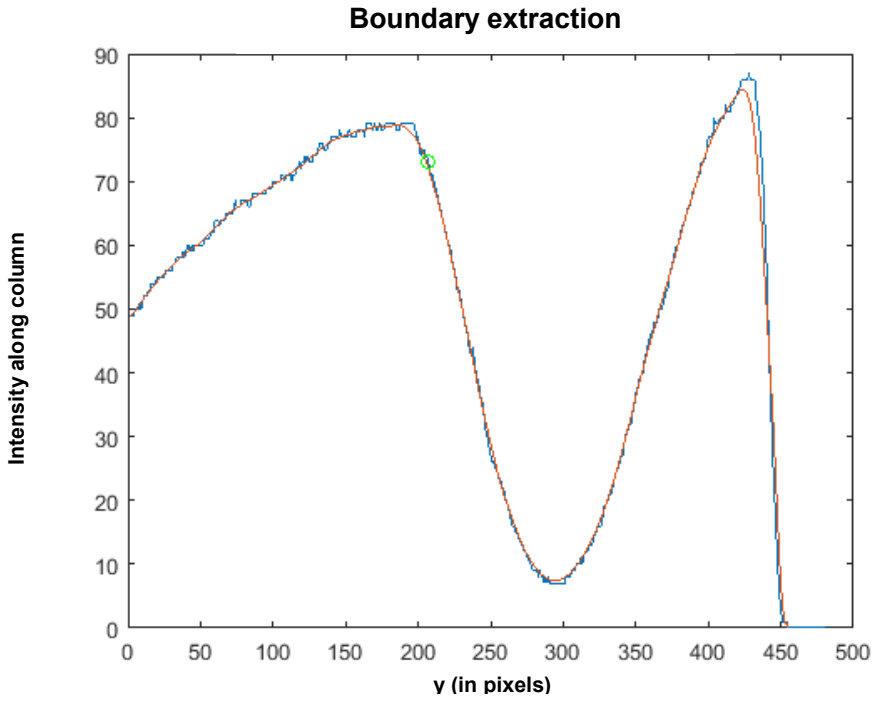

Figure 84. Location of upper boundary point

- An error is also calculated for each condition by using a polynomial estimate of the current point based on the previous points. When the error crosses a certain threshold, the algorithm stops extracting points. This stop condition is incorporated and monitored so that the detection stops when the hazy spray region leads to uncertain boundary points.

An example of a boundary extracted using this method is shown in Figure 85.

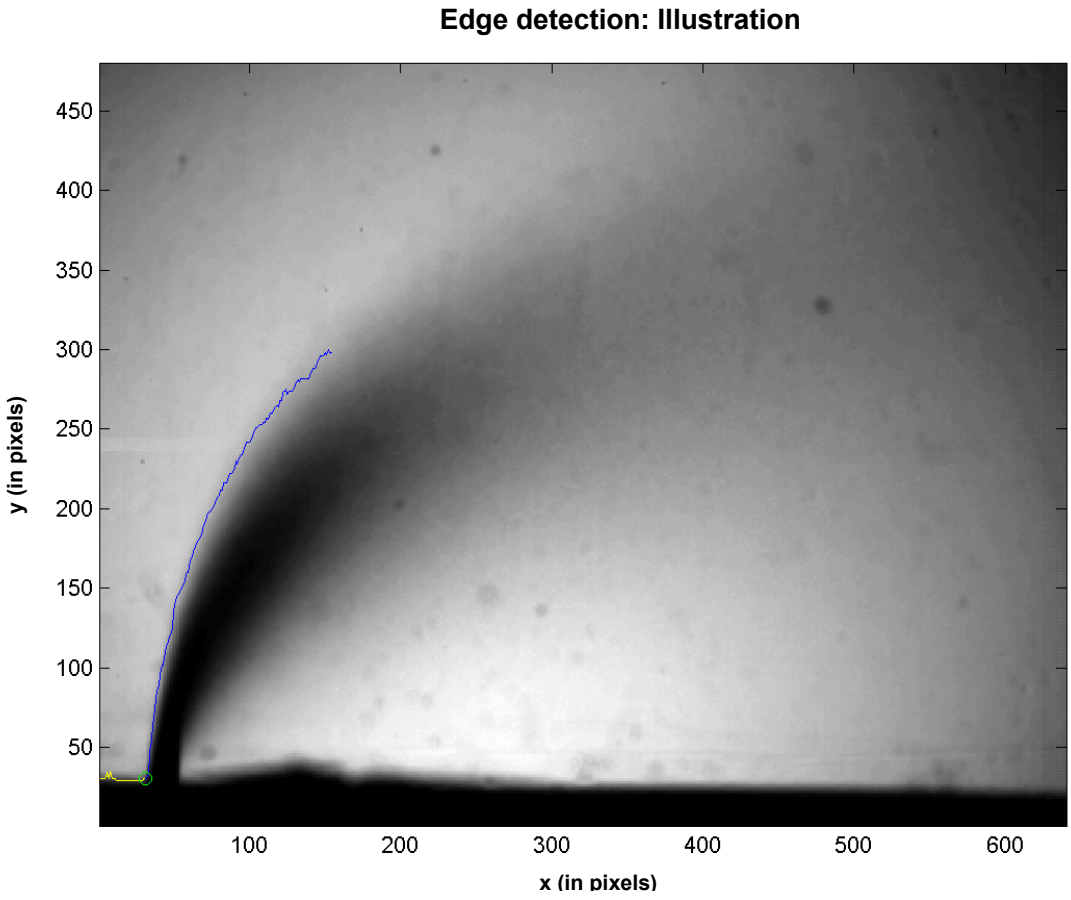

Figure 85. Spray with upper trajectory points

Appendix C: Using Power Spectrum to Analyze Frequency Spectra

The resolution of FFT spectrum depends upon the sampling frequency (F_S) and the number of samples, L, by the relation $\Delta f=F_S/L$. Therefore the frequency resolution is different for the observed q from the images and the expected q from the velocity signal because they are sampled at different frequencies and for different numbers of samples. Moreover if the frequency of interest does not lay exactly on one of the frequency bins, reading the amplitude from FFT becomes error-prone. In order to overcome these shortcomings, the power spectrum is used in place of the amplitude spectrum.

Parseval's theorem specifies that the power related to a time-series data is the same as the power contained in its transform. Therefore, even if different frequency resolutions are used for the same data series (for example, by padding zeros), the total power of the two spectra should be the same. This effect is illustrated in Figure 86 where the same time series data is transformed into two spectra with different frequency resolutions by padding zeros in the second case. Clearly, the gain in frequency resolution is offset by the fact that the amplitude suffers some leakage. However, the power contained in the spectra is the same [26].

Also in the case of comparing spectra of response and input signals, since the two spectra are of comparable power, the power values in a narrow band around the frequency of interest can be used in place of amplitude, thus minimizing errors.

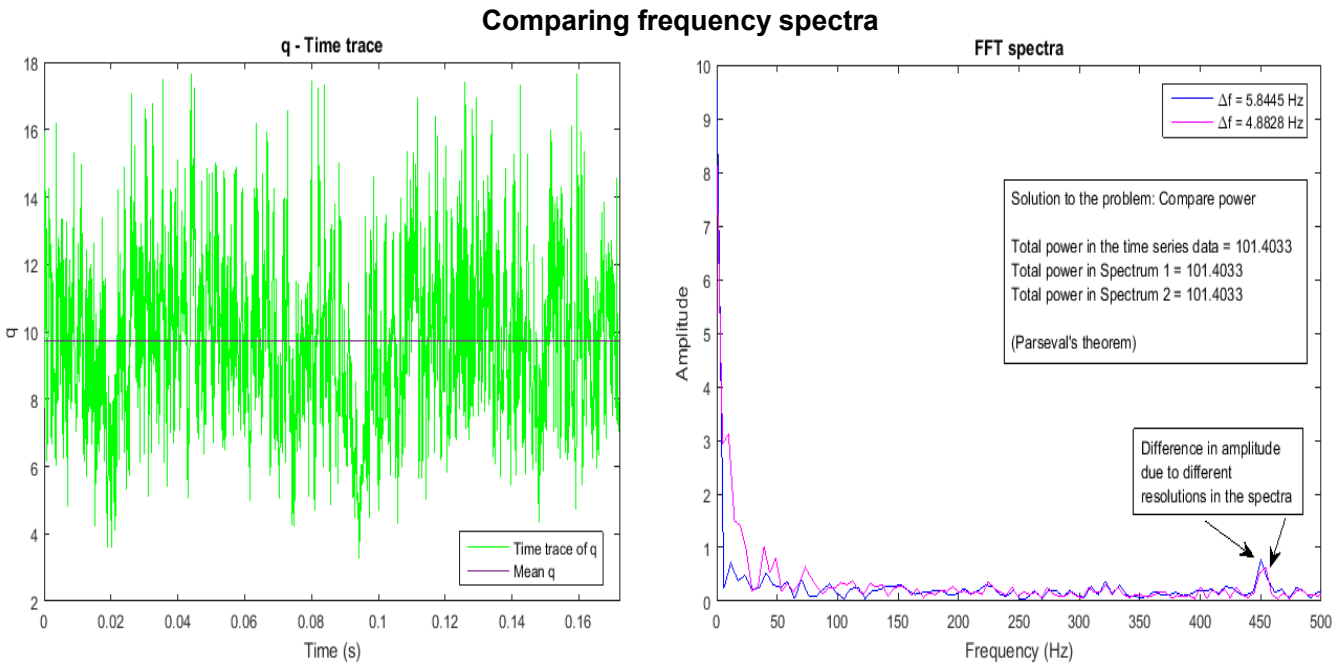

Figure 86. Comparing spectra with different resolutions

Appendix D: Filtering noise in Cross-Sectional Mie-Scattering Images

The cross-sectional Mie-scattering images are obtained using an intensifier and the instantaneous images contain background noise as shown in Figure 87.

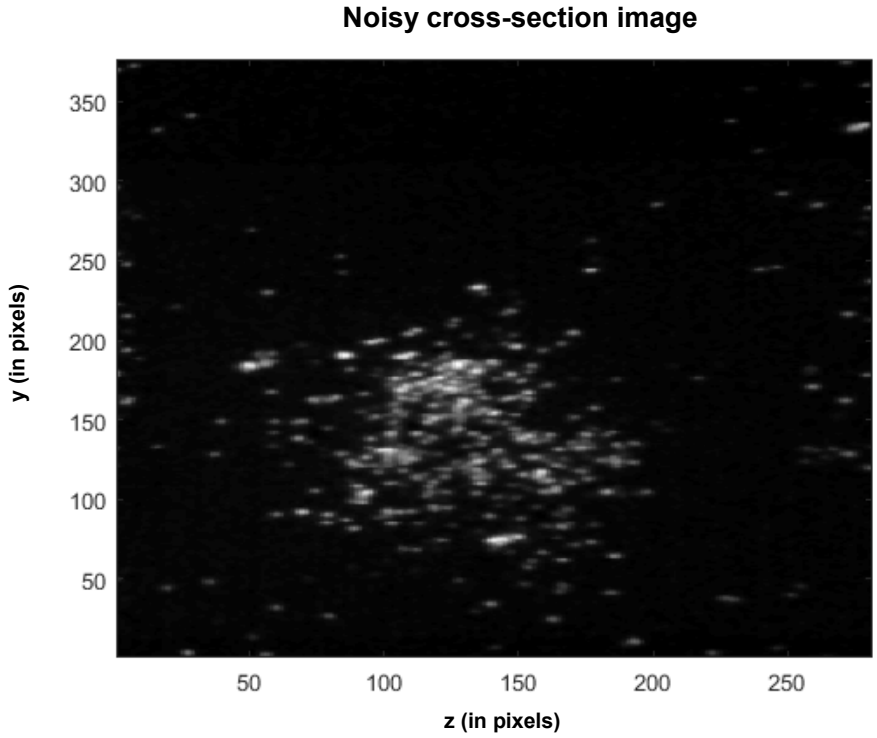

Figure 87. Mie-Scattering image with noise

Therefore in order to find the lateral and vertical extent of the spray, a procedure is used to filter out the noise, which will be explained by describing the process to locate spray lateral extent (width) using this method:

- The intensities of pixels in each column are summed up. The Maximum and Minimum values are located. Peak height is defined as difference of Maximum and Minimum.

- The column sum values, which are less than 10% of the peak height from the minimum value, are isolated.
- The mean and standard deviation of the isolated values are calculated. The base level is defined as the sum of mean and one standard deviation.
- The column sum having a minimum peak within the base level, and which is closest to the Maximum column point, is then selected as the edge.

This process is illustrated in Figure 88 with the green and magenta circles locating the spray extent. Figure 89 shows the original image with the lateral limit locations shown in green and magenta lines.

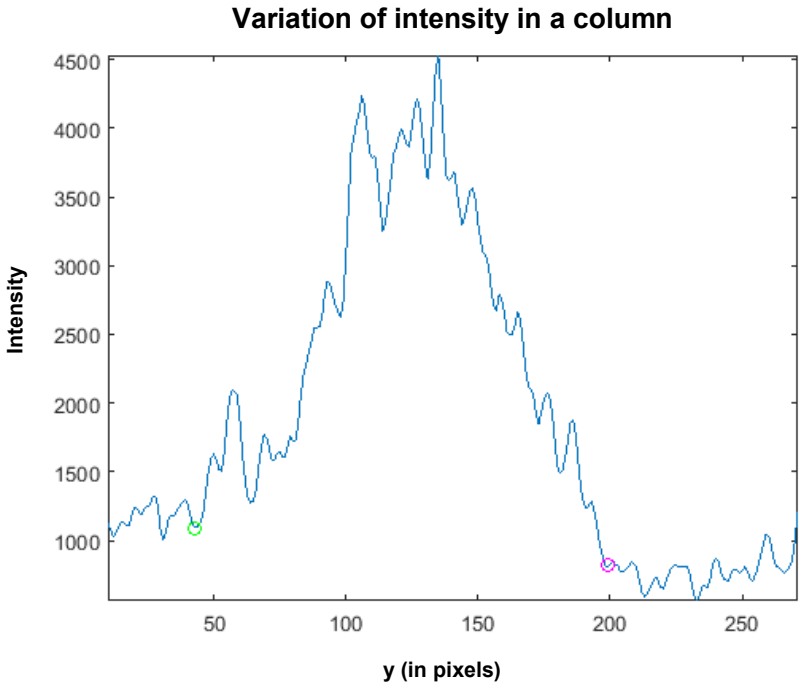

Figure 88. Location of lateral extent from "Column Sum" plot

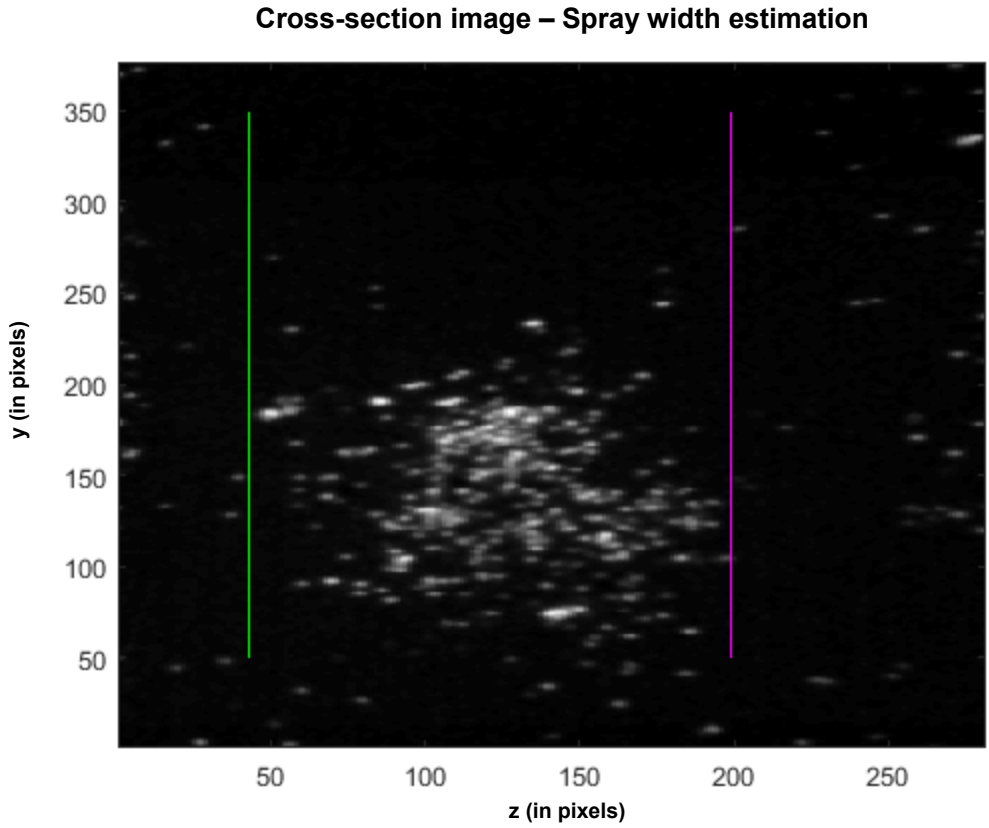

Figure 89. Cross-section image with spray lateral extent